**COMPARISON OF COMPUTATIONAL
ELECTROMAGNETIC CODES FOR
PREDICTION OF LOW-FREQUENCY
RADAR CROSS SECTION**

THESIS

Paul C. Lash, Captain, USAF

AFIT/GE/ENG/06-32

**DEPARTMENT OF THE AIR FORCE
AIR UNIVERSITY**

AIR FORCE INSTITUTE OF TECHNOLOGY

Wright-Patterson Air Force Base, Ohio

Report Documentation Page		*Form Approved* *OMB No. 0704-0188*
Public reporting burden for the collection of information is estimated to average 1 hour per response, including the time for reviewing instructions, searching existing data sources, gathering and maintaining the data needed, and completing and reviewing the collection of information. Send comments regarding this burden estimate or any other aspect of this collection of information, including suggestions for reducing this burden, to Washington Headquarters Services, Directorate for Information Operations and Reports, 1215 Jefferson Davis Highway, Suite 1204, Arlington VA 22202-4302. Respondents should be aware that notwithstanding any other provision of law, no person shall be subject to a penalty for failing to comply with a collection of information if it does not display a currently valid OMB control number.		

1. REPORT DATE **23 MAR 2006**	2. REPORT TYPE	3. DATES COVERED

4. TITLE AND SUBTITLE **Comparison Of Computational Electromagnetic Codes For Prediction of Low-Frequency Radar Cross Section**	5a. CONTRACT NUMBER
	5b. GRANT NUMBER
	5c. PROGRAM ELEMENT NUMBER
6. AUTHOR(S) **Paul Lash**	5d. PROJECT NUMBER
	5e. TASK NUMBER
	5f. WORK UNIT NUMBER
7. PERFORMING ORGANIZATION NAME(S) AND ADDRESS(ES) **Air Force Institute of Technology,Graduate School of Engineering and Management,2950 Hobson Way,Wright Patterson AFB,OH,45433-7765**	8. PERFORMING ORGANIZATION REPORT NUMBER **AFIT/GE/ENG/06-32**
9. SPONSORING/MONITORING AGENCY NAME(S) AND ADDRESS(ES)	10. SPONSOR/MONITOR'S ACRONYM(S)
	11. SPONSOR/MONITOR'S REPORT NUMBER(S)

12. DISTRIBUTION/AVAILABILITY STATEMENT   **Approved for public release; distribution unlimited.**

13. SUPPLEMENTARY NOTES   **The original document contains color images.**

14. ABSTRACT

Radar cross section (RCS) prediction of full-scale aircraft is of interest to military planners for a variety of applications. Several computational electromagnetic codes for RCS prediction are available with differing features and capabilities. The goal of this research is to compare the capabilities of three computational electromagnetic codes for use in production of RCS signature assessments at low frequencies in terms of performance, accuracy, and features Fast Illinois Solver Code (FISC), Code for Analysis of Radiators on Lossy Surfaces (CARLOS-3D), and Science Applications International Corporation Fullwave solver (SAF). The comparison is accomplished through analysis of predicted and measured RCS of several canonical and simple objects and a complex target comprised of these constituent objects. In addition to RCS accuracy, memory requirements and computation time are key considerations for this code comparison. Verification of code performance in memory and processing time based on varying levels of unknowns is performed. A 1/36 scale body-ofrevolution missile model is the complex model constructed for measurement and prediction. The model corresponds to an 18-meter full-scale target and includes a cavity allowing mode propagation at frequencies of interest. The complex model is simulated at 400 and 500 MHZ corresponding to a 24 and 30 lambda target length, respectively. RCS of each constituent part of the model is also analyzed to establish a level of confidence in solution accuracy. Solution convergence is shown using increasing discretization levels. A comparison is also conducted between measured and predicted results for two PEC objects coated with magnetic radar absorbent material (MRAM). The RCS for a 12″?12″ MRAM-coated PEC flat plate and a 9″?9″ MRAM-coated PEC right circular cone are measured in the Air Force Research Laboratory?s compact RCS/antenna measurement range and then compared to results from FISC using its impedance boundary condition (IBC) feature. A physical optics method for predicting RCS of a material-coated PEC plate is also developed as a third data. The IBC formulation is generalized for polarization and angle-dependent impedances to investigate prediction improvement. Results of each part of the comparison are presented as well as the methodology used to evaluate the codes.

15. SUBJECT TERMS

16. SECURITY CLASSIFICATION OF:			17. LIMITATION OF ABSTRACT	18. NUMBER OF PAGES	19a. NAME OF RESPONSIBLE PERSON
a. REPORT	b. ABSTRACT	c. THIS PAGE		**166**	
unclassified	**unclassified**	**unclassified**			

AFIT/GE/ENG/06-32

COMPARISON OF COMPUTATIONAL ELECTROMAGNETIC CODES FOR
PREDICTION OF LOW-FREQUENCY RADAR CROSS SECTION

THESIS

Presented to the Faculty

Department of Electrical and Computer Engineering

Graduate School of Engineering and Management

Air Force Institute of Technology

Air University

Air Education and Training Command

In Partial Fulfillment of the Requirements for the

Degree of Master of Science in Electrical Engineering

Paul C. Lash, B.S.E.E.

Captain, USAF

March 2006

APPROVED FOR PUBLIC RELEASE; DISTRIBUTION UNLIMITED

AFIT/GE/ENG/06-32

COMPARISON OF COMPUTATIONAL ELECTROMAGNETIC CODES FOR
PREDICTION OF LOW-FREQUENCY RADAR CROSS SECTION

Paul C. Lash, B.S.E.E.
Captain, USAF

Approved:

//signed//	
Dr. Michael J. Havrilla (Chairman)	Date

//signed//	
Dr. Kueichien Hill (Member)	Date

//signed//	
Dr. Andrew J. Terzuoli (Member)	Date

//signed//	
Dr. William P. Baker (Member)	Date

AFIT/GE/ENG/06-32

Abstract

Radar cross section (RCS) prediction of full-scale aircraft is of interest to military

planners for a variety of applications. Several computational electromagnetic codes for

RCS prediction are available with differing features and capabilities. The goal of this

research is to compare the capabilities of three computational electromagnetic codes for

use in production of RCS signature assessments at low frequencies in terms of

performance, accuracy, and features: Fast Illinois Solver Code (FISC), Code for

Analysis of Radiators on Lossy Surfaces (CARLOS-3D), and Science Applications

International Corporation Full-wave solver (SAF). The comparison is accomplished

through analysis of predicted and measured RCS of several canonical and simple objects

and a complex target comprised of these constituent objects. In addition to RCS

accuracy, memory requirements and computation time are key considerations for this

code comparison. Verification of code performance in memory and processing time

based on varying levels of unknowns is performed. A 1/36 scale body-of-revolution

missile model is the complex model constructed for measurement and prediction. The

model corresponds to an 18-meter full-scale target and includes a cavity allowing mode

propagation at frequencies of interest. The complex model is simulated at 400 and 500

MHZ corresponding to a 24 and 30 lambda target length, respectively. RCS of each

constituent part of the model is also analyzed to establish a level of confidence in solution

accuracy. Solution convergence is shown using increasing discretization levels. A

comparison is also conducted between measured and predicted results for two PEC

objects coated with magnetic radar absorbent material (MRAM). The RCS for a $12''\times12''$

MRAM-coated PEC flat plate and a $9''\times9''$ MRAM-coated PEC right circular cone are

measured in the Air Force Research Laboratory's compact RCS/antenna measurement range and then compared to results from FISC using its impedance boundary condition (IBC) feature. A physical optics method for predicting RCS of a material-coated PEC plate is also developed as a third data. The IBC formulation is generalized for polarization and angle-dependent impedances to investigate prediction improvement. Results of each part of the comparison are presented as well as the methodology used to evaluate the codes.

Acknowledgments

Table of Contents

List of Figures

List of Tables

Equation Section 1

1   Introduction

Radar cross section (RCS) prediction of aircraft is vital to the United States Air Force for operational planning and system design. Numerous computational electromagnetic codes are available to perform this task that offer varying levels of performance, unique features, and capabilities. The goal of this research is to compare the capabilities of three computational electromagnetic (CEM) codes for use in production of RCS signature assessments at low frequencies in terms of performance, accuracy, and features: Fast Illinois Solver Code (FISC), Code for Analysis of Radiators on Lossy Surfaces (CARLOS-3D), and Science Applications International Corporation (SAIC) Full-wave solver (SAF).

Obtaining RCS data can be accomplished via measurement or prediction. There are tradeoffs for either method of acquiring signature data. Experimental measurement of RCS is costly and rarely yields complete data sets for every aspect angle and frequency of interest. RCS measurement also presents a host of complexities and data qualifications. For example, RCS data customers must decide whether static or dynamic measurements are desired. Both static and dynamic measurements must contend with the presence of clutter. With static measurements, clutter can be more precisely characterized using techniques such as vector background subtraction and careful attention to target-mount interactions. Dynamic measurements, on the other hand, include real effects on RCS from rotating turbines, wing flex, and control-surface movement. RCS CEM prediction is inherently immune to clutter contamination but is also a static process which neglects the RCS effects of target movement. Radar range facilities are expensive, have limited availability, and each has a finite measurement

capability. From an intelligence standpoint, foreign weapons systems are simply not available for measurement and exploitation. Due to cost, availability, capability, and many other reasons, RCS prediction is essential to building databases of RCS profiles of foreign aircraft in support of integrated defense system development and performance of threat assessment.

1.1 Problem statement

The sponsor for this research, the Signatures Branch of the National Air and Space Intelligence Center (NASIC/AENS), currently uses FISC to predict RCS for targets of interest. RCS data is generated for a bandwidth of interest and sector averaging (azimuth and elevation) is used to provide RCS signatures at certain target aspects. Low frequency radars play an integral role in ballistic missile defense and integrated air defense systems. Consequently, NASIC has a growing number of requirements to perform low frequency radar signature assessments on foreign aerodynamic and ballistic missile systems. NASIC is interested in using the best suited RCS prediction code to perform these assessments.

This thesis compares FISC, CARLOS-3D and SAF through RCS prediction and measurement of several simple, canonical, and complex objects. Accuracy is compared by quantitative and qualitative comparisons between predicted and measured data. Memory requirements and computation time are examined for targets of varying sizes. A 1/36 scale body-of-revolution missile is the complex model constructed for measurement and prediction. The model corresponds to an 18 meter full-scale target and includes a cavity allowing mode propagation at frequencies of interest. The complex model RCS is predicted at 400 and 500 MHZ corresponding to a 24-wavelength (λ) and 30λ target

length, respectively. Two constituent parts of the complex model, a cylinder and a cone, have well-known RCS patterns. RCS of each constituent part of the model is predicted and measured to establish a level of confidence in solution accuracy. Solution convergence is shown using increasing discretization levels. A comparison was also conducted between measured and predicted results for two PEC objects coated with magnetic radar absorbent material (MRAM). The RCS for a 12″×12″ MRAM-coated PEC flat plate and a 9″×9″ MRAM-coated PEC right circular cone are measured in Air Force Research Laboratory's (AFRL's) compact RCS/antenna measurement range and then compared to results from FISC using its impedance boundary condition (IBC) feature. A physical optics (PO) method for predicting RCS of a material-coated PEC plate is also developed as a third data set. The IBC formulation is generalized for polarization and angle-dependent impedances to investigate prediction improvement. Results of each part of the comparison are presented as well as the methods used to evaluate the codes.

1.2   *Thesis Organization*

The following section is an overview of the composition of this thesis. Chapter 2 starts with CEM code background information and brief descriptions of FISC, CARLOS, and SAF. Next, the chapter provides theoretical background information pertaining to RCS, a brief treatment of the Method of Moments (MoM), and specifics on CEM code modeling of physical targets. The chapter continues with a derivation of a PO approximation for a material-coated flat PEC plate, and a discussion of IBCs. Chapter 2 concludes with an explanation of two metrics used to compare the measured and predicted RCS results. Chapter 3 describes the methodology for characterizing the three

codes through the RCS prediction and measurement of several objects. Chapter 4

discusses results of the characterization described in Chapter 3. Finally Chapter 5

provides conclusions based on the analysis performed in Chapter 4 and recommendations

for future work.

2   Background

This chapter provides a theoretical background for each of the topics discussed in chapter 3. Sections 2.1 through 2.5 provide background information and brief descriptions of FISC, CARLOS, and SAF. Sections 2.6 through 2.14 describe terms pertinent to RCS with some mathematical rigor to establish a basis for discussion and further development. These sections also describe assumptions made when analyzing RCS and why the assumptions can be made. Section 2.15 discusses target modeling requirements and parameters for the CEM codes being considered. Section 2.16 gives a brief treatment of the Method of Moments for computation of RCS. Sections 2.17 and 2.18 explain resource requirements in terms of memory and processing time. Section 2.19 derives a PO approximation for a material-coated PEC flat plate. Section 2.20 provides a short derivation of impedance boundary conditions.Equation Section 2

2.1   CEM Code Types

Full-wave CEM codes, also known as *exact codes*, *full-wave solvers*, or *low-frequency codes*, use integro-differential equations, which are based on Maxwell's equations, discretized to a specific target geometry to numerically solve for the induced electrical currents on the surface of arbitrarily shaped targets due to incident electromagnetic radiation. Approximations are kept to a minimum and are due to:

- the process of converting continuous integro-differential equations into discrete matrix-vector products, (MoM – directly related to target geometry precision)
- truncation of infinite series representations,
- the numerical precision of the processor,

and

- the number of operations that must be performed (computational noise increases with the number of operations).

The other major CEM category is approximate codes, also known as *asymptotic* or *high-frequency* codes. Approximate codes, as the name implies, is based on an approximation to Maxwell's equations. Examples include physical optics (PO), geometrical optics (GO), physical theory of diffraction (PTD), uniform theory of diffraction (UTD), or hybrid methods to compute RCS. The underlying assumption for approximate codes is that the target size and curvature is very large compared to wavelength. Since wavelength, λ, is equal to the speed of light divided by frequency, i.e. $\lambda = c / f$, this requirement implies high frequency hence the term *high-frequency* codes. Approximate codes are popular for their ability to rapidly solve (with reasonable accuracy) problems that are considered too *large* for full-wave codes. Approximate codes typically do not calculate second order diffraction mechanisms and yield poor results for cavities [16]. For low signature targets, these mechanisms become more important. Also, due to the underlying high-frequency assumption, approximate codes cannot be used when the target is small with respect to wavelength. Full-wave codes, on the other hand, take all scattering mechanisms into account, for example, traveling & creeping waves, tip & edge diffraction, etc. Which category of code is best suited to the application depends mostly on the electrical size of the object (see section 2.7, Scattering Regimes).

2.2   *Sizing up MoM codes*

So what is a *large* problem, and why do MoM codes require more time and
computer resources? For a given target geometry, the computational requirements in
memory and processing time are proportional to the frequency squared (explained in
detail in section 2.17). For this reason, the computational problem size is often put in
terms of a target's longest dimension in wavelengths, also known as electrical size.
Problems larger than $30\,\lambda$ are difficult to solve in a reasonable amount of time without
the aid of parallel processing. Predicting RCS of targets on the order of a full-scale
fighter aircraft at normal operational frequencies such as X-band (8-12 GHz) with a full-
wave code exceeds the capabilities of most supercomputer resources [16]. These initial
roadblocks are just a foreshadowing of the complexity of RCS signature assessment
production. Frequency-averaging of RCS is usually needed over the bands used by
operational radars, thus multiplying the effort of the original task by the number of
individual frequencies required. Nyquist sampling criteria increases the number of aspect
angles required to capture lobing in RCS as targets grow electrically larger, and material
coatings significantly complicate and increase computational requirements. How a
vehicle's RCS changes with surface variations is also of interest. Given these
multiplicative resource requirements for one target alone, meeting RCS production for a
host of targets can be a daunting task! Time and resource constraints prevent full
exploration of all possibilities of target variations based upon available intelligence data.

2.3   **FISC version 1.7**

FISC is a method of moments, full-wave CEM code for computing the RCS of
targets that are geometrically discretized using triangular facets. FISC was developed by

the University of Illinois Center for Computational Electromagnetics at Urbana-Champaign and Demaco Inc. Using the surface equivalence principle, surfaces that describe the target geometry are replaced by an equivalent electrical current density ($\vec{J}_s$) to maintain the same fields as those scattered by the object replaced. Surface currents are computed using surface integrals in the form of an electric field integral equation (EFIE), magnetic field integral equation (MFIE), or combined field integral equation (CFIE). In the derivation of the EFIE or MFIE, the boundary condition for either the tangential electric or magnetic field is enforced. Individually enforcing boundary conditions can result in incorrect solutions near frequencies where the surface represents a resonant cavity(a natural solution which is in the null space of the forced solution). At these frequencies, the solution is not unique. This phenomenon is called the internal resonance problem of the EFIE and the MFIE [3]. An MFIE can only be used on closed surfaces. This requirement arises from the MFIE formulation for an open surface giving rise to both common mode and differential mode currents. This presents an ill-posed problem where there is one equation with a two unknown currents. This problem is not present for an EFIE since boundary conditions at a perfect electrical conductor (PEC) interface require the electric field to be identically equal to zero (leading to a common-mode current only). Therefore, the EFIE can be used on open or closed surfaces. The Combined Field Integral Equation, CFIE, was developed to provide unique, stable solutions for all closed geometries. A CFIE is a linear combination of an EFIE and an MFIE defined as: $\alpha\,EFIE + \left(1-\alpha\right)MFIE$ where the α parameter determines the ratio of EFIE to MFIE. The α parameter range is $0 < \alpha < 1$ and typically is set to 0.5. Setting

α to zero or one reduces the CFIE to an MFIE or EFIE, respectively. Since the CFIE uses both the MFIE and EFIE it is valid only for closed surfaces.

Once the surface currents are known, the scattered fields can be calculated. Rao, Wilton and Glisson (RWG) basis functions, i.e. expansion functions, are used to represent the currents along the N shared edges of the triangular facets comprising the target geometry [13] .

MoM converts the continuous surface integral equations into discrete matrix-vector products. The challenge in using MoM is the computational intensity required to invert a matrix representing impedance across the surface of the scatterer. Full-matrix inversion using Gaussian elimination or Lower Upper Decomposition (LUD) requires N^3 operations and $O(N^2)$ in memory to store the matrix. To reduce this computational complexity, FISC does not invert or store this impedance matrix, but rather solves iteratively for the surface currents. This iterative process, if Galerkin testing is used, employs methods such as the conjugate gradient (CG) where the solution is found through matrix-vector multiplication and residual error reduction. Iterative methods such as this reduce computational complexity from $O(N^3)$ operations to $O(N^2)$. The total number of operations for this iterative method is N^2 operations to perform each matrix-vector product times the number of iterations required to reach an acceptable residual. The Fast Multipole Method (FMM) accelerates the process and reduces computational complexity to $O(N^{1.5})$. The Multi-level Fast Multipole Algorithm (MLFMA) is an extension of FMM to higher levels and further reduces complexity to $O(N \log N)$ for both memory and solution time. Although FISC is a serial code, a utility

called Scalable Multipole Engine (ScaleME) has been developed to allow FISC to be scaled to run on parallel processing nodes. For more information on ScaleME, the reader is referred to Hastriter [16]. FISC's MLFMA offers the capability to solve very large scale problems even when using the serial version of the code. Problem size is limited only by memory resources and solution time. FISC's version 1.7 material-handling capability is limited to integral equation formulations based on impedance boundary conditions (IBCs), thin dielectric sheets and resistive boundary conditions. Bulk material capability, i.e. volumetric currents is not supported. Other capabilities include the ability to produce monostatic or bistatic RCS, far-field or near field solutions, bistatic to monostatic approximation, and facet output files showing the current distribution across a surface. Refer to [13] for a comprehensive description of FISC's capabilities.

2.4   CARLOS_3D_BOR_2D (CFDMAXES/PICASSO) Version 4.4.1™

CARLOS_3D_BOR_2D (CFDMAXES/PICASSO) Version 4.4.1™ (hereafter referred to simply as CARLOS-3D or CARLOS-BOR as applicable) is a three-dimensional MoM code based on the Stratton-Chu and Maue surface integral formulations [18].   The software is Boeing proprietary and is subject to export control laws under the International Traffic-in-Arms Regulations (ITAR). CARLOS is a parallel code capable of using multiple nodes to reduce solution time. For conducting surfaces, EFIE, MFIE or a CFIE formulation can be used. A versatile feature offered by CARLOS is the ability to individually specify the alpha parameter used in the CFIE formulation for each surface. This capability allows a CFIE to be used for geometries with both open and closed conducting surfaces. As with FISC, CARLOS has an iterative solver, although this feature was not exercised in this research. CARLOS offers the ability to handle

materials using IBCs, surface integral equations, and volumetric integral equations and accepts permittivity and permeability parameters. It supports many geometry types including triangular facets, quadrilateral facets, two-dimensional bodies of translation, body of revolution, and mixed BOR/facetized geometries. CARLOS has the ability to produce monostatic or bistatic RCS, far-field or near field solutions, and output files listing current distribution across a surface or volume currents along edges in a volumetric mesh. Another capability of CARLOS is that the impedance matrix for 2D, BOR, and 3D-PATCH geometries is generated as needed without the need to store the matrix. This feature reduces the memory requirement. CARLOS version 4.4.1 was used in this thesis and has a hard-coded 70k edge limit. At the time of publication, CARLOS version 5.2 was available for use within AFRL. This constraint limits the problem size for triangular facet files. Therefore, in this research a body of revolution missile model was chosen so that a BOR model of the missile could be used. CARLOS is non-intuitive for the novice but a graphical user interface is available to assist with the creation of input pages. CARLOS does not have FMM or MLFMA functionality and therefore requires substantial resources in terms of processing nodes, memory and processing time to solve large-scale problems. Refer to [17,17] for additional information on CARLOS.

2.5 *SAF Version 3.1*™

SAIC's Full-wave solver (SAF) is an extension of FISC. It incorporates all features of FISC and adds some new capabilities. SAIC currently provides SAF to the Department of Defense upon request free of charge and like CARLOS, SAF is proprietary and subject to export control laws under ITAR. SAF offers the capability to handle mixed geometry types for modeling higher-order surfaces. Triangular facets with

3 or 6 nodes and quad facets with 4 or 9 nodes are accommodated. The higher node count allows for curvilinear facet edges. Automatic mesh refinement is not available for curvilinear edges or quad facets. SAF includes the ability to handle bulk materials with volumetric meshes composed of tetrahedron pyramids or bricks. As opposed to FISC, SAF will accept permittivity and permeability values for resistive sheets and calculate the resistance. An exciting feature that has been implemented in SAF is the hybridization of SAF with Xpatch® (SAIC/Demaco's high-frequency/asymptotic RCS prediction code) via a method called "Crossflux". RCS of grouped targets of varying sizes are addressed by this hybridization where Xpatch® is used for the larger targets, SAF is used for the smaller targets and the interactions are computed using the Crossflux formulation. SAF with Crossflux is not yet publicly available and was not examined in this thesis [19].

2.6   Radar Cross Section

This section will provide the theoretical background for discussion of RCS (σ). Consider the target acquisition radar illuminating a target in Figure 2-1.
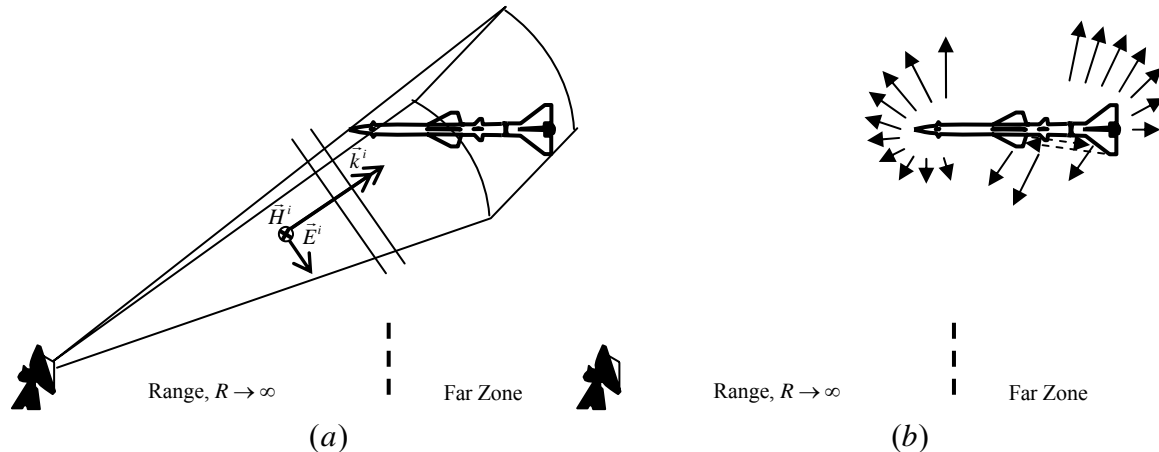
Figure 2-1: (a) Plane wave incident on target (b) Target captures a portion of the incident power $\propto \sigma$ and reradiates with scattered fields (depicted by the arrows) dependent on target shape and material properties.

The radar and target are assumed to be distant from one another so that the wavefront incident upon the target is approximately uniformly planar. RCS is the equivalent aperture surface area of a target which captures a portion of the incident field and would produce an equivalent scattered field at the receiver if radiated isotropically. The aperture surface area can be thought of as the surface area of an equivalent sphere radiating the same scattered field back to the receiver as the target.

$$\sigma_{target} \qquad = \qquad \sigma_{equivalent\ sphere}$$
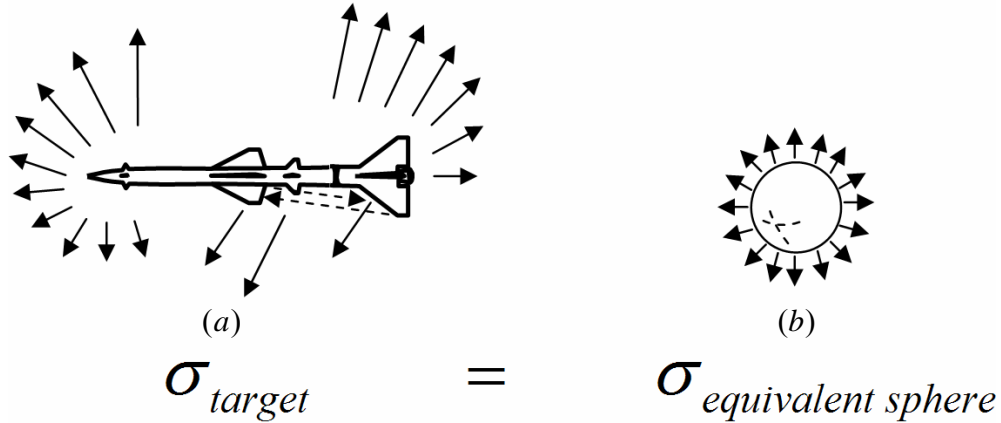
Figure 2-2: (a) Target re-radiating captured energy (b) Equivalent sphere radiating to produce an equivalent scattered field at the receiver.

RCS is defined in units of square meters as follows [4]:

$$\sigma = \frac{\text{power scattered toward source/unit solid angle}}{\text{incident power density/}4\pi} \tag{2.1}$$

More often, RCS is defined in terms of the scattered and incident fields:

$$\sigma = \lim_{R_r \to \infty} 4\pi R^2 \frac{|\hat{e} \cdot \vec{E}_s|^2}{|\vec{E}_i|^2}, \tag{2.2}$$

where R is the range to the target, $\vec{E}_s$ is the electric field strength scattered from the target back to the receiving antenna, $\vec{E}_i$ is the electric field strength incident upon the target and $\hat{e}$ is the unit polarization vector of the receiving antenna. Polarization is

defined in section 2.10. As alluded to above, RCS is a far-field quantity, meaning that R

is sufficiently large that the wavefront of the incident electromagnetic wave is considered

approximately planar rather than spherical. As an example, Figure 2-3 shows an RCS

range employing a rear reflector to achieve a planar wave front versus use of a single

microwave antenna to transmit a spherical wave front. See section 2.9 for further

discussion of plane waves.
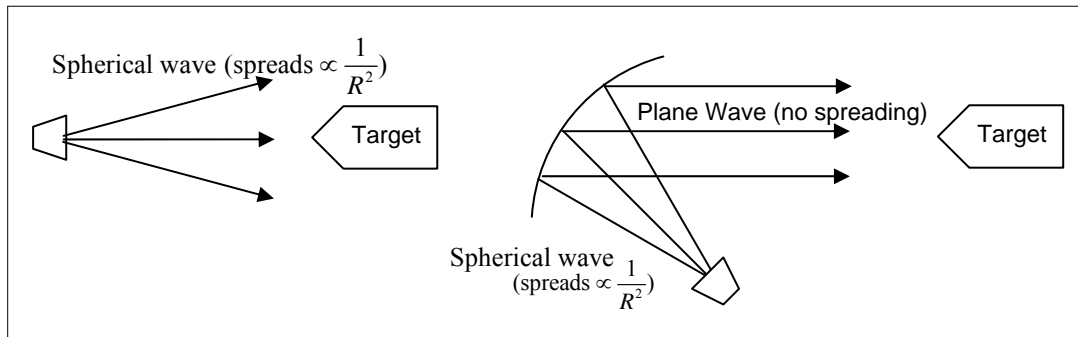
Figure 2-3: Spherical wave spreading versus plane wave propagation

Monostatic RCS, developed below, assumes that the transmitter is collocated with the

receiver. For this thesis, only monostatic RCS signatures are considered. For a treatment

of bistatic RCS of complex objects see Eigel [9].
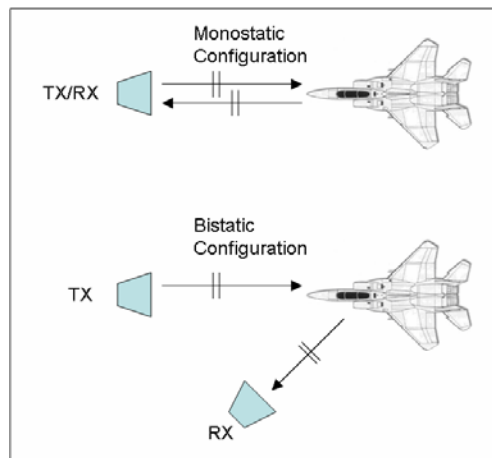
Figure 2-4: Monostatic versus bistatic geometry

2.7 Radar Range Equation and RCS Definition

Given that the transmitted wave is planar because the target is located sufficiently far from the receiver, a simple derivation of the RCS definition given in equation (2.2) can be shown [6]. The meaning of 'sufficiently far' is given in section 2.11, Far-Field criterion. The power transmitted by the radar, measured in watts is given by:

$$P_t \qquad \text{(Watts)}. \tag{2.3}$$

Power density transmitted by an isotropic antenna is the transmitted power divided by 4π steradians and by the inverse square of the distance from the transmitter to the target:

$$\text{Transmitted power density (isotropic)} = \frac{P_t}{4\pi R_t^2} \qquad \text{(Watts/m}^2), \tag{2.4}$$

where a steradian (Sr) is the unit of solid angle. Solid angle is defined as the area subtended by a cone centered at the origin of a sphere divided by the square radius of the sphere. An entire unit sphere has a solid angle of 4π steradians.
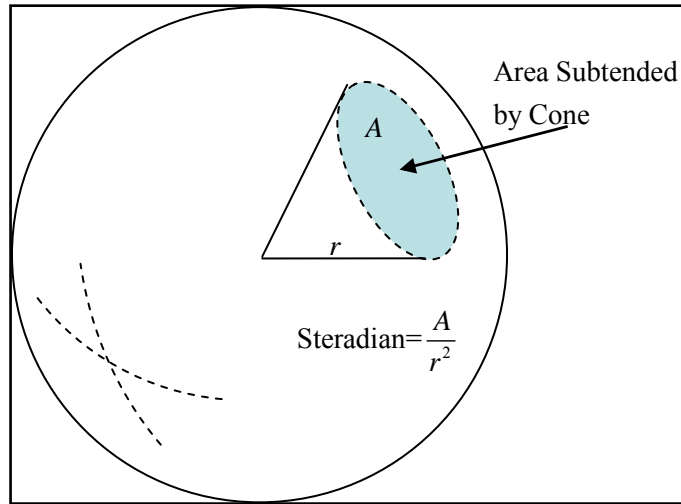
Figure 2-5: Steradian definition

For a non-isotropic or directional antenna, the transmitted power density is:

$$\text{Transmitted power density (directional)} = \frac{P_t G_t}{4\pi R_t^2} \qquad (\text{Watts/m}^2), \qquad (2.5)$$

where G_t is a unitless quantity describing the gain of the transmit antenna. Equation (2.5) gives the power density transmitted by the antenna, now we must consider how much of the energy is incident upon or captured by the target aperture. This target aperture is the target's RCS, σ. RCS is the target's ability to reradiate electromagnetic energy and is a function of many factors including frequency and polarization of incident wave, target shape, target size, and material composition.

$$\text{Power density on target (aperture)} = \frac{P_t G_t}{4\pi R_t^2} \qquad (\text{Watts/m}^2) \qquad (2.6)$$

After reradiating from the target, the energy is backscattered to the receiver. Here (2.7) we insert the variable σ for RCS and later will solve for σ in terms of the other known values in the radar range equation. Equation (2.7) is the expression for the power scattered back to the receiver from the target. Once again, the power is diminished by the inverse square of the distance:

$$\text{Power Density at Receiver} = \frac{P_t G_t \sigma}{4\pi R_t^2} \times \frac{1}{4\pi R_r^2} \quad (\text{Watts/m}^2), \qquad (2.7)$$

R_r is the distance from the target back to the receiver. Since this development is for monostatic RCS, the receiver antenna is at the same location as the transmitter. Now just as we considered the ability of the target to capture radiated RF energy, we must also consider the ability of the antenna to do the same. A_e is the effective aperture of a receiver antenna, a measure of the antenna's ability to capture radiated energy:

$$A_e = \frac{\lambda^2 G_r}{4\pi}. \qquad (2.8)$$

Multiplying (2.7) by (2.8) results in (2.9), the portion of the energy scattered by the target that is captured by the receiver:

$$\text{Power at receiver } = \frac{P_t G_t \sigma}{4\pi R_t^2} \times \frac{1}{4\pi R_r^2} \times \frac{\lambda^2 G_r}{4\pi} \quad \text{(Watts)}. \tag{2.9}$$

With all quantities known except for RCS, we solve for σ:

$$\sigma = \frac{(4\pi)^3 P_r R_t^2 R_r^2}{P_t G_t G_r \lambda^2} \quad (\text{m}^2). \tag{2.10}$$

We wish to put σ in terms of incident and scattered fields. Equation (2.5) can be written in terms of the incident field and the intrinsic impedance of free space:

$$\frac{\left|\vec{E}_i\right|^2}{2\eta_0} = \frac{P_t}{4\pi R_t^2} \quad (\text{Watts/m}^2) \tag{2.11}$$

Similarly, power density returning to the receiving antenna incident upon the target can be written in terms of the incident field and the intrinsic impedance of free space:

$$\frac{\left|\vec{E}_s\right|^2}{2\eta_0} = \frac{P_r}{A_e} = \frac{P_r 4\pi}{\lambda^2 G_r} \quad (\text{Watts/m}^2) \tag{2.12}$$

Substituting (2.11) and (2.12) into (2.10) and allowing $R_r = R$ yields:

$$\sigma = 4\pi R^2 \frac{\left|\vec{E}_s\right|^2}{\left|\vec{E}_i\right|^2}. \tag{2.13}$$

To ensure the target is in the far-field, it is necessary to impose the limit as $R_r \to \infty$. Polarization dependence can now be incorporated into the RCS definition. Therefore, RCS is mathematically defined in terms of complex scattered field quantities is:

$$\sigma = \lim_{R_r \to \infty} 4\pi R_r^2 \frac{\left|\hat{e} \cdot \vec{E}_s\right|^2}{\left|\vec{E}_i\right|^2}, \tag{2.14}$$

where $\hat{e}$ is the unit polarization vector of the receive antenna.

In section 2.19.1 and 2.19.2 it is shown that the scattered field $\vec{E}_s$ can be written in terms of the incident electric field, $\vec{E}_i$, such that RCS is normalized and independent of the magnitude of $\vec{E}_i$. It will also be shown in equation (2.77) that if the target is in the radiation zone, otherwise known as far field, RCS is not a function of range. RCS values generally have a large dynamic range. For this reason, graphs showing RCS in this research are shown in decibels per square meter (dBsm):

$$\sigma_{dBsm} = 10 \log_{10} \left(\frac{\sigma[m^2]}{1 \, m^2} \right). \tag{2.15}$$

2.8   RCS and Range Profile

Complex voltages determined either by measurement or prediction can be processed to create either RCS plots or images. An RCS plot displays σ versus azimuth (AZ) or elevation (EL) for a target exposed to a fixed transmit frequency (FREQ). A range profile (a.k.a. impulse response) can be made by sweeping across a band of frequencies at a specific azimuth angle and performing an inverse Fourier transform. RCS and range profile plots are referred to as one-dimensional since they provide scattering information about the target in only one dimension. For a range profile, a complex in-phase and quadrature voltage is determined (measurement or prediction) for each transmitted frequency. This frequency-sampled data can be converted to time-sampled data using an inverse Fourier transform. Taking the absolute value of the data

and converting time to range yields the range profile. Range profiles and RCS plots will be used in chapter 4. Synthetic aperture radar (SAR) images can be made when the transmitter sweeps across frequency and changes its location relative to a fixed target. In the case of a static radar range, an inverse SAR (ISAR) image can be created where the transmitter is fixed and the target rotates relative to the radar. SAR and ISAR are referred to as 2-D or 3-D images (3-D image also called a scattering center plot). A 3-D image can be created when all degrees of freedom are varied: frequency, azimuth and elevation. These image types are summarized in Table 2-1. As is the case with RCS, range profiles are generally expressed in dBsm.

Table 2-1: Types of scattering plots

Dim.	Plot Type	Fix	Sweep	Example
0-D	RCS	FREQ, AZ, EL	-	1 GHz, 0° AZ, 0°EL
1-D	RCS (AZ)	FREQ	AZ	1 GHz, 0:(0.5):360°
1-D	RCS (EL)	FREQ	EL	1 GHz, -90:(0.5):90°
1-D	Range Profile (AZ)	AZ	FREQ	30° AZ, 2-18GHz
1-D	Range Profile (EL)	EL	FREQ	30° EL, 2-18GHz
2-D	SAR/ISAR (AZ)	-	AZ, FREQ	0:0.5:30°, 2-18GHz
2-D	SAR/ISAR (EL)	-	EL, FREQ	0:0.5:30°, 2-18GHz
3-D	SAR/ISAR (a.k.a. Scattering Center plot)	-	AZ, EL, FREQ	-30:0.5:30°, AZ -30:0.5:30°, EL 2-18GHz

2.9   TEM Waves and Plane Waves

In this section it is important to understand the concept of polarization of a plane wave with respect to the scattering object. To understand this, transverse electromagnetic (TEM) waves need to be defined. A *TEM* wave is one whose electric and magnetic fields are transverse to the direction of wave propagation. The electric and magnetic field components are in a plane transverse to the propagation vector, $\vec{k}$.
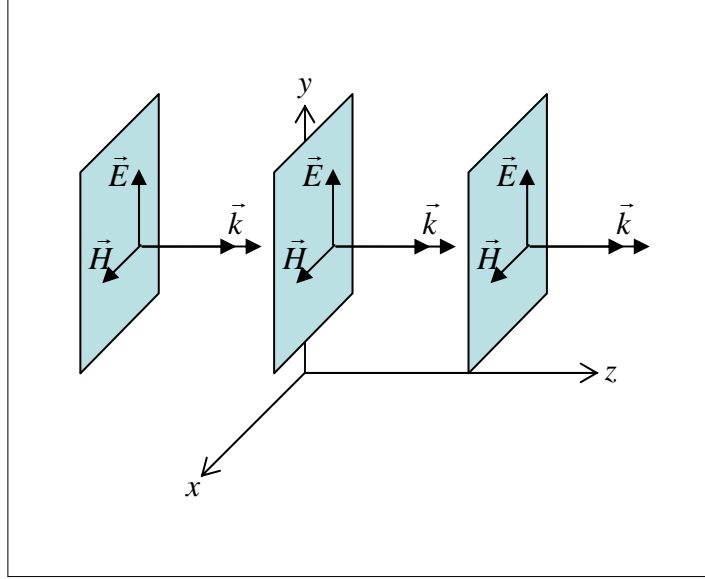
Figure 2-6: Equiphase plane fronts of TEM^Z plane wave

If phase fronts are planar the *TEM* wave is called a plane wave as illustrated in Figure

2-6. Depicted are equiphase parallel planes with field vectors of equal amplitude in each

plane. In the Cartesian coordinate system used in Figure 2-6, the plane wave is

transverse to the z-coordinate direction, and is referred to as *TEM^Z*.

2.10 Plane Wave Polarization

Consider a plane wave upon a planar surface. As shown in Figure 2-7, the plane of

incidence is defined by $\hat{n} \times \vec{k}^i$ or otherwise stated, the plane containing both $\hat{k}^i$, the unit

direction vector in the direction of plane-wave propagation, and the surface normal, $\hat{n}$ [4].
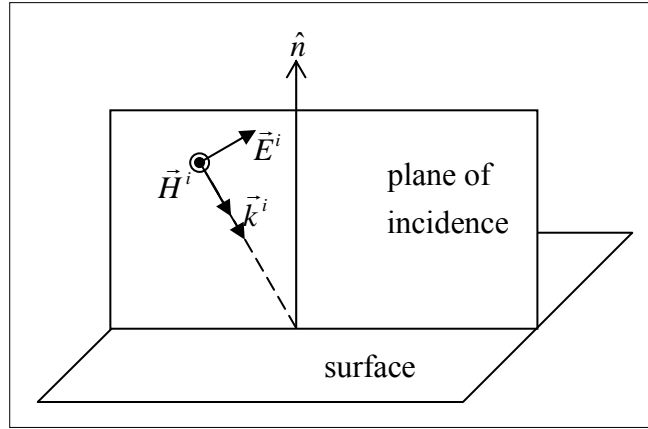
Figure 2-7: Plane of incidence and parallel polarization

Electric field polarization relates orientation of the electric field, $\vec{E}^i$, to plane of

incidence. For parallel polarization, the incident electric field lies in the plane of

incidence as shown in Figure 2-7. Conversely, for perpendicular polarization, the

incident electric field is perpendicular to the plane of incidence as shown in Figure 2-8.
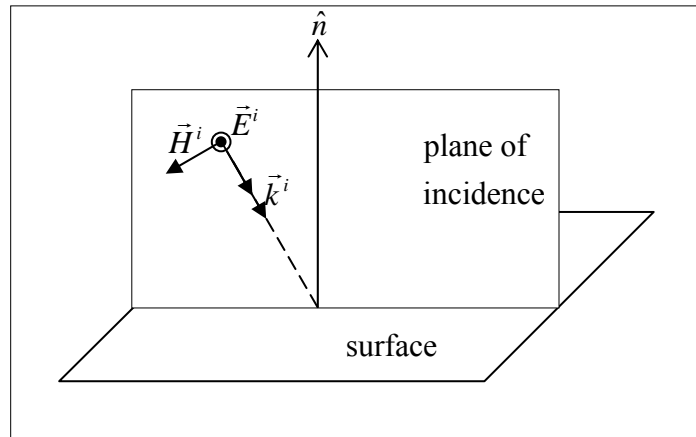
Figure 2-8: Plane of incidence and perpendicular polarization

The magnitude of $\vec{k}$ is defined as the wave number, k, which describes how the wave is

propagating in terms of attenuation, phase velocity, and dispersion as shown in equations

(2.16) and (2.19). For the Cartesian coordinate system, k has components in the x, y and

z directions. The relationship between k and its components is known as the constraint

equation [1]:

$$k^2 = k_x^2 + k_y^2 + k_z^2 \Rightarrow k = \sqrt{k_x^2 + k_y^2 + k_z^2} \ . \tag{2.16}$$

The wave number is a function of frequency, permeability, and permittivity. Permittivity, ε, is related to electric susceptibility, a measure of the sensitivity of a medium to become electrically polarized in the presence of an electric field:

$$\varepsilon = \varepsilon_0 (1 + \chi_e) = \varepsilon_0 \varepsilon_r \ . \tag{2.17}$$

where χ_e is electric susceptibility, ε_0 is the permittivity of free space, and ε_r is the relative permittivity of the medium. Permeability, μ, is related to magnetic susceptibility, a measure of the sensitivity of a medium to become magnetically polarized in the presence of a magnetic field:

$$\mu = \mu_0 (1 + \chi_m) = \mu_0 \mu_r \ . \tag{2.18}$$

where χ_m is magnetic susceptibility, μ_0 is the permeability of free space, and μ_r is the relative permeability of the medium. The notation for k in free space is k_0 and correspondingly is a function of ε_0 and μ_0:

$$k = \omega \sqrt{\mu \varepsilon} \Rightarrow k_0 = \omega \sqrt{\mu_0 \varepsilon_0} = 2\pi \frac{f}{c} = \frac{2\pi}{\lambda} \quad (\text{m}^{-1}), \tag{2.19}$$

where μ_0 is defined as

$$\mu_0 \equiv 4\pi \times 10^{-7} \qquad\qquad (\text{henries/meter}), \tag{2.20}$$

the speed of light, c, is measured as

$$c \approx 2.997925 \times 10^8 \qquad\qquad (\text{meters/sec}), \tag{2.21}$$

and permittivity is calculated to be

$$\varepsilon_0 = \frac{1}{c^2 \mu_0} \approx 8.854 \times 10^{-12} \qquad\qquad (\text{farads/meter}) . \tag{2.22}$$

The speed of light, in terms of permeability and permittivity of free space (2.20), is

$$c = f\lambda = \frac{1}{\sqrt{\varepsilon_0 \mu_0}} \approx 2.997925 \times 10^8 \qquad \text{(meters/sec)} .$$

(2.23)

2.11 Far-Field Criterion

In order to meet the requirement that waves are planar, the target must be located sufficiently far away from the transmitter such that the incident wavefront is considered planar. For indoor ranges, the rule of thumb for minimum acceptable range is

$$R > \frac{2D^2}{\lambda} .$$

(2.24)

This specification [6] places a restriction on phase error. It can be derived by examining the geometry given in Figure 2-9 and noting the relationships between R, D, and x using the Pythagorean theorem:

$$(R+x)^2 = R^2 + \left(\frac{D}{2}\right)^2 ,$$

(2.25)

where R is the distance from the receiver to the target, D is the maximum dimension of the target aperture and x is the additional distance a wave must travel if the wave were planar. While traveling this extra distance, the phase of the incident field changes at the rate of 2π radians per wavelength traveled as given in (2.19). The phase difference between the wavefront at the center of the plate and at the edge is referred to as cross-range phase variation.
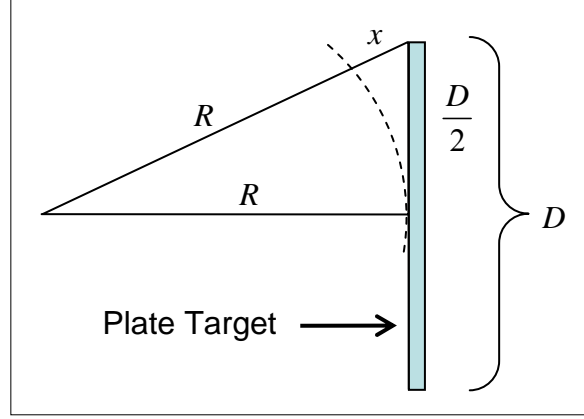
Figure 2-9: Cross-range phase variation

Noting that x is small compared to R, solving for R yields:

$$(R + x)^2 = R^2 + \left(\frac{D}{2}\right)^2 \qquad (2.26)$$

$$R^2 + 2Rx + x^2 = R^2 + \frac{D^2}{4}$$

$$\text{since } x \ll R$$

$$R = \frac{D^2}{8x}$$

Knott [4] states that if a complex target can be represented by a collection of discrete scatterers, the composite return at a given frequency is

$$\sigma = \left| \sum_{n=1}^{N} \sqrt{\sigma_n} e^{j\Phi_n} \right|^2, \qquad (2.27)$$

where σ_n is the RCS of the nth scatterer and Φ_n is the relative phase of that particular contribution due to its physical location. The relative phase, Φ, between the target center and the edge is related to the distance x by the relationship:

$$\Phi = kx = \frac{2\pi}{\lambda} x \Rightarrow x = \frac{\lambda \Phi}{2\pi} \qquad (2.28)$$

The wave number, k equals $2\pi / \lambda$ and simply means that the field has a phase variation of 2π cycles per wavelength of travel. When multiplied by the distance, x, this product calculates how much the phase changes over the length of x or in other words, how much of the period is contained in the distance x. The portion of the period is the phase difference between object center and the object edge. Substituting (2.28) into (2.25) and solving for R yields the generalized far-field criterion:

$$R > \frac{\pi D^2}{4\Phi\lambda}$$ (2.29)

Kent states [7] that a range, R sufficiently large to result in a maximum 22.5 degree phase taper over the target is the standard used for acceptable cross-range phase variation in RCS range measurements. Substituting 22.5 degrees, ($\pi / 8$ radians) as a maximum allowable phase error into (2.29) yields far-field phase-restricted criterion of $\pi / 8$ radians, equation (2.30).

$$R > \frac{2D^2}{\lambda}$$ (2.30)

Not only is phase a consideration for far-field criterion, but also uniformity of incident field amplitude across the target aperture. Kouyoumjian and Peters specify that 1 dB of RCS measurement error can be expected if the incident field at the target has a phase variation less than or equal to $\pi / 8$ radians and an amplitude variation of 1 dB or less over the target aperture. It is worth noting that for range measurements, antenna beam width may be the most important factor in determining RCS measurement error due to range. Hendrick [10] examined configurations using point scatterers on long targets and concluded that narrow beamwidths created a larger amplitude taper across the target and resulted in a larger impact to RCS measurement error than the phase errors arising from

inadequate range. He postulates that since a wider beamwidth creates a more uniform

amplitude across the target, the range criterion may be lessened for long targets

consisting primarily of point scatterers. His range criterion is given in table 1 below

where the first column is the target length D divided by wavelength, corresponding to

the minimum acceptable range in the same row in the second column.

Table 2-2: Hendrick's [10] minimum range criterion for example target lengths

Target Size in Wavelengths: $\dfrac{D}{\lambda}$	Minimum Acceptable Range: R
3	$R \geq \dfrac{4D^2}{\lambda}$
10	$R \geq \dfrac{D^2}{2\lambda}$
50	$R \geq \dfrac{D^2}{4\lambda}$

2.12 Locally-Planar Surfaces and Constant Phase Area

The far-field phase criterion give by equation (2.30) can also be used to describe

whether a surface is sufficiently planar to be considered *locally planar*. For a region of

the target aperture, if the relative distance to the receiver does not vary by more than an

acceptable phase difference, i.e. $\pi/8$ radians , that region of the target is considered to

be a constant phase area and responsible for the specular flash. Substituting $\pi/8$ into

(2.28) equates to a range differential of $\lambda/16$. Therefore, a region of a target that varies

less than $\lambda/16$ in distance from the receiver is considered a constant phase area for a

cross-range variation of $\pi/8$ radians as illustrated in Figure 2-10. If the plate shown in

Figure 2-9, were curved such that $|R + x| \leq |R + \lambda/16|$ over the entire surface area, the

entire surface could be called locally planar. Therefore, if the constant phase area

encompasses the entire target at broadside incidence, the complete target could be

considered locally planar. In this scenario, the relative phase between scatterers across

the surface would be less than 22.5 degrees. To determine whether a surface is locally

planar in the case where only a portion of the target has a constant phase area as shown in

Figure 2-10, both the radius of curvature of the target and constant phase area must be

considered. If the radius of curvature of the surface in the neighborhood about a specular

point is several orders of magnitude larger than the radius of curvature at a point, for

example at the specular point on a sphere, this surface may be considered locally planar.

In the case of an irregular surface, using the $\pi/8$ cross-range phase variation tolerance,

as long as the distance from the irregularity to the receiver is not more than $\lambda/16$ the

surface is considered locally planar. Use of radius of curvature would be inappropriate

for the irregular surface since the radius of curvature, for example for some small

depression, might be smaller than the distance corresponding to the allowable cross-range

phase variation tolerance, i.e. less than $\lambda/16$ for $\pi/8$ cross-range phase variation

tolerance.
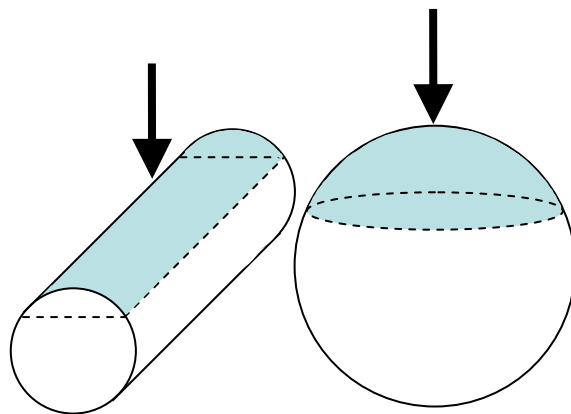
Figure 2-10: Constant phase areas responsible for specular flash [4]

2.13 Phasor addition to estimate lobing density

Dimensions of a target have a significant impact on the lobing structure of the RCS pattern. Consider the scattering geometry of a missile relative to an observation point as shown in Figure 2-1.
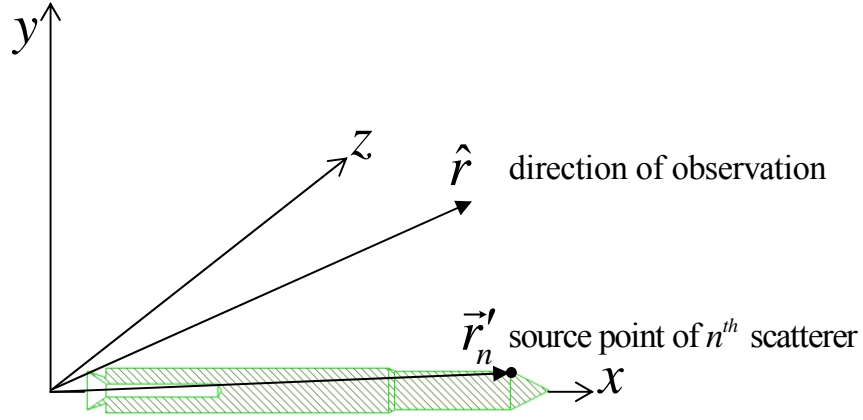
Figure 2-11: Scattering geometry

Recall from equation (2.27), the complex RCS of a collection of N individual scatterers can be represented as the square of the coherent sum of the individual scatterers:

$$\sigma(\theta,\phi) = \left| \sum_{n=1}^{N} \sqrt{\sigma_n} e^{j\Phi_n} \right|^2 , \qquad (2.31)$$

where Φ_n is the relative phase of that particular contribution due to its physical location in space[4]. The phase term can be written as the two-way phase difference between the observer and the nth scatterer:

$$\Phi_n = 2k(\hat{r} \cdot \vec{r}_n') \qquad (2.32)$$

$$\sigma = \left| \sum_{n=1}^{N} \sqrt{\sigma_n} e^{j2k(\hat{r} \cdot \vec{r}_n')} \right|^2 ,$$

$$\hat{r} \cdot \vec{r}_n' = \hat{r} \cdot \hat{x} x_n' + \hat{r} \cdot \hat{y} y_n' + \hat{r} \cdot \hat{z} z_n' = x_n' \sin\theta\cos\phi + y_n' \sin\theta\sin\phi + z_n' \cos\theta$$

where $\hat{r}$ is the direction of observation, $\vec{r}_n'$ is the source point vector from the origin to the location of the nth scatterer. For a simplified analysis of the 3-D missile, if z-invariance is assumed and the observation is normal to the x-y plane (i.e. $\theta = 90°$) then equation (2.32), the coherent sum of individual scatterers, can be written as:

$$\sigma = \left| \sum_{n=1}^{N} \sqrt{\sigma_n} e^{j\frac{4\pi}{\lambda}(x_n' \cos\phi + y_n' \sin\phi)} \right|^2 , \qquad (2.33)$$

where ϕ is the observation angle measured from the x axis, x_n' and y_n' are the Cartesian coordinates of the nth scatterer. A missile target typically has a significant difference in spatial extent in the x and y dimensions. By examining (2.33) RCS lobe widths can be explained. For small changes in observation angle $\Delta\phi$, about ϕ equals $= 0°$, $\cos(\Delta\phi) \approx 1$. However, $\sin(\Delta\phi) \approx \Delta\phi$. Then as ϕ varies by a small amount, the product $x_n' \cos\phi$ does not change very quickly. Therefore, fluctuations about $0°$ are determined by the $y_n' \sin\phi$ product. At a $90°$ observation angle the cosine term in (2.33) fluctuates more rapidly than the sine term therefore the $x_n' \cos\phi$ product determines the lobe widths. These results will explain the RCS lobing structure of the missile in Chapter 4. To illustrate this point, Figure 2-12 shows four point scatters representing the range of x_n' and y_n' and the relationship of the x_n' extent to y_n' extent. As the viewing angle approaches $90°$ the lobes become increasingly narrow. Therefore, fluctuations in terms of lobe widths can be characterized by examining the spatial distribution of scatterers.
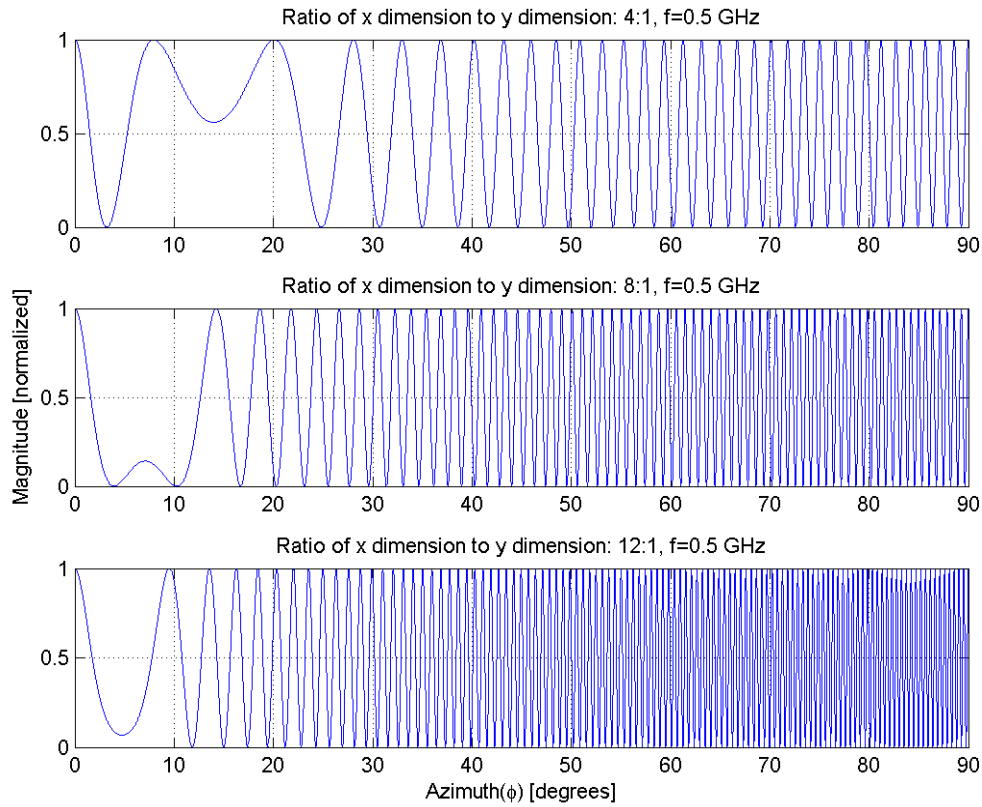
Figure 2-12: Lobing structure from four point scatterers of equal magnitude, where lobe widths are inversely proportional to the cross-range extent of the target.

2.14 Scattering Regimes

There are three regions defining types of scattering: Rayleigh, Mie (or resonance) and optical. Figure 2-13 shows the monostatic RCS of a sphere as a function of its circumference, these regions are defined by the target size in wavelengths [4, 15].

2.14.1 Optics Region

The optics region is characterized primarily by specular scattering from objects of a size much larger than a wavelength. The term *specular* is derived from the latin word, *speculum*, which means "mirror". A sphere is in the optics region when its electrical size (relative to wavelength) is $ka \geq 10\lambda$. In order for surface currents to wrap around the

sphere and return to the front where they can contribute to back-scattering, they must

travel a longer distance in wavelengths in the shadowed region (see inset,

Figure 2-13: Normalized monostatic RCS for a conducting sphere as a function of its
circumference over the three scattering regimes [4, 15]

). As the surface currents traverse the longer distance in the shadowed region, more

energy scatters to the forward region and thus less current flows around to the front face

of the sphere. The result is that the major contributing scattering mechanism in the optics

region is from energy reflected back to a receiver from the specular point on the sphere

rather than from surface waves.
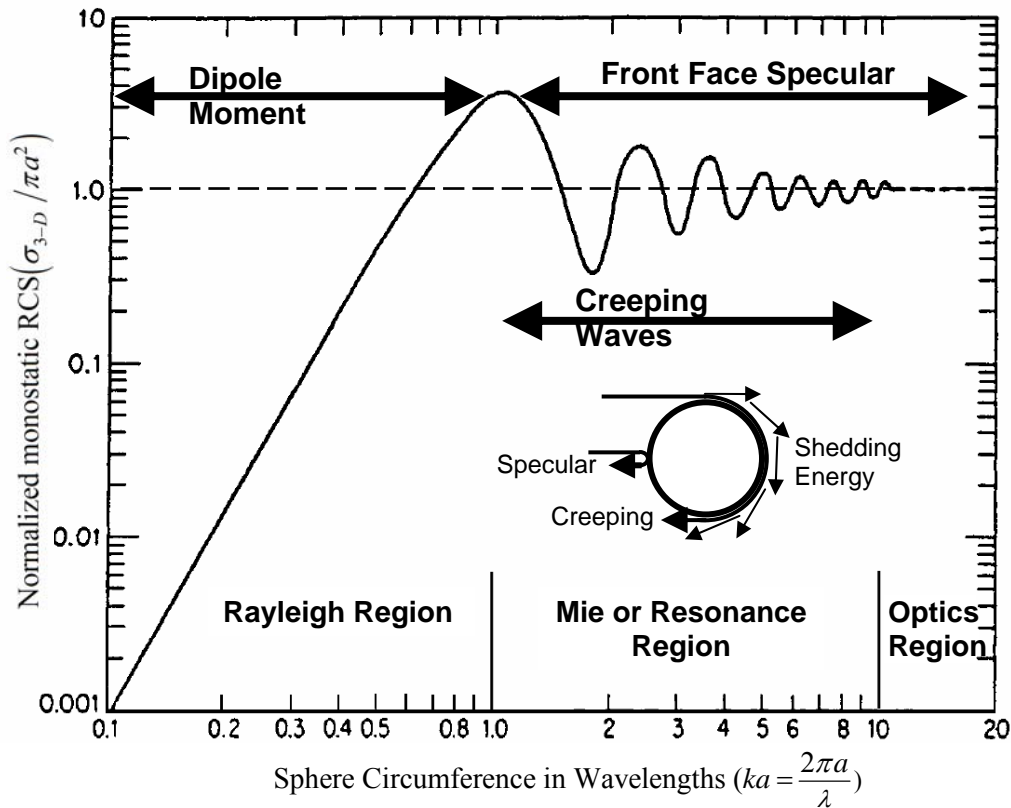
Figure 2-13: Normalized monostatic RCS for a conducting sphere as a function of its
circumference over the three scattering regimes [4, 15]

The specular point on a sphere is that point which aims a surface normal, $\hat{n}$, directly back

at the receiver. Surface currents which shed energy in shadowed regions are referred to

as creeping waves. Specular scattering for non-spherical objects will also dominate over

creeping waves in the optics region. Two other scattering mechanisms attributed to

objects in both the Mie and Optics regions are diffraction and multiple bounce.

Diffraction is electromagnetic scattering which occurs when a surface current encounters

a sudden discontinuity on the surface. Multiple bounce refers to multiple specular

scattering or multiple diffraction scattering as depicted in Figure 2-14. For target

modeling, features on the order of a wavelength should be included in the model.
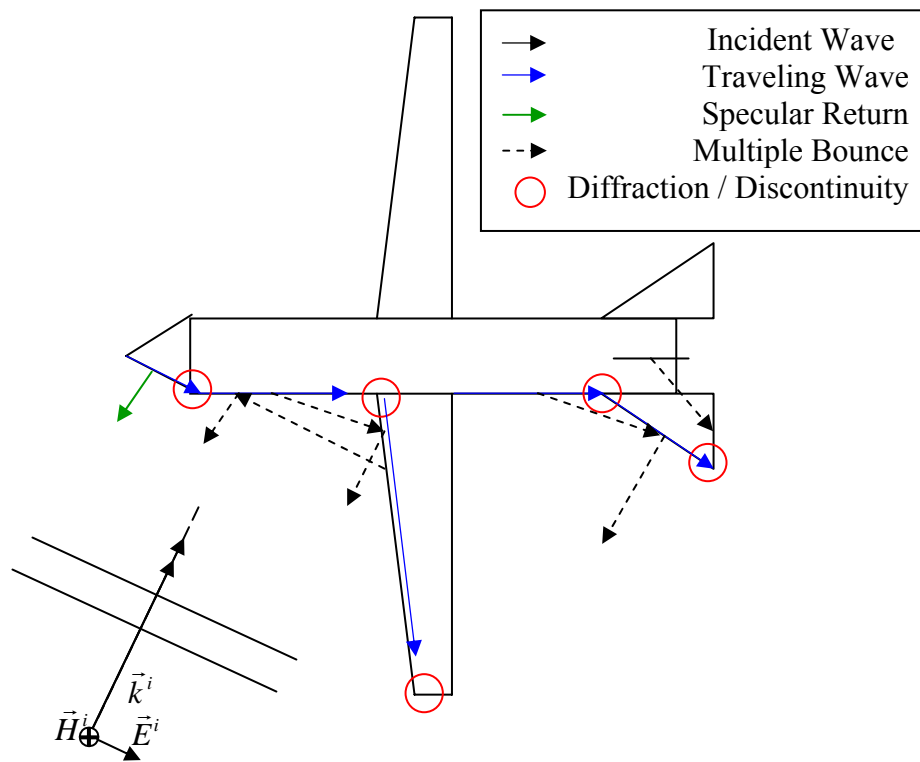
Figure 2-14: Scattering in the optics region due to an incident plane wave

2.14.2 Mie/Resonant Region

Objects on the order of a wavelength $0.1\lambda < ka < 10\lambda$, are Mie scatterers where

mechanisms such as traveling and creeping waves come into play. Surface currents that

gain energy in illuminated regions are referred to as traveling waves. Traveling waves

occur when a component of the electric field lies in the plane of incidence inducing a current that is reinforced by the incident field. The Mie region is referred to as the resonant region due to the occurrence of constructive and destructive interference of creeping waves with the specular reflection from the constant phase area of the front of the sphere. As in the optics region, features on the order of a wavelength should be included in the model.

2.14.3 Rayleigh Region

For objects smaller than a wavelength such as hydrometeors, there is relatively no phase variation over the surface of the body. The constant phase of the field relative to the object causes a polarization of charges, i.e. a dipole moment, to be established across the object. It can be shown that electrostatic analysis applies to this situation and the RCS is proportional to the fourth power of frequency [4]. All objects in this thesis are in the optical and Mie scattering regions. Shape and size are important for objects in this scattering regime.

2.15 CAD Model Requirements

CEM codes require a computer model representation of the target. FISC, CARLOS, and SAF accept CAD models composed of triangular facets. Inevitably, even the best computer models will be different from the physical targets for one of two reasons: either the CAD model is more precise than the physical model, or the CAD model is an approximation of the physical model. For example, a flat plate with zero thickness can be described perfectly by a triangular patch model but the real physical plate will have a finite thickness. On the other hand, a sphere described by flat triangular

facets can only approximate the doubly-curved surface of the physical model.

Differences between the CAD and physical model are error sources but may be

insignificant depending on the frequency of interest. For example, section 2.12 discusses

criteria for curved or irregular surfaces that may be considered planar depending on

frequency. For good convergence and accuracy, triangular facets should be as close to

equilateral as possible. FISC recommends that the ratio of longest to shortest facet be

less than 100. FISC and SAF analyze the ratios of longest to shortest edge lengths of

each facet contained in the facet file and record the largest, smallest, and average ratio to

an output page as shown in Figure 2-15.

```
Aspect ratio for this facet model:
        largest  aspect ratio         = 1.0000
        smallest aspect ratio         = 0.5207
        average  aspect ratio         = 0.9489
```

Figure 2-15: FISC Output file analysis of facet sidelength ratios

This equilateral triangular facet constraint is at odds with accurate modeling of certain

target features such as sharp tips which can result in long, narrow facets or facets that are

significantly smaller than the average facet size. Such facets can result in solution

inaccuracy (non-converged results) and computational instability. Target surfaces can be

meshed carefully to capture important scattering structures but this requires an

understanding of how the small details affect electromagnetic theory. Oftentimes, the

decision whether to model a feature boils down to the size of the feature with respect to

the transmitted wavelength. For an aircraft geometry, this may be manifested by

decisions on whether to model extruded features such as points/tips based on relationship

to wavelength or cavities, depressions and gaps based on cutoff frequencies.

Another requirement, when using CAD geometry for FISC, CARLOS and SAF is that the geometry must be 'well connected'. This means that all facet edges must meet at a vertex and no vertex may terminate in the center of another edge. To match with FISC terminology, hereafter vertices are called nodes. Nodes which do not meet the criteria stated above are called hanging nodes. Figure 2-16 shows facet connectivities disallowed by FISC [13].
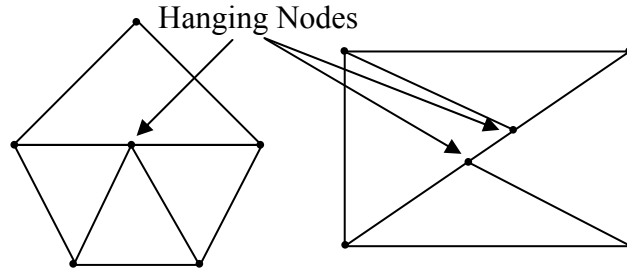
Figure 2-16: Facet connectivities disallowed in FISC[13], SAF, and CARLOS

2.15.1 Target Surface Discretization

Target curvature can only be approximated when using triangular facets. The number of facets required to cover the total surface area is the object's total surface area, A_s, divided by the area of an equilateral triangular facet, A_f:

$$\text{Facets} \approx \frac{A_s}{A_f} = \frac{A_s}{\frac{1}{2}bh} = \frac{A_s}{\frac{1}{2}b^2 \sin(60°)} = \frac{A_s}{\frac{1}{2}b^2 \frac{\sqrt{3}}{2}} = \frac{4A_s}{b^2\sqrt{3}} \, . \tag{2.34}$$

Each triangle edge represents an unknown surface current. So a key question is always, "How many edges or unknowns comprise a target?" The geometry should be a good representation of the target. Computational time and memory are both proportional to the number of unknowns. Each edge current is mathematically represented by basis functions that model the expected physical behavior of the surface current. An

assumption is made that the surface current has constant phase and over a facet edge.

Phase varies with distance traveled by the wave, as defined by the wave number, k. To

allow for this phase variation, FISC recommends that the surface should be discretized

with segments having edge lengths no longer than $\lambda/5$ where $\lambda/10$ is a generally

accepted minimum for good solution convergence. Incorporating discretization into

(2.34) yields:

$$\text{Facets} \approx \frac{4A_s}{\left(\dfrac{\lambda}{d}\right)^2 \sqrt{3}} = \frac{4d^2 f^2 A_s}{c^2 \sqrt{3}}, \tag{2.35}$$

where d is the discretization, f is the operating frequency and c is the speed of light.

(a)

8 Vertices
12 Facets
18 Edges

(b)

14 Vertices
24 Facets
36 Edges

(c)

26 Vertices
48 Facets
72 Edges

(d)

50 Vertices
96 Facets
144 Edges

(e)

96 Vertices
192 Facets
288 Edges
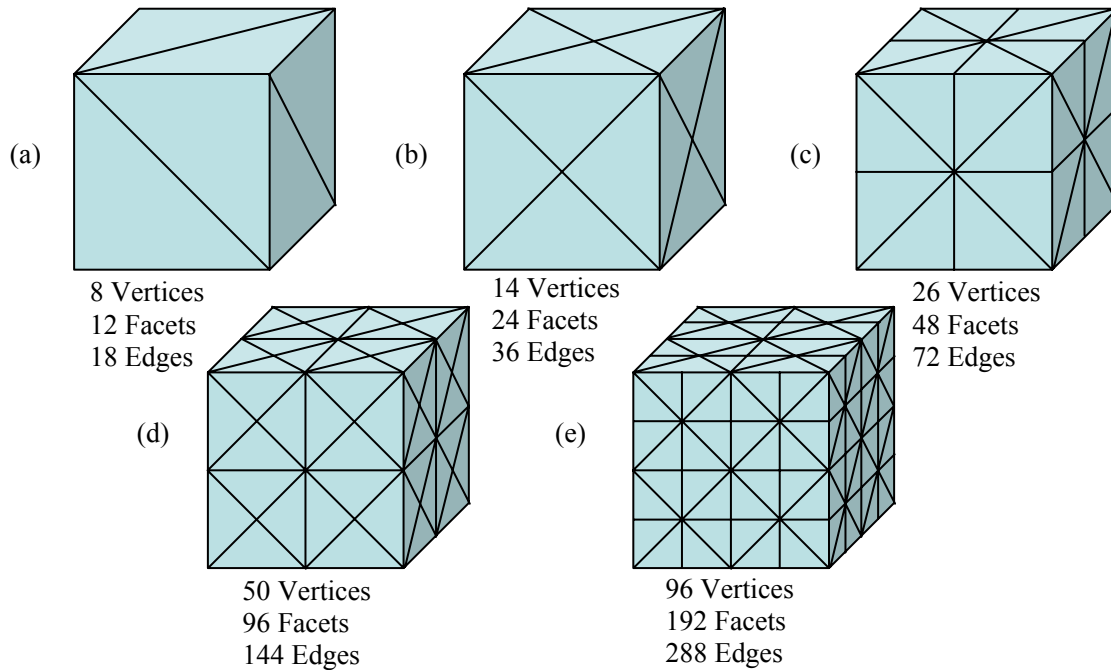
Figure 2-17: 6-sided cube with increasing levels of discretization

It can be shown that as the number of nodes increases for three-dimensional models, the

relationship of the number of nodes to the number of facets to the number of edges is

1:2:3. To demonstrate this relationship, consider the simple geometry of a closed cube shown in Figure 2-17. As shown in the figure, several levels of discretization can describe the same cube. Figure 2-17(a) describes the cube with the fewest number of triangular facets. The cubes in Figure 2-17(b) – (e) show increasing levels of discretization. A general recursive formula for this iterative increase in facets is given by

$$
\begin{bmatrix} \dfrac{N_{n(i)}}{N_{n(i)}} \\[2mm] \dfrac{N_{F(i)}}{N_{n(i)}} \\[2mm] \dfrac{N_{E(i)}}{N_{n(i)}} \end{bmatrix} = \begin{bmatrix} \left[\dfrac{2(N_{n(i\text{-}1)}-1)}{2(N_{n(i\text{-}1)}-1)}\right] \\[2mm] \dfrac{2N_{F(i\text{-}1)}}{2(N_{n(i\text{-}1)}-1)} \\[2mm] \dfrac{2N_{E(i)}}{2(N_{n(i\text{-}1)}-1)} \end{bmatrix} \xrightarrow[\ \to\ ]{i \to large} \begin{bmatrix} 1 \\ 2 \\ 3 \end{bmatrix},
\tag{2.36}
$$

where $N_{n(i)}$, $N_{F(i)}$ and $N_{E(i)}$ are the number of nodes, triangular facets and edges for the

i^{th} level of discretization; $N_{n(0)} = 8$, $N_{F(0)} = 12$, and $N_{E(0)} = 18$ as shown in Figure 2-17(a);

and i is the level of discretization (Figure 2-17(b),(c),(d), and (e) represent

$i = 1, 2, 3$ and 4, respectively). As the discretization level increases, the ratio quickly

approaches the 1:2:3 relationship as shown in

Table 2-3. Two nodes are required for each edge, each edge is shared by two facets and each facet has three edges. Therefore, the number of edges for a 3-D surface is approximately equal to one and a half (1.5) times the number of triangular facets:

$$
\text{Edges} \approx \frac{3}{2}\text{Facets} = \frac{6A_s}{\sqrt{3}}\left(\frac{d}{\lambda}\right)^2.
\tag{2.37}
$$

For example, using equation (2.37) for a cube of side length $l = \lambda/2$, with discretization (also called mesh density) of $d = \lambda/10$, yields about 347 nodes where a ceiling function is used because not all triangles will be equilateral and the entire surface of a closed object will be fully covered by facets. Figure 2-18 illustrates the increase in the number

of edges as a function of frequency and discretization level for a 1-meter square cube. A

less precise method is to estimate the number of edges is from the number of nodes.

Using equation (2.38) for the hypothetical cube with $\lambda/10$ discretization and side length

of $\lambda/2$, 150 nodes would be needed. Once again, the ceiling function is needed since

the equation doesn't account for shared nodes which causes them to be doubly counted.

Referring to Table 2-3, this node estimate falls between i=4 and i=5, so the rough

estimate is 300 to 600 edges for this problem. As the number of nodes increases, the

number of edges approaches three times the number of nodes.

$$N_n = 6\left(\frac{10l}{\lambda}\right)^2.$$ (2.38)

Table 2-3: Node:Facet:Edge counts for a 6-sided cube as discretization increases

i	# Vertices	# Facets	# Edges	Relationship: $\frac{1}{N_n}\left(N_n : N_F : N_E\right)$
0	8	12	18	1.0000:1.5000:2.2500
1	14	24	36	1.0000:1.7143:2.5714
2	26	48	72	1.0000:1.8462:2.7692
3	50	96	144	1.0000:1.9200:2.8800
4	98	192	288	1.0000:1.9592:2.9388
5	194	384	576	1.0000:1.9794:2.9691
6	386	768	1152	1.0000:1.9896:2.9845
7	770	1536	2304	1.0000:1.9948:2.9922
8	1538	3072	4608	1.0000:1.9974:2.9961
9	3074	6144	9216	1.0000:1.9987:2.9980
10	6146	12288	18432	1.0000:1.9993:2.9990
11	12290	24576	36864	1.0000:1.9997:2.9995
12	24578	49152	73728	1.0000:1.9998:2.9998
13	49154	98304	147456	1.0000:1.9999:2.9999
14	98306	196608	294912	1.0000:2.0000:2.9999
15	196610	393216	589824	1.0000:2.0000:3.0000
16	393218	786432	1179648	1.0000:2.0000:3.0000
17	786434	1572864	2359296	1.0000:2.0000:3.0000
18	1572866	3145728	4718592	1.0000:2.0000:3.0000
19	3145730	6291456	9437184	1.0000:2.0000:3.0000
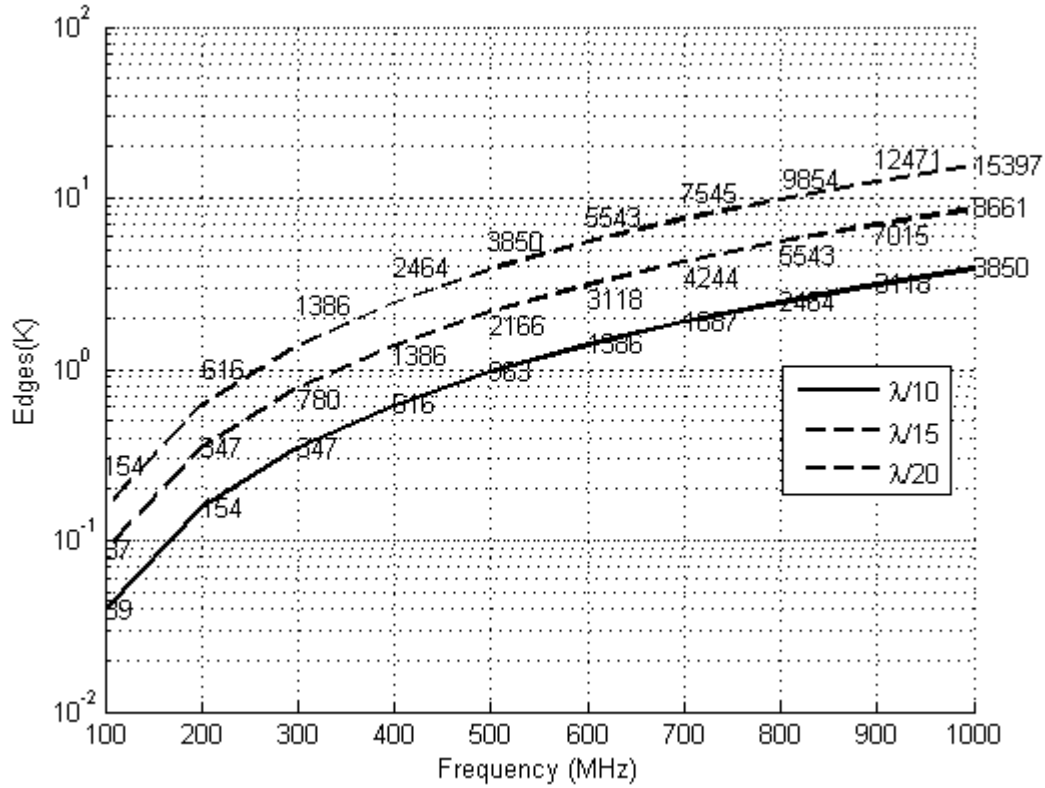
Figure 2-18: Number of edges versus frequency for a cube with side length of 1 meter.

2.15.2 Closed CAD models

CFIE solutions were selected for the study, therefore, closed CAD geometries were necessary. In order for the geometry to be 'closed', all facet edges must meet at a vertex which means that no edge may terminate in the center of another edge. Geometries that are open will not meet the 1:2:3 Node:Facet:Edge relationship. FISC/SAF perform a check for this relationship when MFIE or CFIE are specified. If it is found that the number of edges are not equal to 1.5 (one and a half) times the number of facets, the EFIE formulation will be used.

2.15.3 CAD Model Summary

In summary, for good convergence and accuracy, target geometries using triangular facets should meet the following requirements:

1. Well-connected, no hanging nodes

2. For closed surfaces, the edge count must be equal to 1.5 (one and a half times) times the number of facets

3. The ratio of longest to shortest edge should be less than 100

4. The maximum edge length should no longer than $\lambda/10$ for two reasons:

   a. The discretization should be fine enough to be a good representation of the target geometry

   b. It is generally assumed that surface current has constant phase and magnitude over a facet edge

2.15.4 FISC/SAF/CARLOS Discretization Refinement

FISC/SAF have the capability to refine a mesh of triangular facets, CARLOS does not offer this feature. This is advantageous for targets which can be described well by straight sides but is no help for targets with curved surfaces. As Figure 2-1 illustrates, FISC & SAF refine the mesh by splitting each side greater than the specified fraction of a wavelength in half. This effectively places a smaller inverted triangular facet inside the original facet. As can be seen from the previous section, each split (equivalent to halving λ in equation (2.37)) results in a four-fold increase in the number of facets. Some mesh refinement can be done without a four-fold increase by changing the allowable max edge length by a small amount. In this case, FISC/SAF will find edges larger than the maximum specified and refine those facets and the neighboring facets (to prevent

hanging nodes) to produce a small increase in the total number of facets. CARLOS offers the feature to refine a body of revolution (BOR) target with its BOR_SEG command, see Appendix B for an example CARLOS BOR input page.
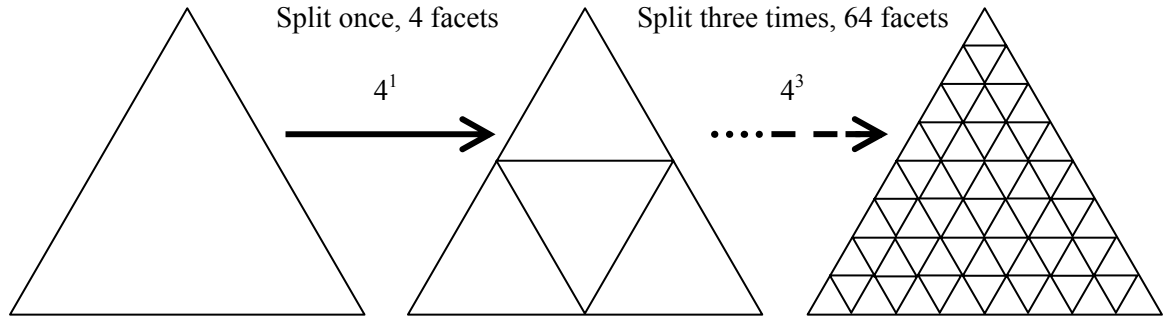
Figure 2-19: FISC/SAF mesh refinement

2.16 Method of Moments

The method of moments (MoM) is a numerical technique to find solutions to linear integro-differential equations. The name comes from the process of taking moments by multiplying a function by weighting/testing functions and integrating. FISC, SAF, and CARLOS use MoM to solve for the induced currents (current density) on the surface of an object by converting a continuous integral equation into a discrete matrix-vector product. The linear operator equation is a general inhomogeneous linear equation of the form [2]:

$$\mathcal{L}\{u(x)\} = f(x), \qquad\qquad (2.39)$$

where $\mathcal{L}$ is a linear operator, $u(x)$ is the unknown function, and $f(x)$ is the known forcing function. In our application, $\mathcal{L}$ is either an integral or integro-differential linear operator, $u(x)$ is electric current density (J) or magnetic current density (M) and $f(x)$

2-37

is the incident electric field intensity, E^i or magnetic field intensity, H^i. The unknown

function is expanded in a series, namely:

$$u(x) = \sum_{n=1}^{N} a_n e_n(x) \Rightarrow \mathcal{L}\left\{\sum_{n=1}^{N} a_n e_n(x)\right\} = f(x), \tag{2.40}$$

where a_n is the unknown expansion coefficient, $e_n(x)$ is a known basis/expansion

function, and N is the number of edges in the target model. Since $\mathcal{L}$ is a linear operator

(2.40) can be rewritten as

$$\sum_{n=1}^{N} a_n \mathcal{L}\{e_n(x)\} = f(x), \tag{2.41}$$

if interchange is allowed. This expansion step represents the discretization of the

continuous integral equation to solve for unknown surface currents. The original task of

finding the unknown function is now modified to finding N unknown constants. Basis

functions are chosen to model the physical behavior of the unknown function. For an

exact solution, the summation in (2.40) has an infinite number of terms forming complete

basis function sets. For an approximate solution, N is finite. What did we gain?

$\mathcal{L}\{e_n(x)\}$ can be calculated but at this point we have 1 equation and N unknowns. To

generate N equations for the N unknowns the testing function is applied N times over an

inner product, $< x, y >$ to create an $N \times N$ matrix. The inner product with the testing

function is in the form of an operator:

$$<t_m, \{\bullet\} >\big|_{m=1,\dots,N} \Rightarrow \int_a^b t_m(x)\{\bullet\} dx, \tag{2.42}$$

where $t_m(x)$ is the mth testing function in the range of $\mathcal{L}$ and $\{\bullet\}$ is the function to be

tested. The integration limits in (2.42) are defined by the end-points of the edges of the

triangular facets of the computer model. These limits represent the integral equation

discretization due to the fidelity of the target geometry. Applying the testing operator to

(2.41) yields:

$$\int_a^b t_m(x)\left\{\sum_{n=1}^N a_n \mathcal{L}\{e_n(x)\}\right\}dx = \int_a^b t_m(x)\{f(x)\}dx \tag{2.43}$$

$$\Rightarrow \sum_{n=1}^N a_n \int_a^b t_m(x)\mathcal{L}\{e_n(x)\}dx = \int_a^b t_m(x)\{f(x)\}dx \quad ... \ m=1,...,N$$

Let

$$Z_{mn} = \int_a^b t_m(x)\mathcal{L}\{e_n(x)\}dx \tag{2.44}$$

$$b_m = \int_a^b t_m(x)\{f(x)\}dx$$

where Z_{mn} is an $N \times N$ matrix representing the impedance between individual elements of

the target geometry, b_m is an N length column vector of known field intensities. In

scattering problems Z_{mn} is geometry-dependent and remains the same no matter what the

incident angle of the electromagnetic wave or observation angle of the receiver.

Substituting (2.44) into (2.43) results in a simplified equation

$$\sum_{n=1}^N Z_{mn}a_n = b_m, \tag{2.45}$$

which has the form:

$$\begin{bmatrix} Z_{11} & \cdot & \cdot & \cdot & Z_{1N} \\ \cdot & \cdot & & & \cdot \\ \cdot & & \cdot & & \cdot \\ \cdot & & & \cdot & \cdot \\ Z_{N1} & \cdot & \cdot & \cdot & Z_{NN} \end{bmatrix} \begin{bmatrix} a_1 \\ \cdot \\ \cdot \\ \cdot \\ a_N \end{bmatrix} = \begin{bmatrix} b_1 \\ \cdot \\ \cdot \\ \cdot \\ b_N \end{bmatrix}. \tag{2.46}$$

<div align="center">known   unknown   known</div>

Galerkin's method uses the the testing function as the basis function, that is:

$$t_m(x) = e_m(x). \tag{2.47}$$

The last step in the method of moments procedure is to fill the matrix and solve for the unknown coefficients:

$$a_n = Z_{mn}^{-1} b_m .$$ (2.48)

In summary, the method of moments procedure discretizes a continuous integro-differential matrix vector product in the following three-step procedure:

1. Expansion of the unknown function

2. Application of testing functions of an inner product (testing operator)

3. Filling and solving the matrix

2.17 Memory Requirement Estimation

As mentioned previously, each edge represents an unknown surface current. The number of edges equates to the number of unknowns, N. As will be shown in Section 2.16, N determines the size of the impedance matrix. For MoM codes such as CARLOS-3D that store the matrix in memory (for certain geometry types), the number of edges can be used to estimate the memory requirement. If the example cube discussed in Section 2.15.1 contained 600 edges the resulting $N \times N$ matrix would be contain 360,000 elements. Assuming each number is stored with single precision accuracy, the memory required for storage using (2.49) would be approximately 2.75MB.

$$\left(N^2 \ elements \right)\left(8 \ bytes \right)\left(\frac{1 \ MB}{1024^2 \ bytes} \right) = \text{memory required } (MB) .$$ (2.49)

2.18 Solution Time

Estimating the processing time required by an iterative solver that does not employ FMM or MLFMA must be done empirically since solution time is dependent upon how

quickly the solution method such as conjugate gradient (CG) converges on a solution. In

its simplest form, the problem being solved is

$$[\mathbf{V}] = [\mathbf{Z}][\mathbf{I}],\tag{2.50}$$

where $\mathbf{V}$ is the known incident field, $\mathbf{I}$ is the unknown surface current, and $\mathbf{Z}$ is a

known matrix describing the impedances between each element across the target surface.

The iterative solution method used in FISC/SAF and available in CARLOS guesses the

unknown surface currents, $\mathbf{I}$, multiplies $\mathbf{I}$ by the known impedance matrix $\mathbf{Z}$ and

compares to the known incident field, $\mathbf{V}$. Through residual error reduction, the error is

compared to an acceptable error bound and the next guess is updated using the CG

method. Each iteration of this process requires N^2 multiplications. The time required to

converge on a solution within error bounds will vary based on geometry, viewing aspect,

and applied materials. The solution time required is dependent on the number of

operation performed and the speed of the central processing unit (CPU) [14]:

$$\left(M\ iterations\right)\left(N^2\ operations\right)\left(S\right) = CPU\ time,\tag{2.51}$$

where S is the arithmetic processor speed in operations per second. This calculation does

not include the time required to read in the geometry, perform checks, calculate plane

wave expressions, fill the matrix or create output files. Deriving expressions for these

operations is non-trivial and beyond the scope of this thesis. The time required is

geometry-dependent and related to the condition number of the impedance matrix. FMM

accelerates the matrix vector multiplications by reducing the required N^2 operations to

$O\left(N^{1.5}\right)$ where the order is the number of iterations. MLFMA further accelerates the

process to reduce complexity to $O\left(N\log N\right)$. Common to CARLOS, FISC (2.51)and

SAF is the option to perform full-matrix inversion using Gaussian elimination or Lower

Upper Decomposition (LUD). Matrix inversion requires N^3 operations. Recall that the impedance matrix is geometry-dependent. Once inverted it can be used to solve for any incident or observed angle. To solve for each incident angle requires an N^2 operation matrix vector product of the inverted impedance matrix with the incident field. Therefore the processing time required for matrix inversion and solution is:

$$\left(N^3 \; operations\right)\left(S\right) + \left(P_{\theta,\phi}\right)\left(N^2 \; operations\right)\left(S\right) = \text{processing time}, \qquad (2.52)$$

where $P_{\theta,\phi}$ is the number of incident angles. For a complete discussion of MLFMA refer to [16].

2.19 *Physical Optics Approximation for a Material-Coated PEC Flat Plate*

Section 4.6 examines FISC's performance using impedance boundary conditions (IBC) by comparing predicted results using IBCs against measured data for an MRAM-coated PEC flat plate. To provide a third comparison, a PO expression for RCS is developed here for perpendicular and parallel polarization. PO is the foundation for asymptotic codes such as Xpatch®. This analysis will show how PO approximation used by asymptotic codes can be expected to compare to an MoM code using IBCs.

2.19.1 *Physical Optics Approximation of the RCS of a Material-Coated PEC Finite Plate for Parallel Polarization*

Consider a TEM wave incident upon a finite-width, material-coated PEC rectangular plate of arbitrary length a and width b depicted in Figure 2-1. The field point position vector $\vec{r}$ and source point position vector, $\vec{r}'$ are given in equation (2.53). In this example, $\hat{n} = \hat{z}$, and the $y - z$ plane is the plane of incidence since it contains both $\hat{k}^i$ and $\hat{n}$.
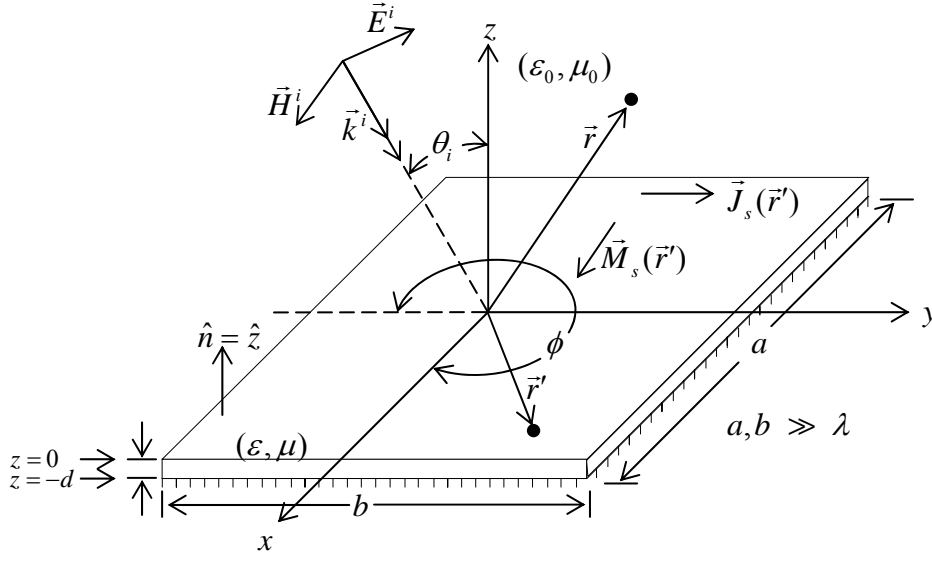
Figure 2-20: Material-coated PEC finite plate, parallel polarization

$$\vec{r} = \hat{x}x + \hat{y}y + \hat{z}z \tag{2.53}$$

$$\vec{r}' = \hat{x}x' + \hat{y}y'$$

$$\hat{r} \cdot \vec{r}' = \hat{r} \cdot \hat{x}x' + \hat{r} \cdot \hat{y}y' = x'\sin\theta\cos\phi + y'\sin\theta\sin\phi$$

The incident wave vector, $\vec{k}^i$ has magnitude k_0 since it is traveling in free space is

defined in (2.54):

$$\vec{k}^i = \hat{y}(\hat{y} \cdot \vec{k}^i) + \hat{z}(\hat{z} \cdot \vec{k}^i) = k_0(\hat{y}\sin\theta_i - \hat{z}\cos\theta_i) = k_0\hat{k}^i \tag{2.54}$$

$$\text{since } \hat{k}^i = \frac{\vec{k}^i}{|\vec{k}^i|};$$

,

$$\hat{k}^i = \hat{y}\sin\theta_i - \hat{z}\cos\theta_i$$

where $\hat{k}^i$ is the unit vector pointing in the direction of the incident wave. In this

example, $\hat{n} = \hat{z}$, and the $y - z$ plane is the plane of incidence since it contains both $\hat{k}^i$

and $\hat{n}$. The incident electric field is

$$\vec{E}^i = \vec{E}_0^i e^{-j\vec{k}^i \cdot \vec{r}} = E_0^i \hat{E}_0^i e^{-j\vec{k}^i \cdot \vec{r}} = E_0^i(\hat{y}\cos\theta_i + \hat{z}\sin\theta_i)e^{-jk_0(y\sin\theta_i - z\cos\theta_i)}, \tag{2.55}$$

where

$$\vec{k}^i \cdot \vec{r} = k_0 \hat{k}^i \cdot (\hat{x}x + \hat{y}y + \hat{z}z) = k_0 (\hat{y}\sin\theta_i - \hat{z}\cos\theta_i) \cdot (\hat{x}x + \hat{y}y + \hat{z}z) \tag{2.56}$$
$$= k_0 (y\sin\theta_i - z\cos\theta_i)$$

The electric and magnetic fields of a *TEM* wave are related by the expression:

$$\vec{H} = \frac{\hat{k} \times \vec{E}}{\eta} \Rightarrow \vec{H}^i = \frac{\hat{k}^i \times \vec{E}_i}{\eta_0} = \hat{x}\frac{\vec{E}_0}{\eta_0} e^{-jk_0(y\sin\theta_i - z\cos\theta_i)}, \tag{2.57}$$

where η_0 is the intrinsic impedance of the medium containing the incident wave, in this case, free space, and is defined as

$$\eta = \sqrt{\frac{\mu}{\varepsilon}} \Rightarrow \eta_0 = \sqrt{\frac{\mu_0}{\varepsilon_0}}. \tag{2.58}$$

Physical optics current approximations are given by (2.59) and are polarization-dependent for material-coated surfaces due to polarization-specific wave impedances [1].

$$\vec{J}_s(\vec{r}') \cong (1-R)\hat{n}' \times \vec{H}^i(\vec{r}')\Big|_{\substack{z'=0 \\ \hat{n}'=\hat{z}'=\hat{z}}} = \hat{y}\frac{E_0^i}{\eta_0}(1-R)e^{-jk_0 y'\sin\theta_i} \tag{2.59}$$
$$\vec{M}_s(\vec{r}') \cong -(1+R)\hat{n}' \times \vec{E}^i(\vec{r}')\Big|_{\substack{z'=0 \\ \hat{n}'=\hat{z}'=\hat{z}}} = \hat{x}E_0^i(1+R)\cos\theta_i e^{-jk_0 y'\sin\theta_i}$$

Where R (2.60) is the interfacial reflection coefficient at i^{th} interface, in this case $i=1$. Z_n is the wave impedance of the medium (2.61). Refer to [3] for development of Z_n and R_n,

$$R_n = \frac{Z_n - Z_{n-1}}{Z_n + Z_{n-1}}. \tag{2.60}$$

The wave impedance of the medium is polarization-dependent:

$$Z_n = \begin{cases} \dfrac{\eta_n k_{nz}}{k_n} & \dots \quad \| \text{ polarization} \\[2ex] \dfrac{\eta_n k_n}{k_{nz}} & \dots \quad \perp \text{ polarization} \end{cases} \tag{2.61}$$

2-44

Note that for a perfectly electrically conducting (PEC) surface, the reflection coefficient, R, is -1, thereby reducing the surface current density given in (2.59) to its familiar form (2.62).

$$\vec{J}_{s\_PO} = \begin{cases} 2\hat{n}' \times \vec{H}^i(\vec{r}') & \text{... illuminated region} \\ 0 & \text{... shadow region} \end{cases} \tag{2.62}$$

The magnetic vector potential, $\vec{A}$ is used to obtain an expression for the field scattered by the target (2.63):

$$\vec{A} = \frac{\mu}{4\pi} \int_S \vec{J}_s(\vec{r}') \frac{e^{-jk\hat{r}\cdot\vec{r}'}}{r} ds', \tag{2.63}$$

$$E_A^s = -j\omega\mu\vec{A}$$

where the scattered electric field due to $\vec{A}$ contains both θ and ϕ components. A more convenient notation makes use of radiation integral $\vec{N}$ (2.64) [1]. The radiation integral for calculating the far-zone scattered electric field due to the magnetic vector potential for the material-covered rectangular plate is given by:

$$\vec{N} = \int_S \vec{J}_s(\vec{r}')e^{jk\hat{r}\cdot\vec{r}'}ds' = \int_{-b/2}^{b/2}\int_{-a/2}^{a/2} \hat{y}\frac{E_0^i}{\eta_0}(1-R)e^{-jk_0 y'\sin\theta_i}e^{jk_0(x'\sin\theta\cos\phi+y'\sin\theta\sin\phi)}dx'dy' \tag{2.64}$$

$$\vec{N} = \hat{y}\frac{E_0^i}{\eta_0}(1-R)\int_{-a/2}^{a/2}e^{jk_0 x'\sin\theta\cos\phi}dx'\int_{-b/2}^{b/2}e^{jk_0 y'(\sin\theta\sin\phi-\sin\theta_i)}dy'.$$

Evaluating the integral yields (2.66). Note that the integrals in (2.64) evaluate to sinc functions (2.65).

$$\int_{-a/2}^{a/2} e^{jk_0 x' \sin\theta\cos\phi} dx' = a\operatorname{sinc}X \quad **; \text{ where } X = \frac{a}{2}k_0 \sin\theta\cos\phi; \tag{2.65}$$

$$\int_{-b/2}^{b/2} e^{jk_0 y'(\sin\theta\sin\phi - \sin\theta_i)} dy' = b\operatorname{sinc}Y; \text{ where } Y = \frac{b}{2}k_0 (\sin\theta\sin\phi - \sin\theta_i) \quad .$$

** see appendix for details of this integration

The final expression for the radiation integral is

$$\vec{N} = \hat{y}ab\frac{E_0^i}{\eta_0}(1-R)\operatorname{sinc}X\operatorname{sinc}Y . \tag{2.66}$$

Finally, the scattered electric field due to the magnetic vector potential $\vec{A}$ can be calculated:

$$\vec{N}_t = \left[\hat{\theta}(\hat{\theta}\cdot\hat{y}) + \hat{\phi}(\hat{\phi}\cdot\hat{y})\right]ab\frac{E_0^i}{\eta_0}(1-R)\operatorname{sinc}X\operatorname{sinc}Y \tag{2.67}$$

$$(\hat{\theta}\cdot\hat{y}) = \cos\theta\sin\phi; \qquad (\hat{\phi}\cdot\hat{y}) = \cos\phi$$

$$\vec{E}_A^s \cong -\frac{jk\eta}{4\pi}\frac{e^{-jkr}}{r}\vec{N}_t = \frac{jk_0\eta_0}{4\pi}\frac{e^{-jkr}}{r}\vec{N}_t$$

$$\vec{E}_A^s = -\frac{jk_0}{4\pi}abE_0^i(1-R)\frac{e^{-jk_0 r}}{r}\operatorname{sinc}X\operatorname{sinc}Y(\hat{\theta}\cos\theta\sin\phi + \hat{\phi}\cos\phi)$$

Similarly, the radiation integral for calculating the scattered magnetic field due to the electric vector potential $\vec{F}$ for the material covered rectangular plate is

$$\vec{L} = \int_S \vec{M}_s(\vec{r}')e^{jk\hat{r}\cdot\vec{r}'}ds' = \int_{-b/2}^{b/2}\int_{-a/2}^{a/2}\hat{x}E_0^i(1+R)\cos\theta_i e^{-jk_0 y'\sin\theta_i}e^{jk_0(x'\sin\theta\cos\phi + y'\sin\theta\sin\phi)}dx'dy' \tag{2.68}$$

$$\vec{L} = \hat{x}E_0^i(1+R)\cos\theta_i\int_{-a/2}^{a/2}e^{jk_0 x'\sin\theta\cos\phi}dx'\int_{-b/2}^{b/2}e^{jk_0 y'(\sin\theta\sin\phi - \sin\theta_i)}dy' \quad .$$

$$\vec{L} = \hat{x}abE_0^i(1+R)\cos\theta_i\operatorname{sinc}X\operatorname{sinc}Y$$

Using the radiation zone approximation, one obtains the scattered magnetic field due to the electric vector potential $\vec{F}$:

$$\vec{L}_t = \hat{\theta}L_\theta + \hat{\phi}L_\phi = \left[\hat{\theta}(\hat{\theta}\cdot\hat{x}) + \hat{\phi}(\hat{\phi}\cdot\hat{x})\right]abE_0^i(1+R)\cos\theta_i \text{sinc}X\text{sinc}Y \tag{2.69}$$

$$(\hat{\theta}\cdot\hat{x}) = \cos\theta\cos\phi; \qquad (\hat{\phi}\cdot\hat{x}) = -\sin\phi$$

$$\vec{H}_F^s \cong \frac{-jk}{4\pi\eta}\frac{e^{-jkr}}{r}\vec{L}_t = \frac{-jk_0}{4\pi\eta_0}\frac{e^{-jk_0r}}{r}(\hat{\theta}\cos\theta\cos\phi - \hat{\phi}\sin\phi)abE_0^i(1+R)\cos\theta_i\text{sinc}X\text{sinc}Y$$

Using the relationship between the scattered magnetic and electric fields results in an expression for the scattered electric field of a *TEM* wave due to the electric vector potential:

$$\vec{E}_F^s \cong -\eta\hat{r}\times\vec{H}_F^s = \frac{jk_0}{4\pi}\frac{e^{-jk_0r}}{r}\hat{r}\times(\hat{\theta}\cos\theta\cos\phi - \hat{\phi}\sin\phi)abE_0^i(1+R)\cos\theta_i\text{sinc}X\text{sinc}Y \tag{2.70}$$

$$\vec{E}_F^s = \frac{jk_0}{4\pi}abE_0^i(1+R)\frac{e^{-jkr}}{r}\cos\theta_i\text{sinc}X\text{sinc}Y(\hat{\theta}\sin\phi + \hat{\phi}\cos\theta\cos\phi)$$

The total scattered electric field is the superposition of the scattered electric fields due to the magnetic and electric vector potentials:

$$\vec{E}^s = \vec{E}_A^s + \vec{E}_F^s \tag{2.71}$$

RCS, when using the radiation zone approximation,(a.k.a. far-field approximation), is independent of range, r. Since $\vec{E}^s$ decays $\propto 1/r$, when squared, this term cancels with the r^2 term in the numerator.

$$\sigma = \lim_{r\to\infty} 4\pi r^2 \frac{|\vec{E}^s|^2}{|\vec{E}^i|^2} \tag{2.72}$$

where σ is RCS in units of square meters. Substituting (2.67) and (2.70) into (2.71) yields:

$$\vec{E}^s \approx \frac{jk_0}{4\pi}abE_0^i\frac{e^{-jk_0r}}{r}\text{sinc}X\text{sinc}Y... \tag{2.73}$$

$$...\left\{\hat{\theta}\sin\phi\left[(1+R)\cos\theta_i - (1-R)\cos\theta\right] + \hat{\phi}\cos\phi\left[(1+R)\cos\theta_i\cos\theta - (1-R)\right]\right\}$$

To compute $\left|\vec{E}^s\right|^2$ $\hat{\theta}$ terms and $\hat{\phi}$ terms are multiplied by their respective complex

conjugates and added according to the dot product for complex numbers:

$$\left|\vec{E}^s\right|^2 = \left(\hat{\theta}E_\theta^s + \hat{\phi}E_\phi^s\right)\cdot\left(\hat{\theta}E_\theta^s + \hat{\phi}E_\phi^s\right)^* = E_\theta^s E_\theta^{s*} + E_\phi^s E_\phi^{s*} = \left|E_\theta^s\right|^2 + \left|E_\phi^s\right|^2. \tag{2.74}$$

For parallel polarization, the incident electric field lies in the plane of incidence. In this

case, the plane of incidence is the $y-z$ plane. Therefore angle $\phi = -90^\circ$ and the

scattered electric field expression simplifies:

$$X = \frac{a}{2}k_0 \sin\theta_i \cos\phi = 0 \Rightarrow \mathrm{sinc}X = 1 \tag{2.75}$$

$$\left|\vec{E}^s\right|^2\Big|_{\phi=-90^\circ} = \left|\frac{k_0}{4\pi r}abE_0^i\mathrm{sinc}Y\left[(1+R)\cos\theta_i - (1-R)\cos\theta\right]\right|^2 \quad.$$

The squared magnitude of the incident electric field is

$$\left|\vec{E}^i\right|^2 = \left(E_0^i\hat{E}_0^i e^{-jk_0(y\sin\theta_i - z\cos\theta_i)}\right)\left(E_0^i\hat{E}_0^i e^{-jk_0(y\sin\theta_i - z\cos\theta_i)}\right)^* \tag{2.76}$$
$$\left|\vec{E}^i\right|^2 = \left(E_0^i\right)^2 \quad.$$

The radar cross section is independent of range, r. Since $\vec{E}^s$ decays $\propto \frac{1}{r}$, when squared,

this term cancels with the r^2 term in the numerator (2.77).

$$\sigma = \lim_{r\to\infty} 4\pi r^2 \frac{\dfrac{\left(E_0^i\right)^2}{(4\pi)^2 r^2}\left(k_0 ab\,\mathrm{sinc}Y\left[(1+R)\cos\theta_i - (1-R)\cos\theta\right]\right)^2}{\left(E_0^i\right)^2} \tag{2.77}$$

$$\sigma = \frac{\left(k_0 ab\,\mathrm{sinc}Y\left[(1+R)\cos\theta_i - (1-R)\cos\theta\right]\right)^2}{4\pi} \quad,$$

The physical optics approximation is valid for infinite planar surfaces where no edge

discontinuities are present to cause edge diffraction as depicted in Figure 2-21. Edge

diffraction gives rise to a TE or TM guided (hybrid mode in the general case) surface

wave in the medium. Guided surface waves and traveling waves are not accounted for by PO. The PO approximation remains valid for specular angles on finite width planar surfaces when the targets that are electrically large compared to wavelength. This requirement is shown in Figure 2-20 where $a, b \gg \lambda$. This is also true for surfaces that are locally planar such that the radius of curvature (for a singly-curved surface) is large enough such that the phase varies by no more than 22.5° as described in section 2.12.
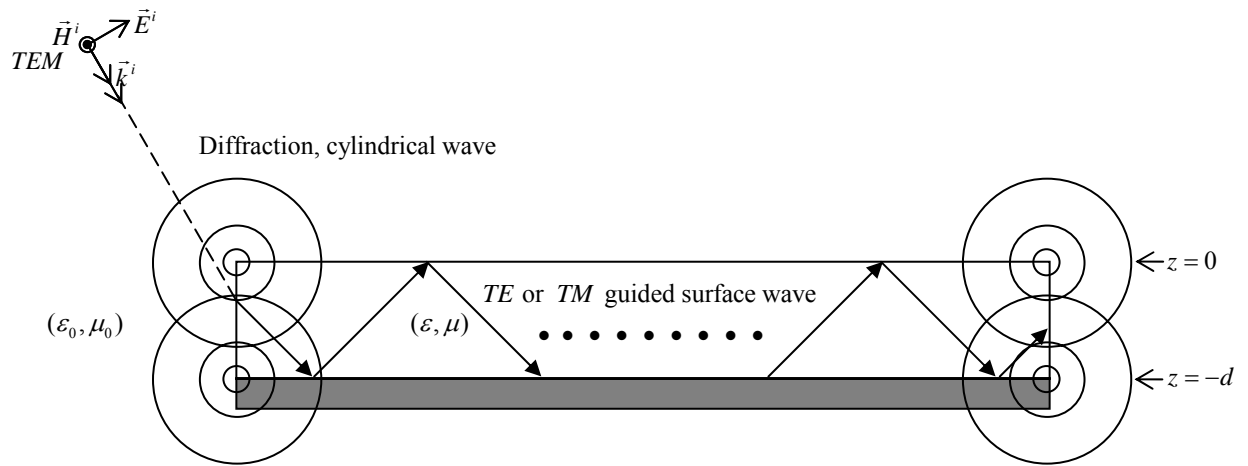
Figure 2-21: Edge diffraction from incident plane wave on finite-width plate

In the PO approximation given in (2.62) it is assumed that $\hat{n}$ points in the same direction across the entire surface area. Unlike a PEC plate, the material-covered plate is polarization dependent. In the case where R=-1 for a PEC plate, equation (2.59) and (2.62) are identical. Full-wave codes are the best choice for predicting specular behavior of targets that are small compared to wavelength. Other computational methods including PO, PTD, GO, GTD, and UTD are only valid for the optics region, i.e. targets are electrically large. Aside from diffraction, surface traveling waves are not accounted for by PO. Backscatter due to traveling waves occurs when a discontinuity is encountered; since PO assumes an infinite planar surface, traveling waves are not accommodated. Therefore, at angles away from normal incidence, the PO approximation

of RCS begins to yield inaccuracies. This is especially true in cases where the electric field lies in the plane of incidence thereby exciting surface current traveling waves. Neither does PO account for guided surface waves. Guided surface waves are electromagnetic waves guided through the material as transverse-electric and/or transverse-magnetic to the direction of propagation as shown in Figure 2-22, where the angle of incidence depicted at the interface between the medium and free space is the critical angle resulting in total internal reflection.
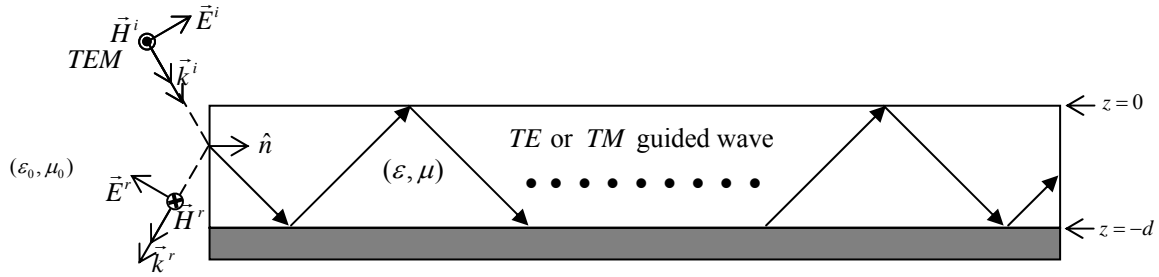
Figure 2-22: Surface-guided wave in a material

2.19.2 *Physical Optics Approximation of the Radar Cross Section of a Material-Coated PEC Finite Plate for Perpendicular Polarization*

Consider a perpendicularly-polarized, transverse, electromagnetic wave (*TEM*) is incident upon a finite width material-coated PEC rectangular plate of arbitrary length, a and width, b, as depicted in Figure 2-23. The field point position vector, $\vec{r}$ and source point position vector, $\vec{r}'$ are

$$\vec{r} = \hat{x}x + \hat{y}y + \hat{z}z$$

$$\vec{r}' = \hat{x}x' + \hat{y}y'$$

$$\hat{r} \cdot \vec{r}' = \hat{r} \cdot \hat{x}x' + \hat{r} \cdot \hat{y}y' = x'\sin\theta\cos\phi + y'\sin\theta\sin\phi$$

(2.78)

The incident direction vector, $\vec{k}_i$, is identical to parallel polarization case given by equation (2.54) above. The incident electric and magnetic fields are
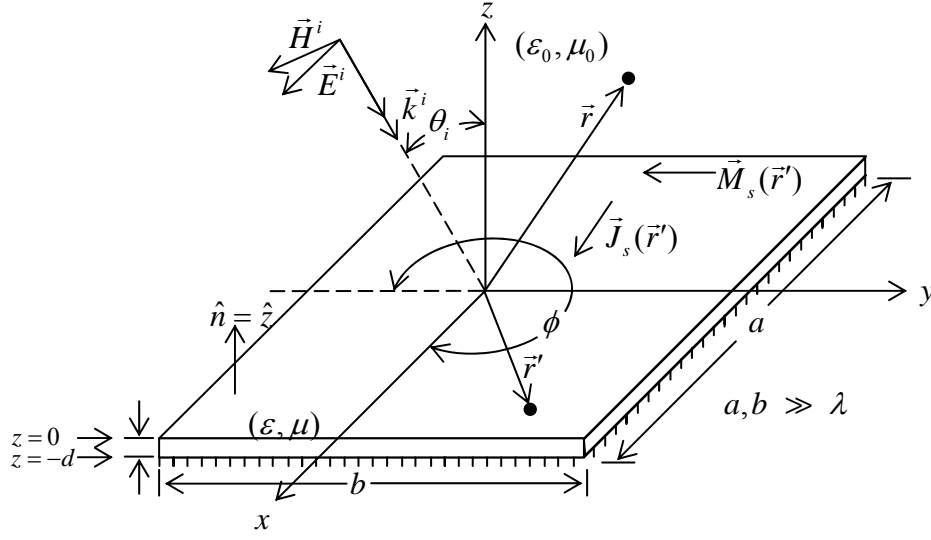
Figure 2-23: Material-coated PEC finite plate, perpendicular polarization

$$\vec{J}_s(\vec{r}') \cong (1-R)\hat{n}' \times \vec{H}^i(\vec{r}')\Big|_{\substack{z'=0 \\ \hat{n}'=\hat{z}'=\hat{z}}} = \hat{x}\frac{E_{0x}^i \cos\theta_i}{\eta_0}(1-R)e^{-jk_0 y'\sin\theta_i} \tag{2.79}$$

$$\vec{M}_s(\vec{r}') \cong -(1+R)\hat{n}' \times \vec{E}^i(\vec{r}')\Big|_{\substack{z'=0 \\ \hat{n}'=\hat{z}'=\hat{z}}} = -\hat{y}E_{0x}^i(1+R)e^{-jk_0 y'\sin\theta_i}$$

$$\vec{E}^i = \vec{E}_0^i e^{-j\vec{k}^i \cdot \vec{r}} = E_0^i \hat{E}_0^i e^{-j\vec{k}^i \cdot \vec{r}} = \hat{x}E_{0x}^i e^{-jk_0(y\sin\theta_i - z\cos\theta_i)} \tag{2.80}$$

$$\vec{H}^i = \frac{\hat{k}^i \times \vec{E}^i}{\eta} = (\hat{y}\sin\theta_i - \hat{z}\cos\theta_i) \times \hat{x}\frac{E_{0x}^i}{\eta_0} e^{-jk_0(y\sin\theta_i - z\cos\theta_i)}$$

$$= \frac{E_{0x}^i}{\eta_0}(-\hat{y}\cos\theta_i - \hat{z}\sin\theta_i)e^{-jk_0(y\sin\theta_i - z\cos\theta_i)}$$

Using the perpendicular wave impedance, the physical optics current approximations are

$$\vec{J}_s(\vec{r}') \cong (1-R)\hat{n}' \times \vec{H}^i(\vec{r}')\Big|_{\substack{z'=0 \\ \hat{n}'=\hat{z}'=\hat{z}}} = \hat{x}\frac{E_{0x}^i \cos\theta_i}{\eta_0}(1-R)e^{-jk_0 y'\sin\theta_i} \tag{2.81}$$

$$\vec{M}_s(\vec{r}') \cong -(1+R)\hat{n}' \times \vec{E}^i(\vec{r}')\Big|_{\substack{z'=0 \\ \hat{n}'=\hat{z}'=\hat{z}}} = -\hat{y}E_{0x}^i(1+R)e^{-jk_0 y'\sin\theta_i}$$

Using the radiation integral, $\vec{N}$, the scattered electric field due to the magnetic vector

potential for the material-covered rectangular plate can be calculated:

$$\vec{N} = \int_S \vec{J}_s(\vec{r}')e^{jk\hat{r}\cdot\vec{r}'}ds' = \int_{-b/2}^{b/2}\int_{-a/2}^{a/2}\hat{x}\frac{E_{0x}^i\cos\theta_i}{\eta_0}(1-R)e^{-jk_0y'\sin\theta_i}e^{jk_0(x'\sin\theta\cos\phi+y'\sin\theta\sin\phi)}dx'dy' \quad (2.82)$$

$$\vec{N} = \hat{x}\frac{E_0^i\cos\theta_i}{\eta_0}(1-R)\int_{-a/2}^{a/2}e^{jk_0x'\sin\theta\cos\phi}dx'\int_{-b/2}^{b/2}e^{jk_0y'(\sin\theta\sin\phi-\sin\theta_i)}dy'$$

$$\int_{-a/2}^{a/2}e^{jk_0x'\sin\theta\cos\phi}dx' = a\operatorname{sinc}X \;\;;\; \text{where } X = \frac{a}{2}k_0\sin\theta\cos\phi;$$

$$\int_{-b/2}^{b/2}e^{jk_0y'(\sin\theta\sin\phi-\sin\theta_i)}dy' = b\operatorname{sinc}Y; \;\; \text{where } Y = \frac{b}{2}k_0(\sin\theta\sin\phi-\sin\theta_i)$$

$$\vec{N} = \hat{x}ab\frac{E_0^i\cos\theta_i}{\eta_0}(1-R)\operatorname{sinc}X\operatorname{sinc}Y$$

The scattered electric field due to the magnetic vector potential $\vec{A}$ is then formulated

using the transverse components of $\vec{N}$:

$$\vec{N}_t = \left[\hat{\theta}(\hat{\theta}\cdot\hat{x}) + \hat{\phi}(\hat{\phi}\cdot\hat{x})\right]ab\frac{E_0^i\cos\theta_i}{\eta_0}(1-R)\operatorname{sinc}X\operatorname{sinc}Y \quad (2.83)$$

$$(\hat{\theta}\cdot\hat{x}) = \cos\theta\cos\phi; \qquad (\hat{\phi}\cdot\hat{x}) = -\sin\phi$$

$$\vec{E}_A^s \cong -\frac{jk\eta}{4\pi}\frac{e^{-jkr}}{r}\vec{N}_t = -\frac{jk_0\eta_0}{4\pi}\frac{e^{-jkr}}{r}\vec{N}_t$$

$$\vec{E}_A^s = -\frac{jk_0}{4\pi}ab\cos\theta_i E_{0x}^i(1-R)\frac{e^{-jk_0r}}{r}\operatorname{sinc}X\operatorname{sinc}Y(\hat{\theta}\cos\theta\cos\phi-\hat{\phi}\sin\phi)$$

Similarly, the radiation integral, $\vec{L}$, for calculating the scattered magnetic field

due to the electric vector potential $\vec{F}$ for the material covered rectangular plate is

$$\vec{L} = \int_S \vec{M}_s(\vec{r}')e^{jk\hat{r}\cdot\vec{r}'}ds' = \int_{-b/2}^{b/2}\int_{-a/2}^{a/2}-\hat{y}E_{0x}^i(1+R)e^{-jk_0y'\sin\theta_i}e^{jk_0(x'\sin\theta\cos\phi+y'\sin\theta\sin\phi)}dx'dy' \quad (2.84)$$

$$\vec{L} = -\hat{y}E_{0x}^i(1+R)\int_{-a/2}^{a/2}e^{jk_0x'\sin\theta\cos\phi}dx'\int_{-b/2}^{b/2}e^{jk_0y'(\sin\theta\sin\phi-\sin\theta_i)}dy'$$

$$\vec{L} = -\hat{y}abE_{0x}^i(1+R)\operatorname{sinc}X\operatorname{sinc}Y$$

The scattered magnetic field due to the electric vector potential $\vec{F}$ is then computed

using the transverse components of $\vec{L}$:

$$\vec{L}_t = \hat{\theta}L_\theta + \hat{\phi}L_\phi = -\left[\hat{\theta}(\hat{\theta}\cdot\hat{y}) + \hat{\phi}(\hat{\phi}\cdot\hat{y})\right]abE_{0x}^i(1+R)\text{sinc}X\text{sinc}Y \tag{2.85}$$

$$(\hat{\theta}\cdot\hat{y}) = \cos\theta\sin\phi; \qquad (\hat{\phi}\cdot\hat{y}) = \cos\phi \qquad .$$

Using the relationship between the scattered magnetic and electric fields results in an expression for the scattered electric field of a *TEM* wave due to the electric vector potential:

$$\vec{H}_F^s \cong \frac{-jk}{4\pi\eta}\frac{e^{-jkr}}{r}\vec{L}_t = \frac{jk_0}{4\pi\eta_0}\frac{e^{-jk_0r}}{r}(\hat{\theta}\cos\theta\sin\phi + \hat{\phi}\cos\phi)abE_{0x}^i(1+R)\text{sinc}X\text{sinc}Y \tag{2.86}$$

$$\vec{E}_F^s \cong -\eta\hat{r}\times\vec{H}_F^s = \frac{jk_0}{4\pi}\frac{e^{-jk_0r}}{r}\hat{r}\times(\hat{\theta}\cos\theta\sin\phi + \hat{\phi}\sin\phi)abE_{0x}^i(1+R)\text{sinc}X\text{sinc}Y \quad .$$

$$\vec{E}_F^s = \frac{jk_0}{4\pi}abE_{0x}^i(1+R)\frac{e^{-jk_0r}}{r}\text{sinc}X\text{sinc}Y(\hat{\theta}\cos\phi - \hat{\phi}\cos\theta\sin\phi)$$

The total scattered electric field is the superposition of the scattered electric fields due to the magnetic and electric vector potentials:

$$\vec{E}^s = \vec{E}_A^s + \vec{E}_F^s \tag{2.87}$$

$$\vec{E}^s \approx \frac{jk_0}{4\pi}abE_{0x}^i\frac{e^{-jk_0r}}{r}\text{sinc}X\text{sinc}Y...$$

$$...\left\{\hat{\theta}\cos\phi\left[(1+R) - \cos\theta_i\cos\theta(1-R)\right] + \hat{\phi}\sin\phi\left[\cos\theta_i(1-R) - \cos\theta(1+R)\right]\right\} .$$

$$\vec{E}^s = \hat{\theta}E_\theta^s + \hat{\phi}E_\phi^s$$

$$\left|\vec{E}^s\right|^2 = \left(\hat{\theta}E_\theta^s + \hat{\phi}E_\phi^s\right)\cdot\left(\hat{\theta}E_\theta^s + \hat{\phi}E_\phi^s\right)^* = E_\theta^s E_\theta^{s*} + E_\phi^s E_\phi^{s*} = \left|E_\theta^s\right|^2 + \left|E_\phi^s\right|^2$$

The incident electric field is perpendicular to the plane of incidence which in this case is the y-z plane. Therefore angle ϕ is -90°. For the monostatic case $\theta_i = \theta$. Making these substitutions, the expression for the scattered electric field simplifies:

$$\left|\vec{E}^s\right|^2_{\phi=-90°} = \left(\frac{k_0}{4\pi r}abE_{0x}^i\text{sinc}Y\left[\cos\theta_i[(1-R) - (1+R)\cos\theta_i]\right]\right)^2 \tag{2.88}$$

$$\left|\vec{E}^s\right|^2_{\phi=-90°} = \left(\frac{-2Rk_0}{4\pi r}abE_0^i\text{sinc}Y\cos\theta_i\right)^2 \qquad .$$

Using the simplified expression for the scattered electric field, the PO approximation of the RCS of a material-coated finite plate for parallel polarization is

$$\sigma = \lim_{r \to \infty} 4\pi r^2 \frac{\left(-2Rk_0 \text{absincY} \cos\theta_i\right)^2 \dfrac{\left(E_0^i\right)^2}{\left(4\pi\right)^2 r^2}}{\left(E_0^i\right)^2}.$$

$$\sigma = \frac{\left(Rk_0 \text{absincY} \cos\theta_i\right)^2}{\pi}$$

(2.89)

Equation (2.89) shows that the physical optics approximation of the RCS of a material-coated, finite plate for parallel polarization is independent of the incident electric field and range as long as far zone criteria are met.

2.20 Impedance Boundary Conditions

FISC's IBC formulation assumes a high-contrast medium where the index of refraction of the medium is much greater than the index of refraction of free space. Due to the high index of refraction it is assumed that the incident field, once in the medium, is normally incident upon a PEC backing. Given these assumptions, the formula describing the surface impedance is [13]

$$\eta_s = j\eta \tan(kd),$$

(2.90)

where η_s is the surface impedance, η is the intrinsic impedance of the medium, k is the wavenumber in the medium and d is the medium thickness. Incorporating angle- and including polarization-dependence yields [3]:

$$\eta_{s\perp} = jZ_\perp \tan(k_{1z}d) \quad \text{... perpendicular polarization}$$
$$\eta_{s\parallel} = jZ_\parallel \tan(k_{1z}d) \quad \text{... parallel polarization} \quad ,$$

(2.91)

where $Z_\perp$, $Z_\parallel$, and k_{1z} are defined as

$$Z_{\perp} = \frac{\eta}{\cos\theta_{inc}};$$

$$Z_{\parallel} = \eta\cos\theta_{inc};$$

$$k_{1z} = k_0\sqrt{\mu_r\varepsilon_r - \sin^2\theta_{inc}}$$

(2.92)

In Chapter 4, FISC's default IBC given by (2.90), and the modified IBC formulation given by (2.91) are compared to measured data for a 12″×12″ MRAM-coated PEC flat plate. In summary, impedance boundary conditions can be expressed as functions of frequency, thickness of the material, material parameters, polarization and angle of incidence:

1. η_{s_FISC} ... $f(f,d,\mu_r,\varepsilon_r)$

2. $\eta_{s\_general}$ ... $f(f,d,\mu_r,\varepsilon_r,pol,\theta_{inc})$.

(2.93)

3   *Methodology*

Analysis of the performance of RCS predictions can be conducted by comparison of predicted results to measured data or comparison of predicted results between two full wave solvers. In this thesis, both methods are employed to compare predicted results against the well-known hip-pocket RCS approximations. Sections 3.1 and 3.2 describe the physical models and CAD models used for RCS comparison and code performance evaluation. Section 3.3 discusses the criteria for sampling in azimuth to meet Nyquist criterion. Sections 3.4 and 3.5 describe the experimental setup for comparison of FISC's IBC feature to experimental measurements. Section 3.6 defines the metrics used for RCS comparison. Equation Chapter (Next) Section 3

3.1   *CAD models for RCS Comparison*

The ballistic missile model shown in Figure 2-1 with dimensions given in Table 2-1 is the complex target chosen for RCS comparisons. RCS of each constituent part of the model is also predicted and measured to establish confidence in solution accuracy. Since this thesis does not examine any of the volumetric material capabilities specific to SAF, RCS data is generated only for the cylinder to verify agreement with FISC and to examine code performance. The complex model is measured and predicted at 400 and 500 MHZ corresponding to a 24λ and 30λ target length. The missile is designed such that it would be of an electrical size to challenge the computational performance and maximum problem size of FISC and CARLOS. For example, the solution time for the 400 MHz missile to compute 180 angles at 0.5° increments with $\lambda/10$ grid density was 64 hours. CARLOS 3-D max problem size of 70,000 unknowns is exceeded by the booster stage.

For this reason CARLOS-BOR is used to compare with FISC results rather than CARLOS 3-D.
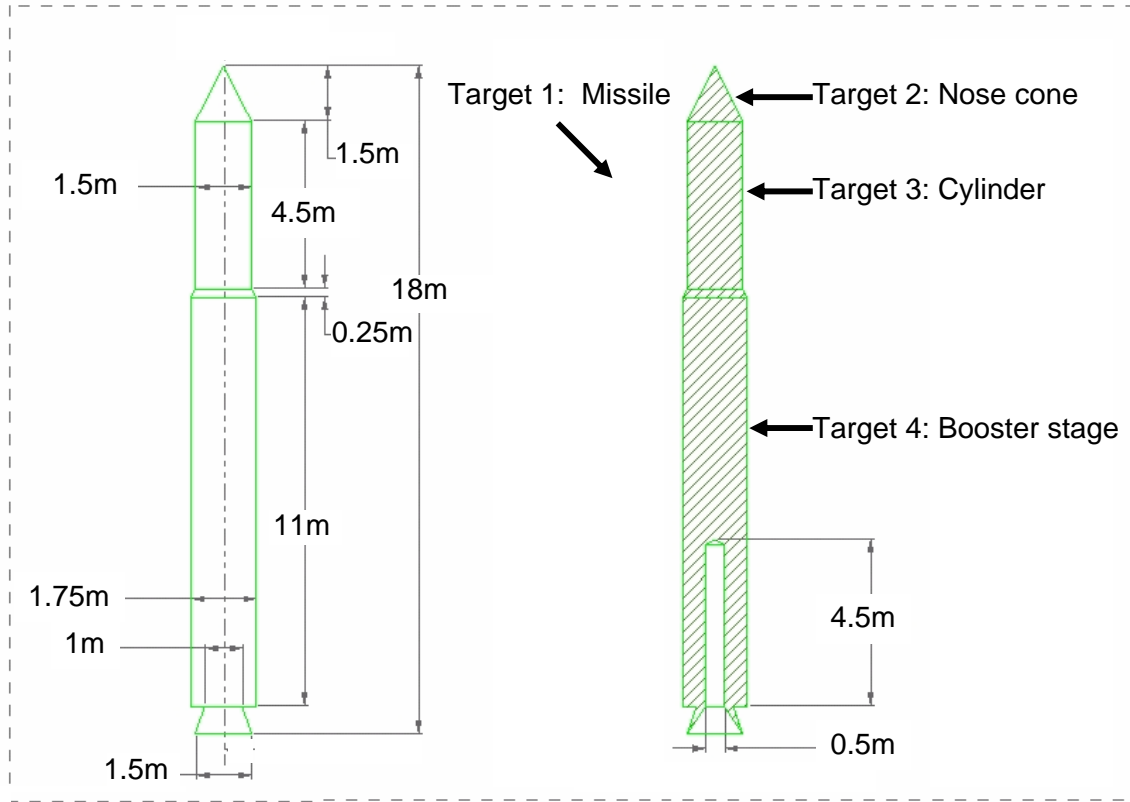
Figure 3-1: Missile model and constituent components

Table 3-1: Model Dimensions

	Full-Scale (m)	1/36 Scale (m)	1/36 Scale (in)
Missile length	18	0.5000	19.685
Booster stage radius	0.875	0.0243	0.957
Upper cylinder radius	0.75	0.0208	0.820
Upper cylinder height	4.5	.125	4.921
Nose cone height	1.5	0.0417	1.640
Nose cone radius	0.75	0.0208	0.820
Cone frustrum height	0.25	0.0069	0.273
Cone frustrum width	0.75–0.875	0.0208–0.0243	0.820–0.957
Exhaust nozzle depth	0.75	0.0208	0.820
Exhaust nozzle width	0.5– 0.75	0.0139–0.0208	0.547–0.820
Cavity depth (as shown)	4.5	0.12500	4.921
Cavity diameter	0.5	0.0139	0.547

CAD models and physical models were designed to match as closely as manufacturing

tolerances would permit. These models were also composed of simple shapes in order to

make comparisons to well-known signatures. Table 3-2 lists all of the targets used in this

study and whether analysis will be for performance, for RCS analysis or both. Each

target type requires several grid densities or edge counts for either proof of convergence

or performance analysis.

Table 3-2: Target Models

	Target	Performance Analysis	RCS	Grid Densities & Edge Counts
1	Missile	X	X	$\lambda/10$, $\lambda/12$, $\lambda/15$ 5k, 10k, 15k, 20k edges
2	Missile nose cone	X	X	$\lambda/10$, $\lambda/12$, $\lambda/15$ 5k, 10k, 15k, 20k edges
3	Missile upper cylinder (open)	X		5k, 10k, 15k, 20k edges
4	Missile upper cylinder (closed)	X	X	$\lambda/10$, $\lambda/12$, $\lambda/15$ 5k, 10k, 15k, 20k edges
6	Booster stage	X	X	$\lambda/10$, $\lambda/12$, $\lambda/15$ 5k, 10k, 15k, 20k edges
7	PEC large cone	X	X	$\lambda/10$, $\lambda/12$, $\lambda/15$
8	MRAM large cone	X	X	$\lambda/10$, $\lambda/12$, $\lambda/15$
9	PEC Plate	X	X	$\lambda/10$
10	MRAM Plate	X	X	$\lambda/10$

3.1.1 Missile model and subcomponents

The physical model shown in Figure 3-1 is fabricated using a 6061 aluminum alloy 6″

diameter rod at 1/36 scale. Full-sized and scaled dimensions are listed in Table 3-1.

There are five noted inconsistencies between the physical model and the CAD models.

The first inconsistency is due to the tolerances of the manufacturing process. The model

is made to a precision of 1/5000 of an inch, whereas the CAD model is exact. Therefore,

the measurements listed in the third column of Table 3-1 have a tolerance of $\pm 0.0025″$.

Secondly, the physical edges of the model are as sharp as could be manufactured but all

physical edges are rounded, whereas the CAD models are perfectly sharp. Third,

surfaces of the model are not perfectly smooth. The lathe which produced the model

leaves a slight ridged texture from multiple passes with a cutting bit. The interior of the

exhaust cavity is perhaps the roughest surface since it is created with a drill bit and is not

polished. Fourth, the back wall of the cavity is rounded rather than pointed inward due to

the shape and sharpness of the drill bit. The last inconsistency is with the interior angle

of the back wall of the cavity. From the target model dimension listed in Table 3-1, the

interior angle is 119.7° whereas the actual angle is 120° corresponding to the angle of the

tip of the drill bit. This angle difference is a known contributor to the difference between

the measured and predicted results for CARLOS and FISC for the cavity aspect. The

diameter of the cavity was designed to be large enough to allow mode propagation. A

circular cavity having a radius of 0.25 meters allows a dominant mode, TE_{11} to propagate.

Eight modes will propagate into this cavity for frequencies less than 1 GHz. Table 3-3

lists the modes and the associated cutoff frequencies, f_c, for this cavity.

Table 3-3: Modes and cutoff frequencies for missile cavity

Mode	f_c
TE_{11}	351.4038 MHz
TM_{01}	458.9892 MHz
TE_{21}	582.9119 MHz
TE_{01}	731.3214 MHz
TM_{11}	731.3214 MHz
TE_{31}	801.8235 MHz
TM_{21}	980.1783 MHz

3.1.2   *CARLOS BOR missile model*

Body of revolution targets in CARLOS must ensure that surface normals are

defined to point outward from the scatterer interior, namely:

$$\hat{n} = \hat{\phi} \times \hat{t} \, , \tag{3.1}$$

where $\hat{\phi}$ is the direction of rotation about the z axis and $\hat{t}$ is the direction of the tangent to the surface along the line defining the geometry. An easy way to ensure that the surface normals are properly-oriented, is to define the geometry as shown in Figure 2-1 and use a right-hand rule approach. For example, start listing points in 'to-from' order from A through J in the CARLOS input page(see appendix C). This is further illustrated in Figure 3-2 and Figure 3-3, where the surface normal points away from the missile body interior. The coordinates used for the missile are listed in Table 3-4.
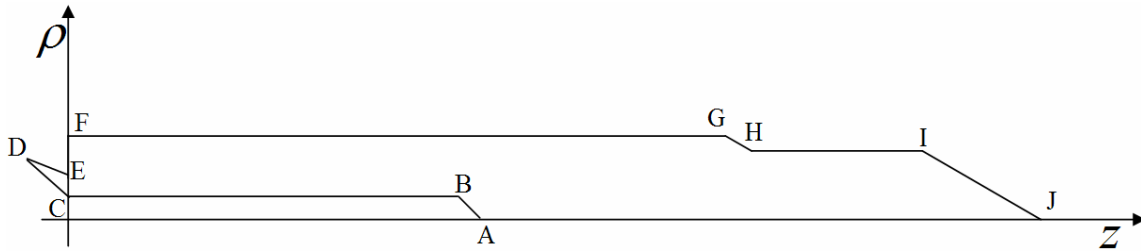
Figure 3-2: Body of revolution geometry for missile model
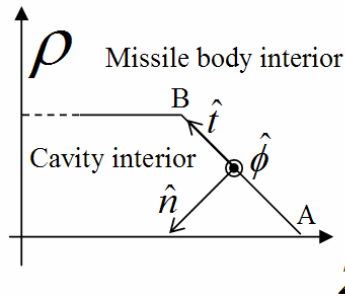
Figure 3-3: Defining BOR geometry for outward-pointing surface normals

Table 3-4: Point coordinates for BOR missile

Point	ρ (mm)	z (mm)
A	0	4500
B	250	4355
C	250	0
D	750	-750
E	500	0
F	875	0
G	875	11000
H	750	11250
I	750	15750
J	0	17250

3.1.3 CAD Performance models

Code performance in memory and processing time is performed by using the following CAD models with a specified number of unknowns. Performance for SAF was performed only for the missile cylinder. The number of unknowns for a three-dimensional closed surface is equal to 1.5 times the number of facets. The frequency used for the RCS prediction is determined by letting the average edge length of the model be $\lambda/10$.

Table 3-5: Performance CAD models

Model	Resolution
Cylinder, Closed End Caps	5k, 10k, 15k, 20k, 35k, 55k edges
Flat-Backed Cone	5k, 7k, 8k, 9k, 10k, 11k, 12k, 15k, 20k edges
Booster Stage	5k, 10k, 12k, 20k, 48k,70k, 86k, 109k, 171k edges
Missile	49k, 123k, 160k, 166k, 189k,192k, 222k, 255k, 264k edges

A model having 5000 (5k) edges was generated for the first three of the above geometries. Since doubling the frequency for a given discretization level will increase the edge count by four as discussed in Section 2.15.4, the 20k edge model was created as follows:

1. Calculate the frequency for the 5k model with 0.1λ average edge length

   This was done with a MATLAB® script that analyzes the CAD file.

2. Double the frequency and enter parameters into a FISC input page.

3. Set maximum edge length to 0.1λ (section C, "EM Settings", FISC input page)

4. Choose the option for FISC to output a refined facet file showing the currents

(section C, "EM Settings", FISC input page). This is the 20k edge facet file.

The 15k edge models were created by iteratively increasing the frequency calculated for the 10k model until the edge count approached 15k. As the frequency was increased, FISC steadily split facets having edge lengths longer than $\lambda/10$ into smaller ones thereby increasing the edge count. The facets nearby the refined facets are also refined so that the model remains well-connected, without any hanging nodes. Since FISC does not remesh the geometry, the original nodes remain fixed. As the frequency is increased a point is reached where all facets are now longer than $\lambda/10$. When this point is reached, FISC splits all facets with the result that the edge count increases by a factor of 4. This is expected since there is a factor of 4 increase in facets whenever all facets are split as was explained in section 2.15.4. Using this trial and error process, the files with edge counts between 12k and 15k were created.

3.2   RCS Measurements

Table 3-6 contains the he test matrix for the physical models. The measurements were taken at the AFRL compact RCS/antenna measurement range (Figure 3-4). The RCS for the missile model and components was measured at 14.4, 18, and 36 GHz corresponding to scaled frequencies, 0.4, 0.5 and 1 GHz respectively.

Table 3-6: Measurement test matrix

Target	Azimuth (degrees)	Frequency
Missile	0:0.5:360	2:0.1:18 GHz
Nose cone	0:0.1:360	2:.1:18 GHz
Upper cylinder	0:0.1:360	2:0.5:18 GHz
Booster stage	0:0.1:360	2:0.1:18 GHz
Nose cone height	0:0.5:360	2:0.1:18 GHz
Nose cone radius	0:0.1:360	2:0.1:18 GHz
PEC large cone	0:0.1:360	2:0.1:18 GHz
MRAM large cone	0:0.5:360	2:0.1:18 GHz
PEC Plate	0:0.5:360	2:0.1:18 GHz
MRAM Plate	0:0.5:360	2:0.1:18 GHz

Figure 3-4: Large PEC cone on mount at AFRL compact RCS range

All targets were measured at 0° elevation angle, a.k.a. waterline cut, and sampled in azimuth at either 0.1° or 0.5°.

3.3   Nyquist Sampling

To ensure proper representation of the RCS pattern, Nyquist criteria for sampling in azimuth should satisfy,

$$\Delta\theta = \frac{\lambda}{2x},$$
(3.2)

where $\Delta\theta$ is in radians, x is the longest dimension of the target [11], and λ is the wavelength corresponding to the frequency of the incident electromagnetic wave. The minimum angular sampling required for 500 MHz is shown in Table 3-7.

Table 3-7: Minimum angular sampling required for each target

Target	Longest Dimension (m)	Minimum Sampling (deg)
Right Circular Cone	.23	74.7
Nose Cone	.75	22.9
Cylinder	4.5	3.8
Booster Stage	12	1.4
Missile	18	0.95

An angular increment of 0.5° is more than sufficient for the full-size missile target to meet the sampling criterion.

3.4 Impedance boundary conditions investigation using square plates

A comparison is conducted between measured and predicted results for 12″×12″ flat plates using FISC's IBC feature. The MRAM material applied to the plates, Figure 3-5: 12″×12″ MRAM-coated PEC flat plate, was Eccosorb® FGM-40, a flexible, magnetically-loaded, electrically non-conductive silicone sheet having a 40 mil thickness (1.016mm) and a pressure-sensitive adhesive backing.
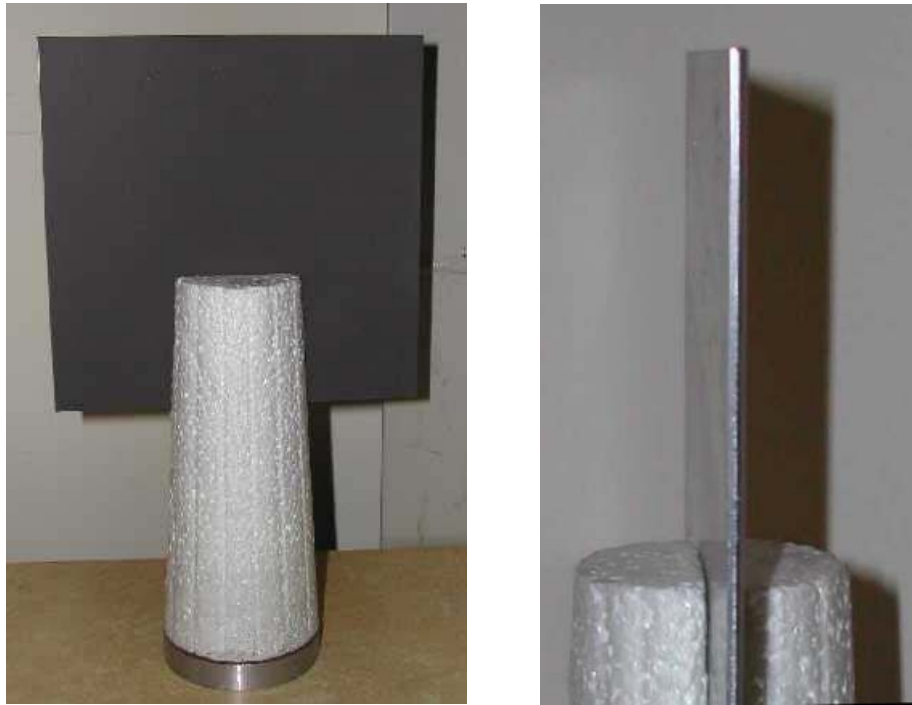
Figure 3-5: 12″×12″ MRAM-coated PEC flat plate
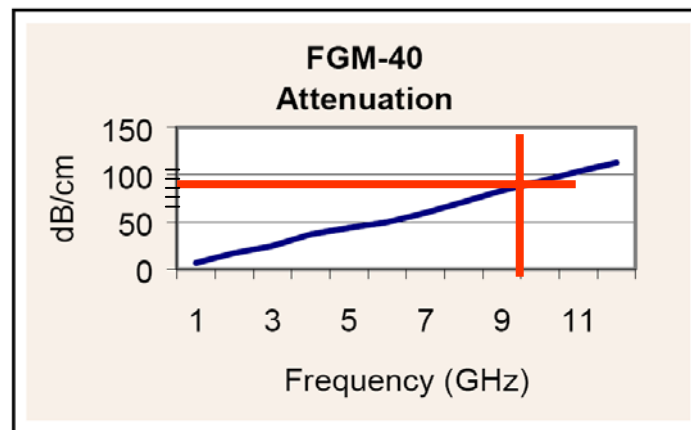
Figure 3-6: FGM-40 attenuation, 9 GHz, 1.016mm thickness

At 9 GHz, the expected attenuation in RCS from the manufacturer's specifications given

in Figure 3-6: FGM-40 attenuation, 9 GHz, 1.016mm thickness above is

$$\frac{90 dB}{cm} \times \frac{1\ cm}{100\ mm} \times 1.016 mm = 9.144 dB .$$ (3.3)

FISC's default IBC formulation which is independent of angle of incidence and polarization of the incident field is compared to measured data. The IBC formulation is then generalized for polarization and angle-dependent impedances to investigate prediction improvement. The PO method for predicting RCS of a material-coated PEC flat plate developed in section 2.19 is also compared to measured RCS and FISC RCS predictions. Results of each part of the comparison will be presented in chapter 4. There were three independent sources for the permittivity and permeability data given in Table 3-8. The first source was the manufacturer given and was only available on whole frequency increments. The permittivity values given by the manufacturer were suspect due to the fact that they differed significantly permittivity from two independent material measurements. The second data source is from measurements taken by General Electric's focus arch system and then processed using a Nicolson-Ross-Weir (NRW) method to extract the complex permittivity and permeability [20]. The last data source is from an X-band waveguide measurement and also processed using the NRW method. For more information on free-space and waveguide material measurements, see Cassell's [20].

Table 3-8: Material parameters for FGM-40

Data Source	Frequency	ε_{real}	$\varepsilon_{imaginary}$	μ_{real}	$\mu_{imaginary}$
Waveguide	9 GHz	24.000	-1.244	2.007	-2.136
Focus arch	9 GHz	25.690	-1.262	1.633	-2.124
Manufacturer	9 GHz	30.000	-1.000	1.600	-2.800

3.5 *Impedance boundary condition investigation using large PEC and MRAM-coated cones*

A comparison was conducted between measured and predicted results for PEC and MRAM-coated PEC 9″×9″ right circular cones. The MRAM material was again

Eccosorb® FGM-40, having a 40 mil thickness (1.016mm) and a pressure-sensitive

adhesive backing. The plates cones measured at the AFRL compact RCS/antenna

measurement range and then predicted with the use of FISC's impedance boundary

condition feature. The dimensions for the cones were chosen to be 1/10th of the physical

dimensions of a realistically-proportioned re-entry vehicle (RV) as shown in Table 3-9.

Figure 3-7 shows current distribution across the PEC cone using FISC's feature to create

a facet file to display induced current on the target (refer to Section C, "EM Setting" of

Appendix E).

Table 3-9: Large PEC/MRAM cone dimensions

	Full-Scale	1/10th scale(SI)	1/10th scale(inches)
Full-Size RV (Right Circular Cone)	2.3 m	0.23 m	9.0551″
Phenolic coating thickness	10-20 mm	1.016 mm	40 mil
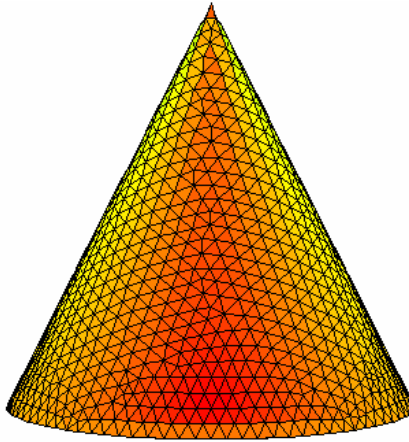
Figure 3-7: FISC output facet file showing current distribution across a PEC cone

3.6 RCS Comparison Metrics

To provide a quantitati ve method for comparing two RCS signatures, this thesis

uses two metrics for RCS measurement comparison: the correlation coefficient (CC) and

dB –deviation, MSE_{dBsm}. The correlation coefficient quantifies how well one plot

matches the next in terms of lobing and is insensitive to differences in amplitude values. MSE_{dBsm} is calculated using a method identical to mean-square error but uses the values in decibels for comparison. The reason for comparing the converted dB values rather than the actual linear RCS values is due to the large dynamic range inherent to RCS signatures. Two signatures that match peak amplitudes well but do not match in lobing structure could score better than two signatures that match lobing structure well but have peaks that are slightly different. In the latter case, the MSE_{dBsm} is not impacted as greatly as MSE for linear values. For MSE_{dBsm} comparisons of multiple RCS patterns, one signature is chosen as "truth" data where truth is defined to be agreement of two MoM solutions or agreement of a MoM solution and a measurement. For evaluation of material-coated PEC objects, measurement data is considered truth data. These quantitative measurements are supplemental to the qualitative evaluation and comparison to hip-pocket RCS formulas (when applicable). A convention used throughout this thesis is that the first value listed in the header of the RCS plot is the value chosen to be truth data.

3.6.1   RCS Signature Correlation Coefficient

The correlation coefficient is calculated using equation (3.4):

$$-1 \leq \frac{\sum_{n=1}^{N}\left(f_1(x_n)\cdot f_2(x_n)\right)}{\sqrt{\sum_{n=1}^{N}\left(f_1^2(x_n)\right)\sum_{n=1}^{N}\left(f_2^2(x_n)\right)}} \leq 1, \tag{3.4}$$

where $f_1(x_n)$ and $f_2(x_n)$ are the functions representing the RCS pattern as a function of the azimuth, x_n is the azimuth angle. Figure 3-8 shows pattern cuts of two cylinders rotated in azimuth VV polarization at 7 GHz. The closed cylinder used for the prediction

is shown in Figure 3-9. One cylinder has an open end-cap while the other is closed on

both ends. As evident from (3.4), $f_1(x_n)$ and $f_2(x_n)$ are interchangeable. Complete

correlation means that two RCS patterns match exactly in lobing structure and the

correlation coefficient is +1. In Figure 3-8 (b) red trace values are one and a half (1.5)

times the blue traces values, yet the correlation coefficient is +1. For complete

decorrelation, as shown in Figure 3-8(d), the coefficient is -1. In Figure 3-8 (a) the two

pattern cuts differ in the aspect angle viewing the open cavity. As is evident, the

correlation coefficient has a high value due to lobe matching over most azimuth angles

but does not suffice to quantify the difference in the waveforms from 300°–360° and 0–

60° degrees where diffuse scattering due to the open cavity is present. As can be

concluded from Figure 3-8 (a) and (b) another metric, MSE_{dBsm} introduced in the next

section, is needed to further quantify the RCS pattern differences. Figure 3-8 (c) shows a

comparison of the closed cylinder with the same data shifted by 45 degrees. The value

for the correlation coefficient is 0.83668 and will not go lower than this value for any

degree shift. Figure 3-9 shows a facetized version of the physical model used to create

the data in Figure 3-8.
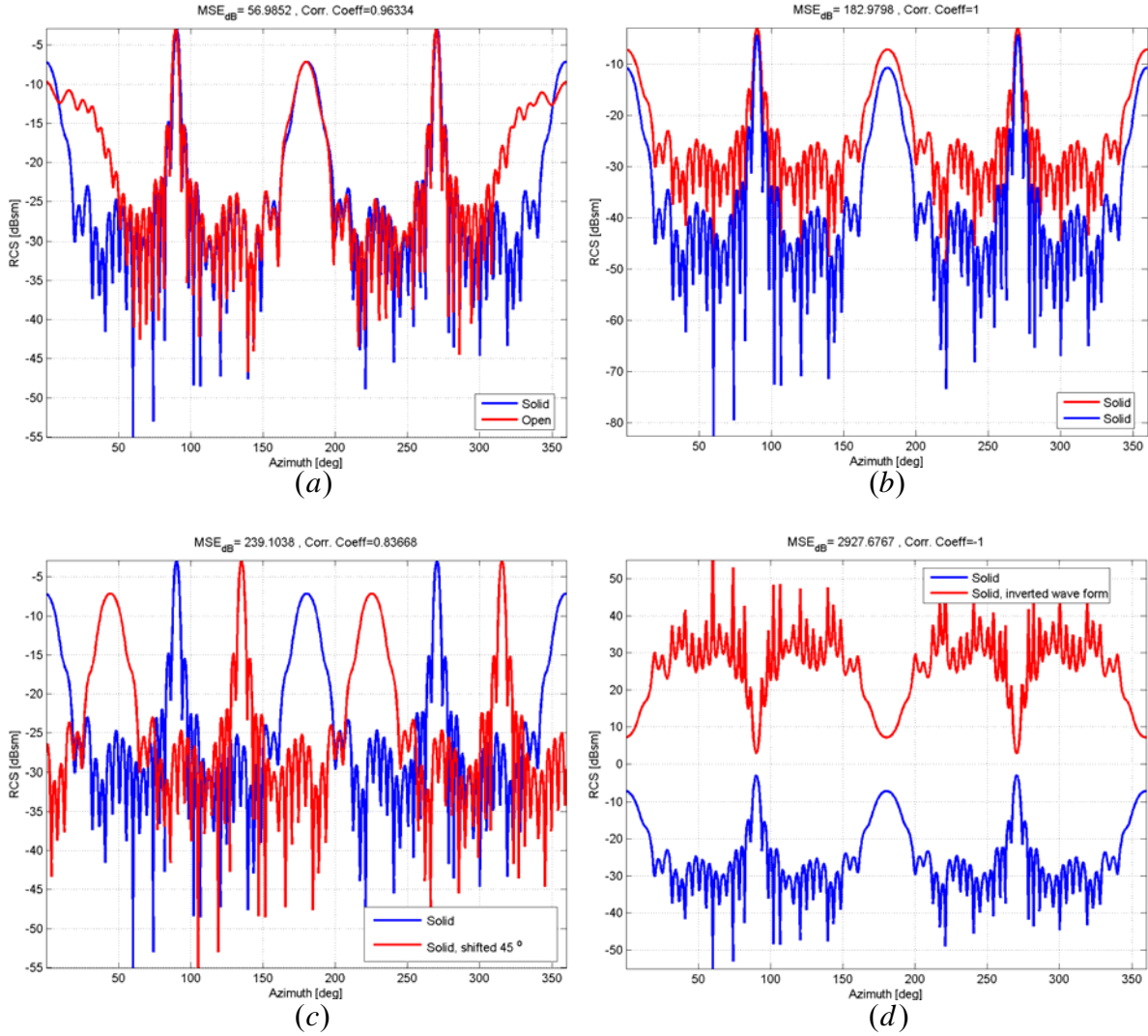
Figure 3-8: Examples of MSE_{dBsm} and Correlation Coeffient (CC) as metrics to quantify differences between RCS patterns, (a) CC= 0.96334, MSE_{dBsm}= 56.9852 for comparison of an RCS pattern cut of a cylinder with one open end with the RCS pattern cut of a closed cylinder, VV polarization, at 7 GHz (b) CC = 1, MSE_{dBsm}= 182.9798 for the comparison of two RCS pattern cuts, amplitude of blue trace values are 1.5 times the amplitude of the red trace values. (c) CC = 0.83668, MSE_{dBsm}= 239.1038 for the comparison of the closed cylinder RCS pattern cut with the same data shifted by 45° (d) CC = -1, MSE_{dBsm} = 2927.6767 for the comparison of the closed cylinder RCS pattern with the same data inverted.
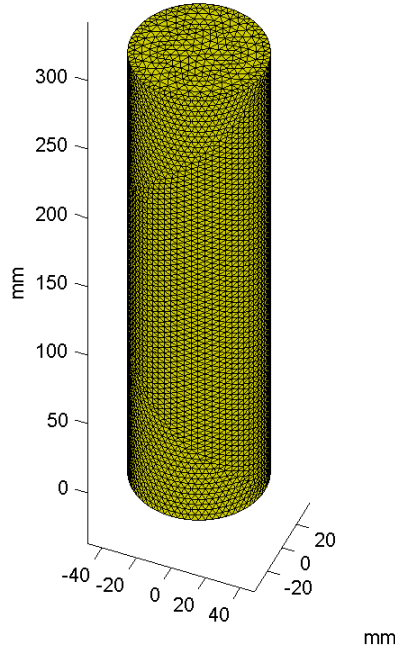
Figure 3-9 Facetized PEC cylinder having closed end caps, 7GHz discretization with maximum edge length of λ/12.

3.6.2 Mean Square Error, Decibel Deviation

Mean Square Error (MSE), also referred to as mean square deviation (MSD), equals the mean of the squares of the deviations from the target values:

$$MSE = \frac{1}{m} \sum_{i=1}^{m} (x_i - T_i)^2 , \qquad (3.5)$$

where x_i is the ith value of a group of m values and T_i is the true value. In this analysis, the decibel values are compared rather than the linear values. For this reason, MSE is identified as MSE_{dBsm} and when used, it will be indicated that one of the RCS patterns is truth data. Two RCS patterns that match exactly will have an MSE_{dBsm} =0. In Figure 3-8(b), a completely correlated waveform, the MSE_{dBsm} quantifies the difference in values. MSE_{dBsm} is also useful as seen in Figure 3-8(c) where a slight shift in one waveform still retains a relatively high correlation coefficient, but the MSE_{dBsm} value is a good indicator of the difference. Figure 3-10 plots both the MSE_{dBsm} and CC values for

3-16

the solid cylinder as it varies when compared to a shifted RCS pattern of the solid

cylinder. When the correlation coefficient is inverted and plotted, its waveform is the

same as that of the MSE_{dBsm}. Note that the CC values are plotted on an inverse scale.

The dynamic range of MSE_{dBsm} values are greater than the range of the CC values. The

conclusion is that the MSE_{dBsm} value is more sensitive to slight changes in lobe alignment

than the CC.
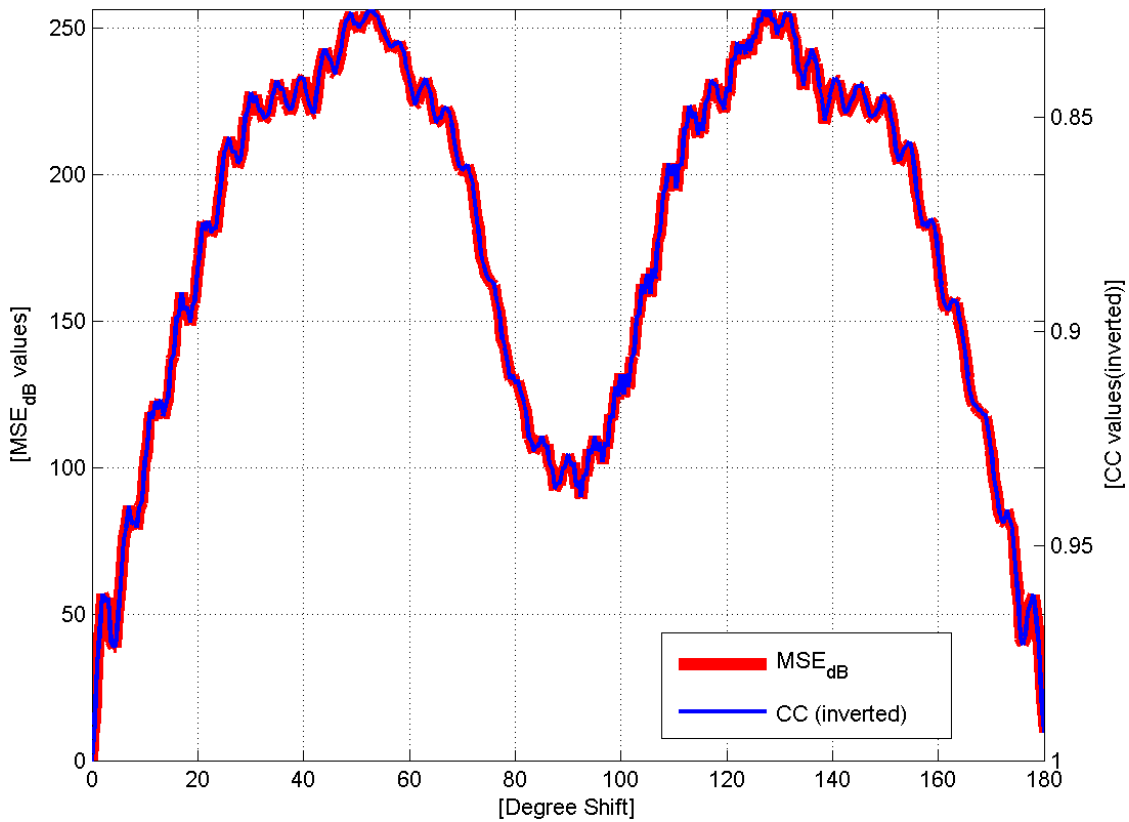
Figure 3-10: Values for MSE_{dBsm} and correlation coefficient for the closed cylinder self-compared to the same data shifted from $0° − 180°$. Note that the correlation coefficient scale is inverted.

3.6.3   Hip-pocket formulas

The following hip-pocket RCS estimation formulas from Knott [4] will also be used for

RCS analysis. These formulas can be used calculate RCS estimates and where high-

frequency scattering is assumed and polarization is not taken into account. Therefore,

use of these formulas will be qualified in each section based on the scattering regime of

the target and polarization where applicable.

Table 3-10: Hip pocket formulas for RCS estimation [4]

Approximate beam width of main beam	$\theta_{null-to-null} = 57° \dfrac{\lambda}{L}$ (3.6)
Specular Reflection	$\sigma = \dfrac{4\pi A^2}{\lambda^2}$ (3.7)
Specular Reflection Singly Curved Surface	$ka\ell^2$ (3.8)
Peak of traveling lobes	$\phi = 49° \sqrt{\dfrac{\lambda}{L}}$ (3.9)

3.7   RCS pattern convergence

A converged RCS solution is defined   solution reached by a MoM code as target

discretization is increased until the point that there is no significant change the RCS

output. Convergence will be demonstrated for the cylinder. For the sake of brevity,

converged results are used for analysis of the remaining targets in Sections 4.2 – 4.4,

without explicitly showing convergence. Equation Chapter 4 Section 1

4   Results

This chapter contains the results and analysis of CARLOS-3D, CARLOS-BOR, FISC and SAF RCS predictions for all the targets described in Chapter 3. Sections 4.1–4.4 discuss the RCS results for each target geometry. The parameters for each RCS prediction are identified by a trace reference and followed by analysis of the measured and predicted RCS results. In Section 4.1 convergence will be demonstrated for the cylinder. For the remaining targets in Sections 4.2 – 4.4, converged results are used for analysis without explicitly showing convergence. Section 4.5 investigates the range profile and lobing structure of the missile model. Sections 4.6 and 4.7 examine FISC RCS predictions using IBCs with comparison to measured data. Lastly, Section 4.8 evaluates performance of SAF, CARLOS-3D and FISC in terms of CPU time and memory requirements.

4.1   Missile upper cylinder

The cylinder is a canonical shape for which closed-form solutions can be computed. As a benchmark shape it is expected that the CEM codes should have excellent agreement. This is the only shape for which RCS data was generated using SAF.

4.1.1   400, 500 MHz convergence in FISC and CARLOS-3D

Three CAD models were produced with grid densities $\lambda/10, \lambda/12, \lambda/15$. It is expected that as grid density is increased the accuracy of the solution will converge to a point where no further increase in grid density results in a change to the RCS. As expected, MSE_{dBsm} and CC values show convergence as grid density increases. Table 4-1 and Table 4-2 list RCS trace references used for the RCS plots in Figure 4-1 through Figure 4-7 .

As discretization increased from $\lambda/10 \rightarrow \lambda/15$, the RCS solutions converge to the CAD

model with the highest discretization level, at $\lambda/15$. This convergence is demonstrated

by the reduction in MSE_{dBsm} and the increase in the correlation coefficient as

discretization increases.   Figure 4-1 and Figure 4-2 show convergence for FISC at 400

and 500 MHz. Figure 4-3 and Figure 4-4 show convergence for CARLOS-3D and

CARLOS-BOR.

Table 4-1: FISC/SAF trace references for upper cylinder at 400/500 MHz

Trace reference	Discretization	Resolution	Precision
mcyl40015/50015	$\lambda/15$	1°	Medium
mcyl40010/50010	$\lambda/10$	1°	Medium
mcyl40012/50012	$\lambda/12$	1°	Medium

Table 4-2: CARLOS trace references for upper cylinder

Trace reference	Discretization	Resolution	Geometry Input
MCYLBOR400/500	$\lambda/20$	1°	BOR
MCYLC40015/50015	$\lambda/15$	1°	Facet file
MCYLC40010/50010	$\lambda/10$	1°	Facet file
MCYLC40012/50012	$\lambda/12$	1°	Facet File
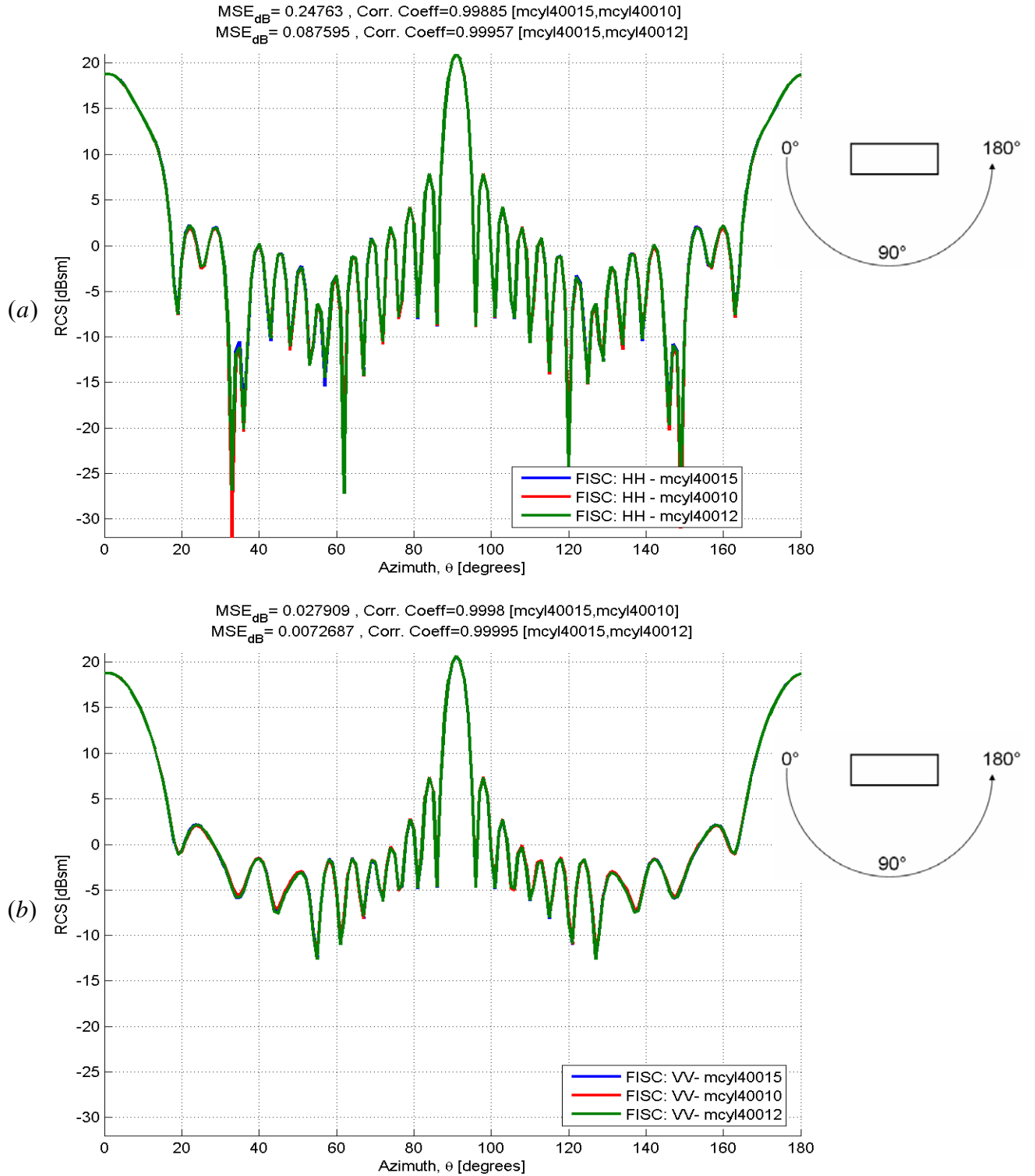
Figure 4-1: FISC RCS prediction of upper cylinder showing convergence with increasing grid densities given in a) 400 MHz HH b) 400 MHz VV. Convergence is shown by reduction MSE_{dBsm} and increase in the value of the correlation coefficient
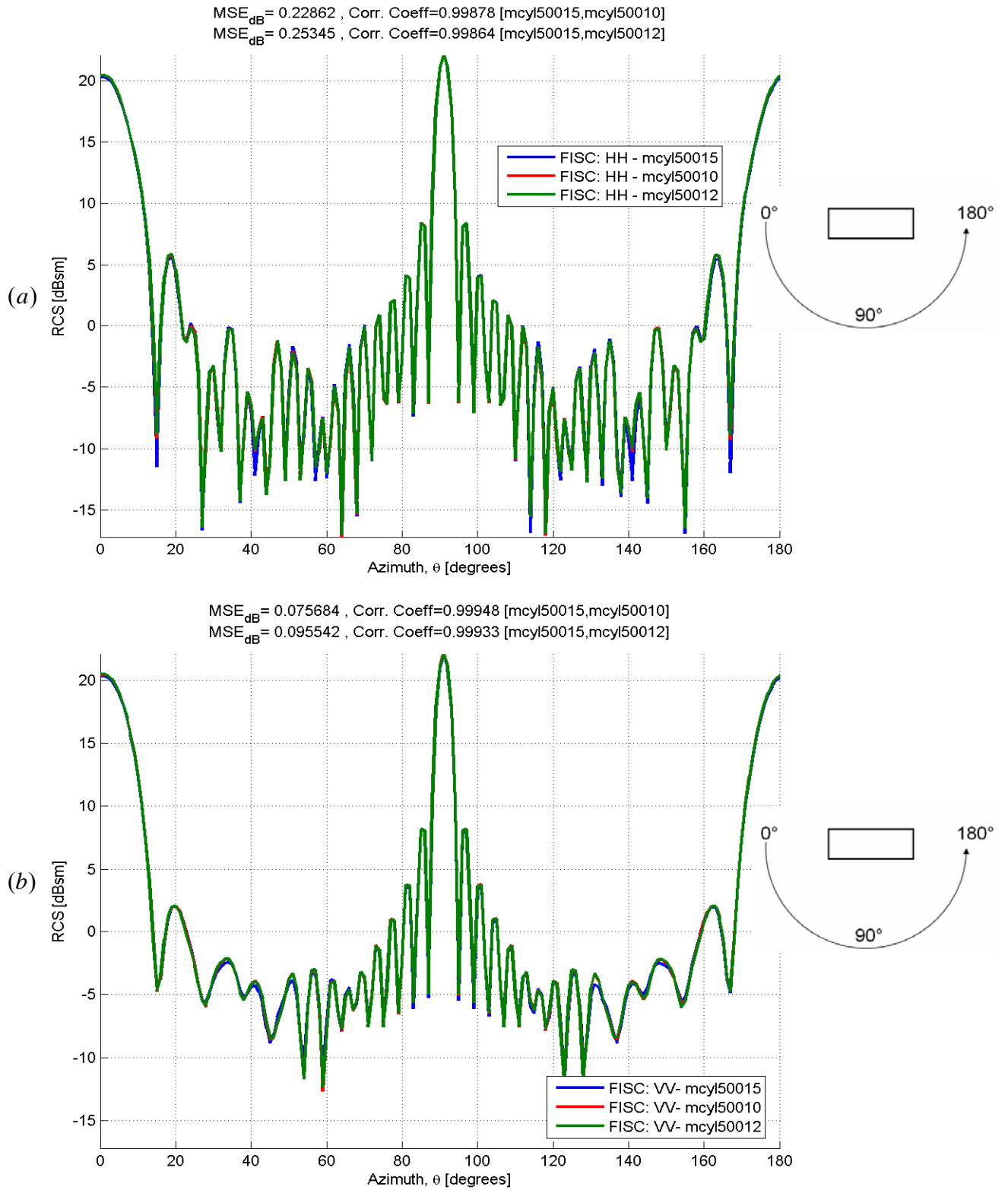
Figure 4-2: FISC RCS prediction of upper cylinder showing convergence with increasing grid densities given in a) 400 MHz HH b) 400 MHz VV. Convergence is shown by reduction in MSE_{dBsm} and increase in the value of the correlation coefficient
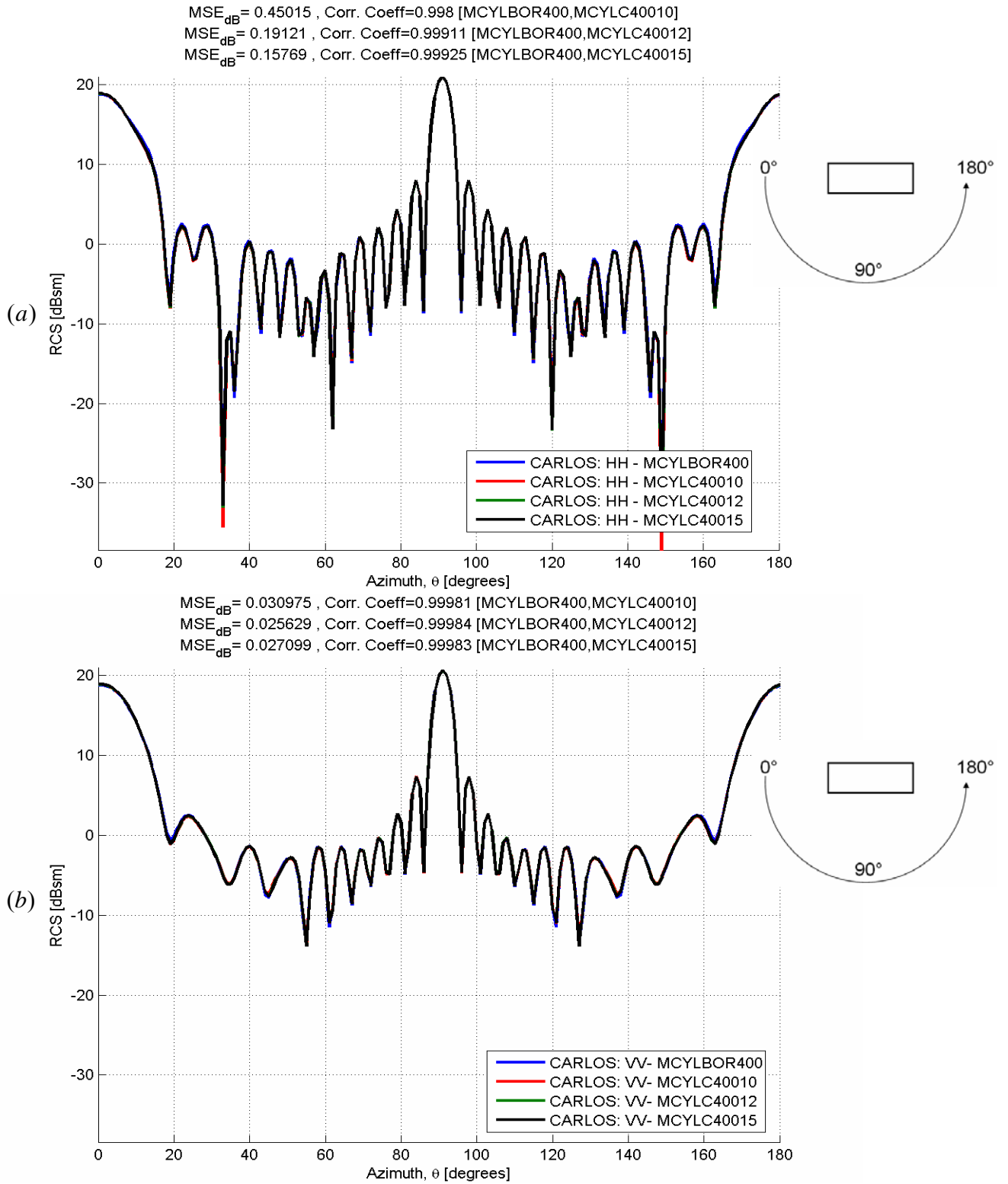
Figure 4-3: CARLOS RCS prediction of upper cylinder showing convergence with increasing grid densities given in a) 400 MHz HH b) 400 MHz VV. Convergence is shown by reduction in in MSE_{dBsm} and increase in the value of the correlation coefficient
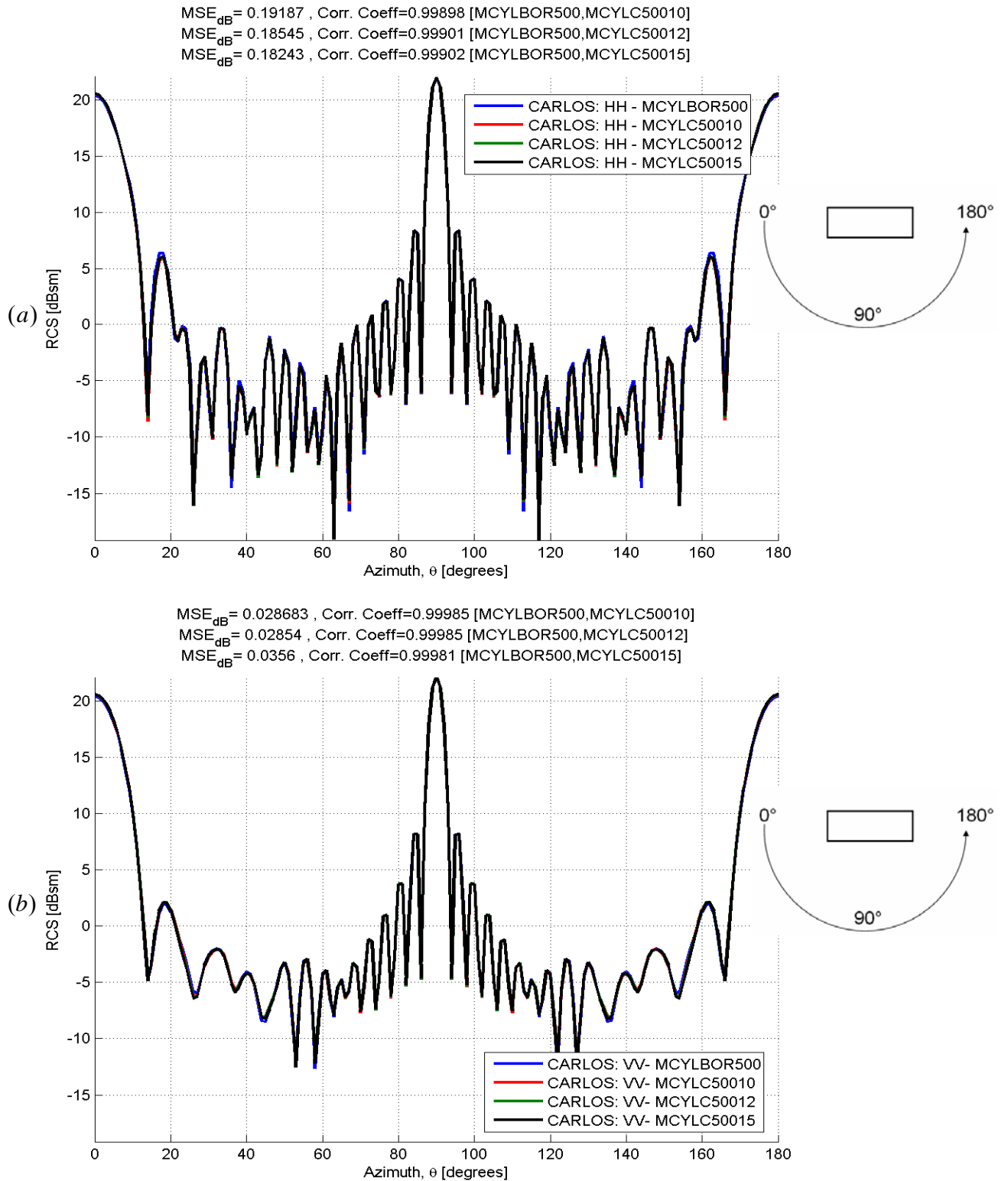
Figure 4-4: CARLOS RCS prediction of upper cylinder showing convergence with increasing grid densities given in a) 500 MHz HH b) 500 MHz VV. Convergence is shown by reduction in in MSE_{dBsm} and increase in the value of the correlation coefficient

4.1.2 400, 500 MHz Cylinder RCS results: CARLOS-3D, CARLOS-BOR, and FISC

The predicted RCS results for the cylinder from FISC, SAF, and CARLOS results were in very close agreement as seen in Figure 4-5. CARLOS-BOR was chosen as the truth solution due to its ability to model the cylinder surface with higher fidelity through the use of overlapping triangle functions which span 5 adjacent points (ie. four segments) on the generating curve. CARLOS 3-D, SAF and FISC used the same triangular facet CAD files. Table 4-3 and Table 4-4 compare hip-pocket RCS estimations to predicted and measured results for the cylinder. With respect to circumference, the closed cylinder is in the Mie region $1.0 < ka = 7.85 < 10$. However, this is the smallest physical cross-section. The maximum physical cross section is well in the optics region with a perimeter in wavelengths of 16 and 20 for 400 and 500 MHz respectively. Hip-pocket formulas [4] assume optics region and therefore yield results not far off the predicted results. There are some noteworthy conclusions that can be seen when comparing FISC and CARLOS results. First, CARLOS-BOR and CARLOS 3-D both match values for HH and VV polarization, while FISC does not. FISC yields slightly different results for VV and HH at these angles due to the nature of the iterative solver arriving at an answer than is within error bounds. CARLOS inverted the matrix and solved for the currents and therefore has an identical value for both polarizations. CARLOS-BOR with $\lambda/20$ precision at is slightly closer to the optics region at 500 MHz and matches the hip-pocket formula result exactly. Figure 4-6 and Figure 4-7 compare measured to predicted RCS for the cylinder. FISC results scored slightly better than CARLOS-BOR or CARLOS-3D results in terms of MSE_{dBsm} and CC values.
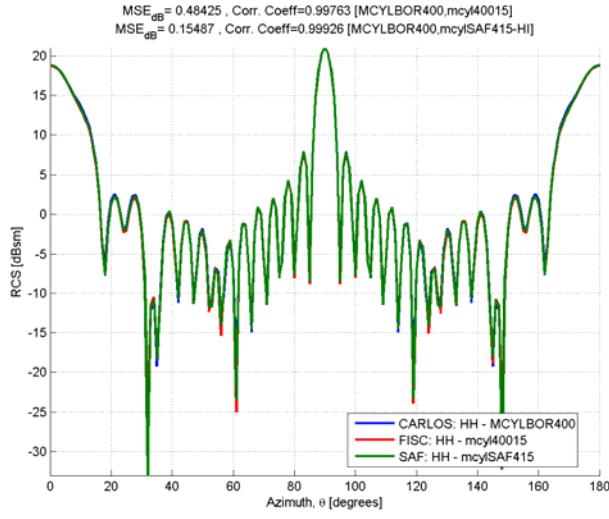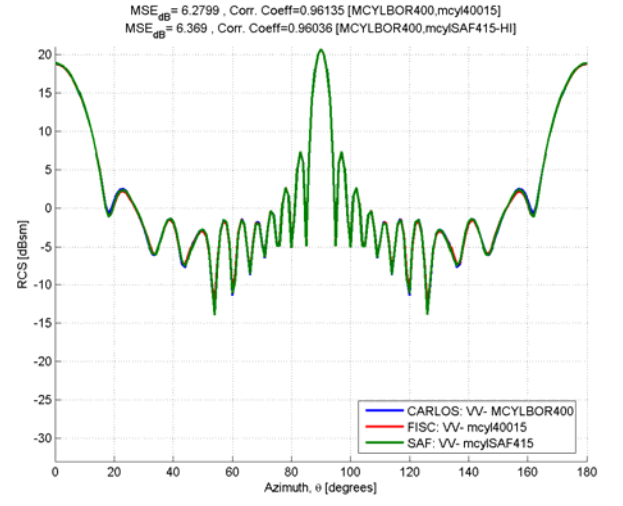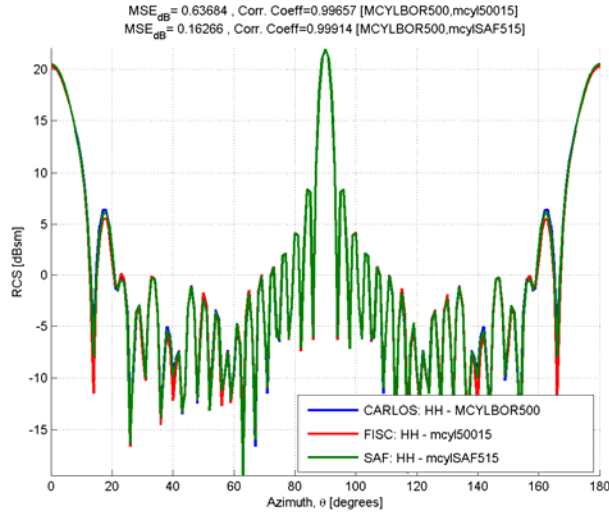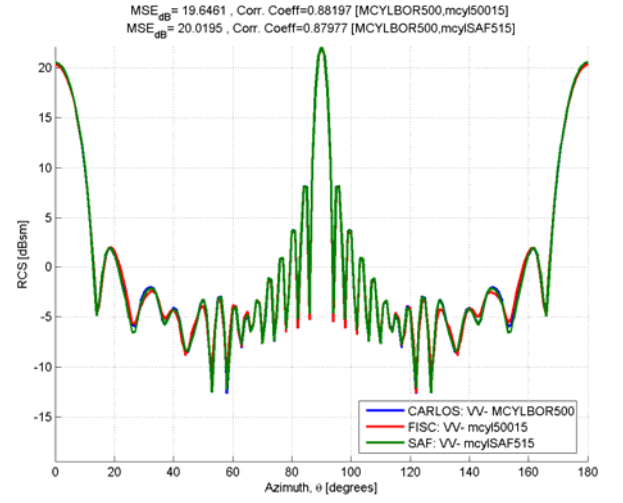
Figure 4-5: Comparison of CARLOS-BOR, FISC, and SAF predicted RCS at (a) 400 MHz HH-polarization, (b) 400 MHz VV-polarization, c) 500 MHz HH-polarization, d) 500 MHz VV-polarization
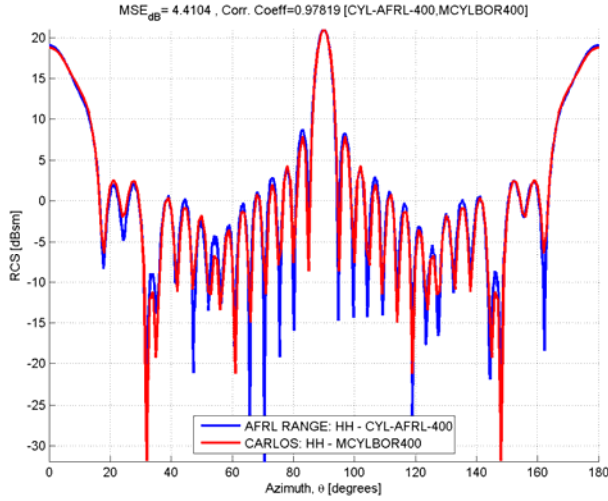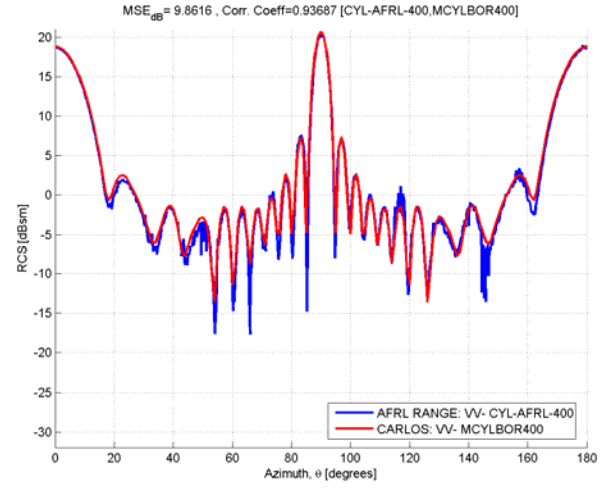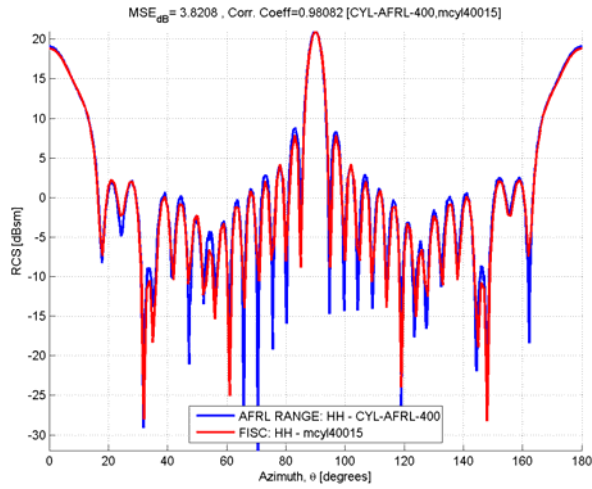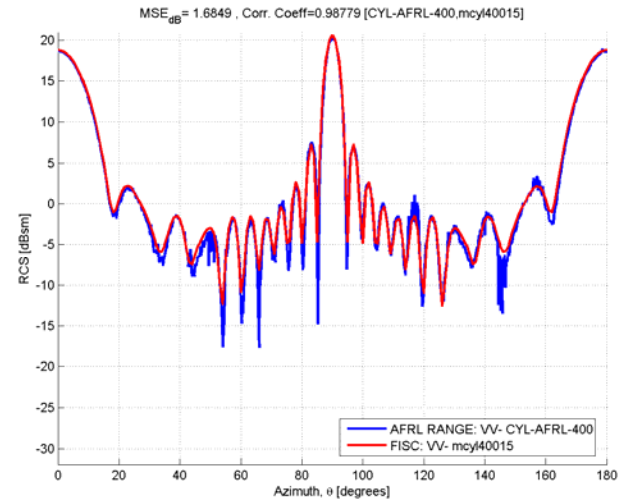
Figure 4-6: Measured versus predicted RCS at 400 MHz for a) CARLOS-BOR HH-polarization, b) CARLOS BOR VV-polarization, c) FISC HH-polarization, d) FISC VV-polarization.
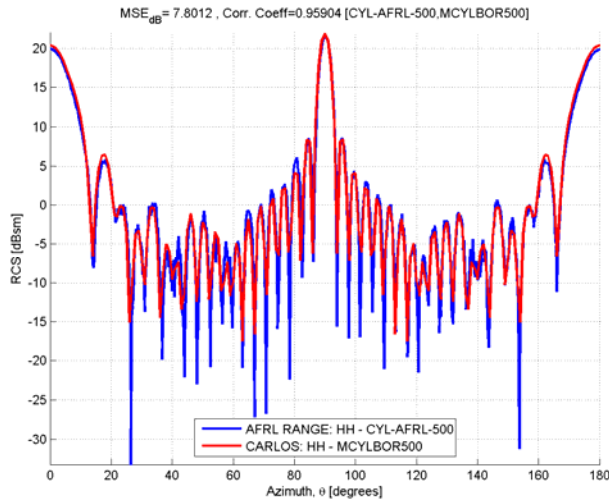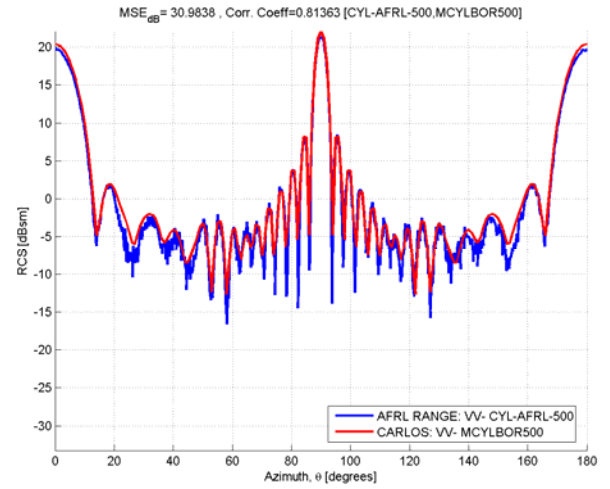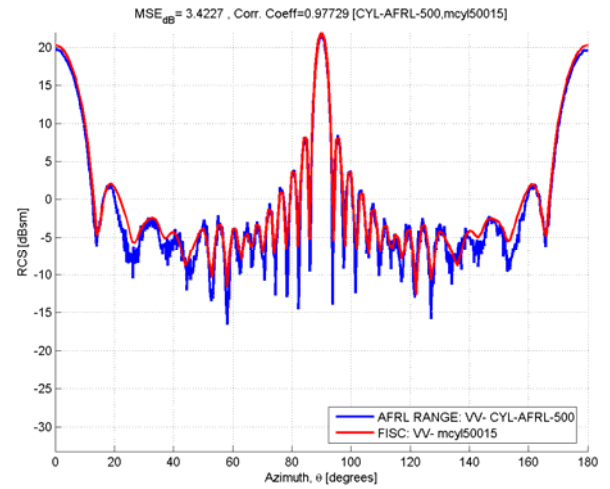
Figure 4-7: Measured versus predicted RCS at 500 MHz for a) CARLOS-BOR HH-polarization, b) CARLOS BOR VV-polarization, c) FISC HH-polarization, d) FISC VV-polarization.

Table 4-3: 400 MHz cylinder RCS results

Measurement	Formula	Formula result	FISC	CARLOS-BOR/ CARLOS 3D
Approximate beam width of main beam	$\theta_{null-to-null} = 57^\circ \dfrac{\lambda}{L}$	9.5°	10°	10°
Specular Reflection Singly Curved Surface	$ka\ell^2$	19.79 dBsm	20.96 dBsm HH 20.63 dBsm VV	21.02 dBsm HH 20.67 dBsm VV 21.01 dBsm HH 20.67 dBsm VV
Location of peak of traveling lobes	$\theta = 49^\circ \sqrt{\dfrac{\lambda}{L}}$	20°	17.5° HH	17.5° HH 17.5° HH
Specular reflection end-caps	$\sigma = 4\pi \dfrac{A^2}{\lambda^2}$	18.43 dBsm	18.79 dBsm HH 18.8 dBsm VV	18.78 dBsm HH 18.78 dBsm VV 18.89 dBsm HH 18.89 dBsm HH

Table 4-4: 500 MHz cylinder RCS results

Measurement	Formula	Formula result	FISC	CARLOS-BOR/ CARLOS 3D
Approximate beam width of main beam	$\theta_{null-to-null} = 57^\circ \dfrac{\lambda}{L}$	7.6°	8°	8°
Specular Reflection Singly Curved Surface	$ka\ell^2$	19.79 dBsm	21.98 dBsm HH 21.95 dBsm VV	21.95 dBsm HH 22.08 dBsm VV 21.97 dBsm HH 22.06 dBsm VV
Location of peak of traveling lobes	$\theta = 49^\circ \sqrt{\dfrac{\lambda}{L}}$	17.89°	17.5° HH	17.5° HH 17.5° HH
Specular reflection end-caps	$\sigma = 4\pi \dfrac{A^2}{\lambda^2}$	20.37 dBsm	20.27 dBsm HH 20.28 dBsm VV	20.37 dBsm HH 20.37 dBsm VV 20.54 dBsm HH 20.54 dBsm VV

4.2   Missile nose RCS comparison & analysis, 400, 500 MHz

CARLOS-BOR and CARLOS-3D solutions, Figure 4-8 and Figure 4-9, compared very

closely with a low MSE_{dBsm} score and a high CC value. The rear of the nose cone has a

crisp edge discontinuity which yields a large flash of diffracted energy. A cylindrical

wave from this edge radiates and results in maximum constructive interference at nose-on incidence. The nose-cone is a right circular cone whose sides make an angle of 63.43° to the base. As expected a specular flash is seen in the RCS signature at that angle. The values calculated below for the specular reflection from the singly-curved surface are for an average radius. Table 4-6 and Table 4-7 compare hip-pocket RCS estimations to measured and predicted results for the nose cone. With respect to circumference of the flat-back face, the nose cone is in the Mie region $1.0 < ka = 6.28, 7.85 < 10$ respectively for 400 and 500 MHz. Therefore the optics-based hip-pocket estimations are expected to differ from the actual values. As expected, HH values for the specular reflection from the singly-curved surface are higher than for the VV polarization since the electric field must go to zero at once along the entire length of the side for a horizontally-polarized incident wave. CARLOS-3D, CARLOS-BOR, and FISC all agree well with each other and measured results. In the measured data, much oscillation can be seen where none should be present. The AFRL measurement range noted that these values are due to a receiver malfunction. Figure 4-8 and Figure 4-9 show that RCS results using facet files with CARLOS-3D compare very well with a BOR geometry results. Figure 4-10 and Figure 4-11 compare measured to predicted RCS for the nose cone. FISC results score slightly better than CARLOS-BOR or CARLOS-3D results in terms of MSE_{dBsm} and CC values.

Table 4-5: FISC, CARLOS-3D, CARLOS-BOR trace references, nose cone target

Trace reference	Discretization	Resolution	Geometry Input
nc40015/50015	$\lambda/15$	0.5°	Facet file
NCBOR400/500	$\lambda/20$	0.5°	BOR
NC40015/50015	$\lambda/15$	0.5°	Facet file
NC40010/50010	$\lambda/10$	0.5°	Facet file
NC40012/50012	$\lambda/12$	0.5°	Facet File
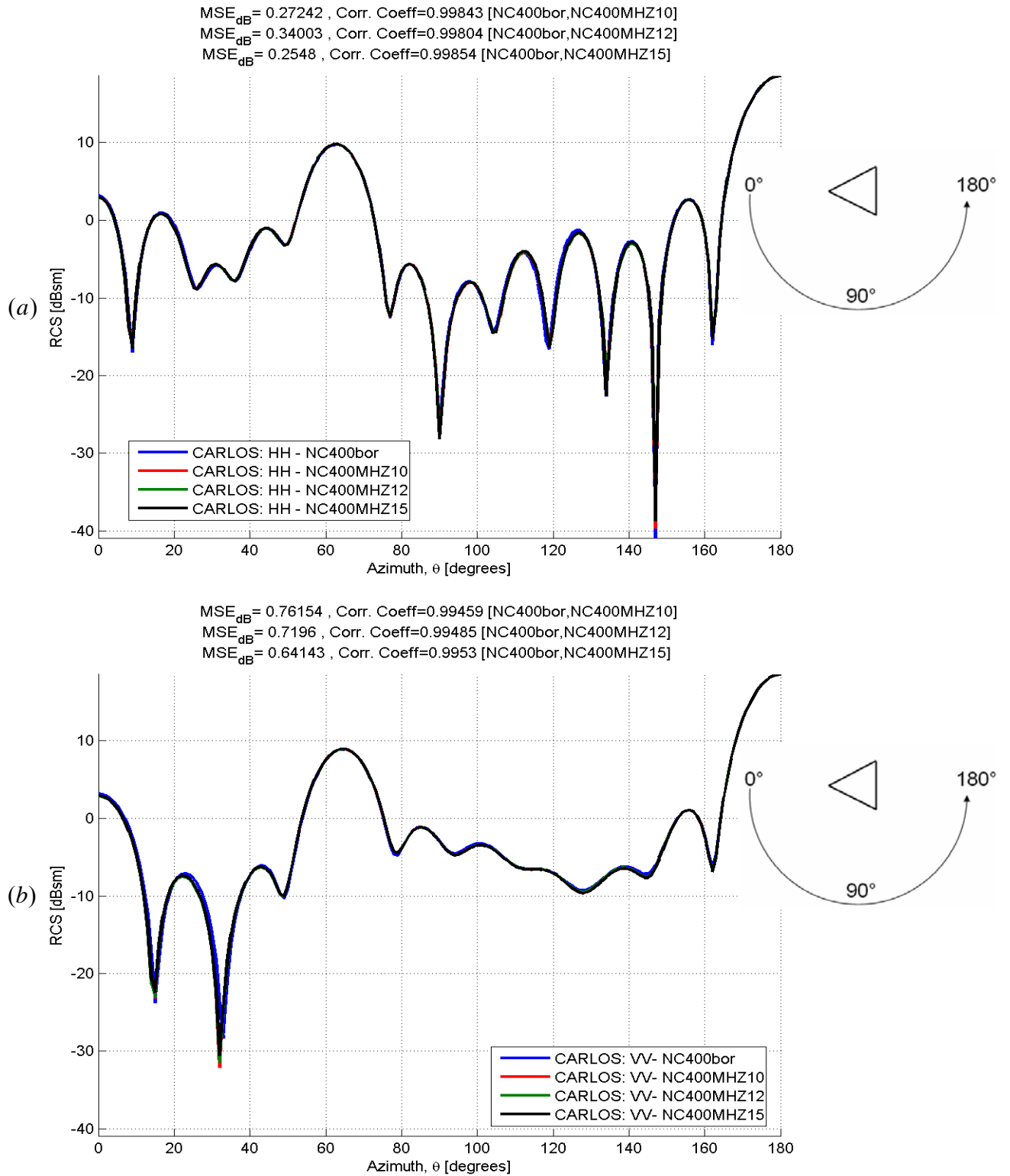
Figure 4-8: CARLOS RCS prediction of the missile nosecone showing convergence with increasing grid densities given in a) 400 MHz HH b) 400 MHz VV. Convergence is shown by reduction in MSEdBsm and increase in the value of the correlation coefficient
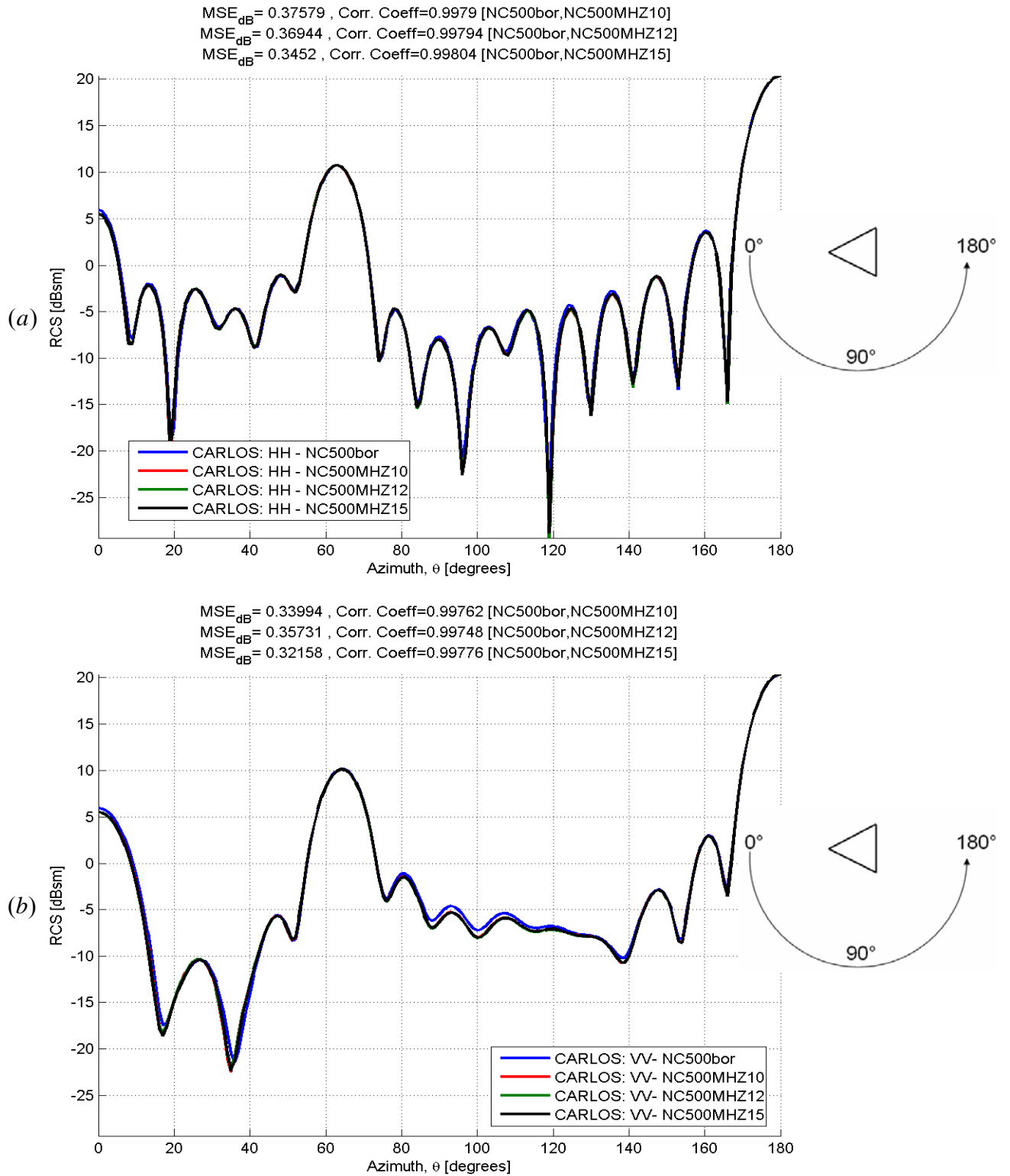
Figure 4-9: CARLOS RCS prediction of the missile nosecone showing convergence with increasing grid densities given in a) 500 MHz HH b) 500 MHz VV. Convergence is shown by reduction in MSEdBsm and increase in the value of the correlation coefficient

Table 4-6: 400 MHz nose cone RCS estimations

Measurement	Formula	Formula result	FISC	CARLOS-BOR/ CARLOS-3D
Specular Reflection Singly Curved Surface	$ka\ell^2$	12.47 dBsm	10.73dBsm HH 10.09dBsm VV	10.73 dBsm HH 10.16 dBsm VV
				10.75 dBsm HH 10.12 dBsm VV
Specular reflection flat-back	$\sigma = 4\pi \dfrac{A^2}{\lambda^2}$	18.43 dBsm	18.51 dBsm HH 18.51 dBsm VV	18.53 dBsm HH 18.53 dBsm VV
				18.53 dBsm HH 18.53 dBsm VV
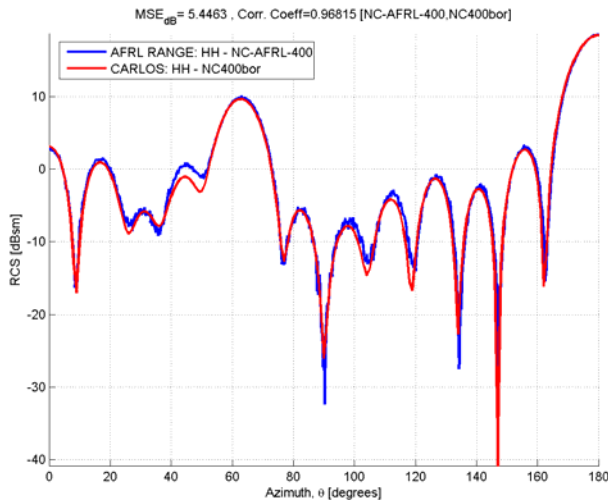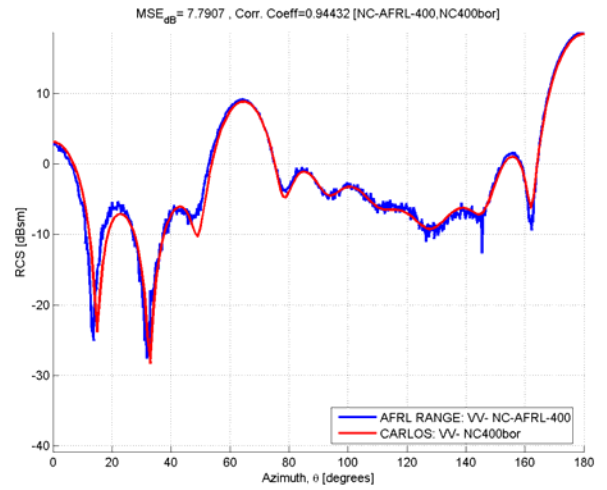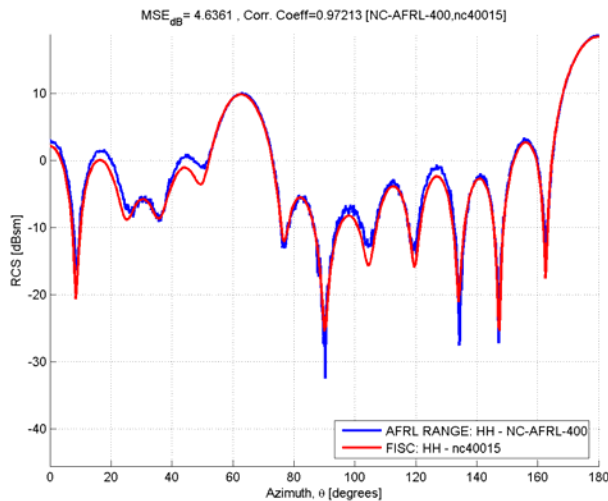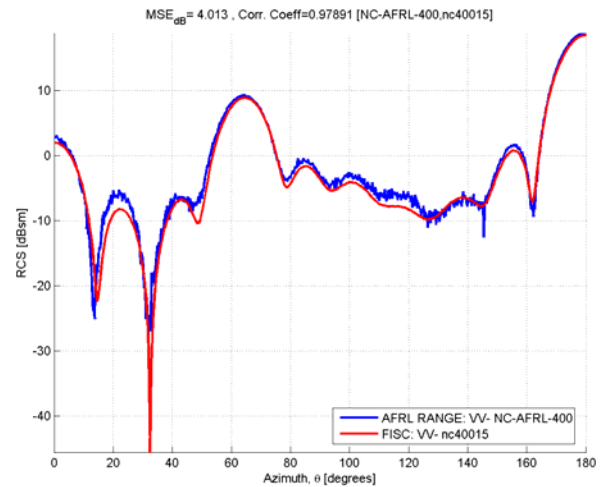
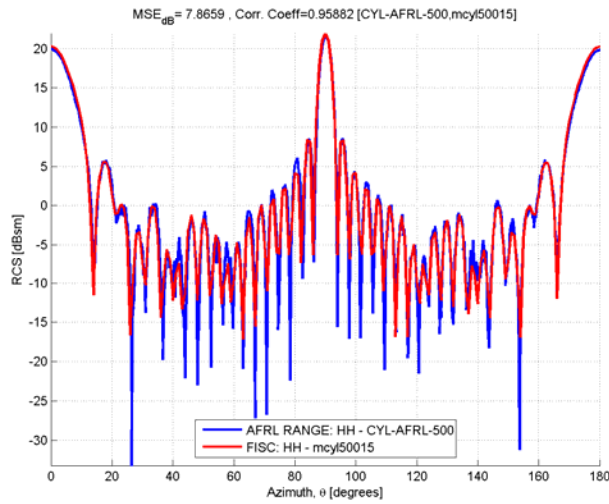Figure 4-10: Measured versus predicted RCS of the missile nose cone at 400 MHz for a) CARLOS-BOR HH-polarization, b) CARLOS BOR VV-polarization, c) FISC HH-polarization, d) FISC VV-polarization.

Table 4-7: 500 MHz nose cone RCS estimations

Measurement	Formula	Formula result	FISC	CARLOS-BOR/ CARLOS-3D
Specular Reflection Singly Curved Surface	$ka\ell^2$	11.5 dBsm	10.73dBsm HH 10.09dBsm VV	10.73 dBsm HH 10.16 dBsm VV 10.75 dBsm HH 10.12 dBsm VV
Specular reflection flat-back	$\sigma = 4\pi \dfrac{A^2}{\lambda^2}$	20.37 dBsm	20.27 dBsm HH 20.27 dBsm VV	20.31 dBsm HH 20.31 dBsm VV 20.34 dBsm HH 20.34 dBsm VV
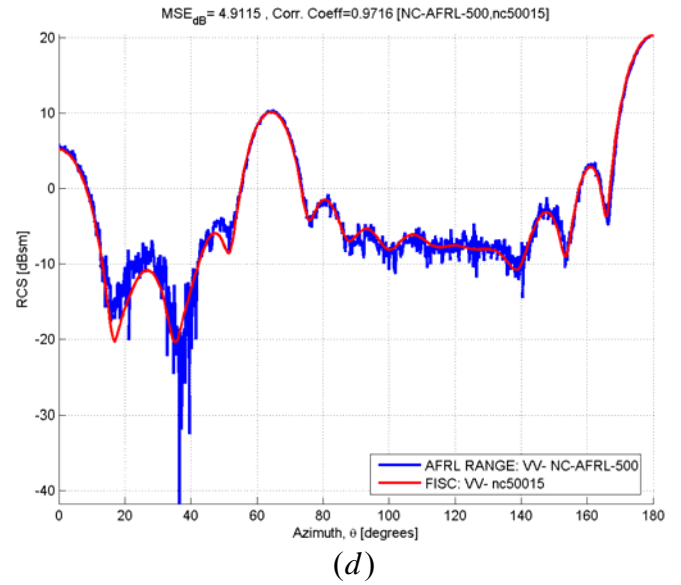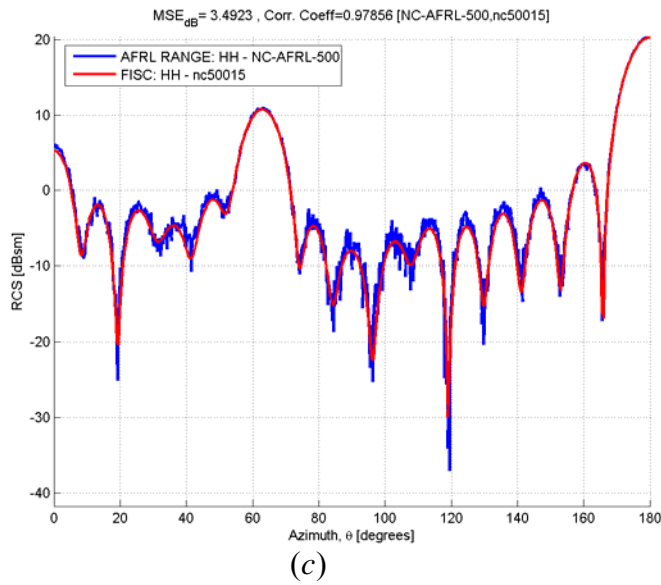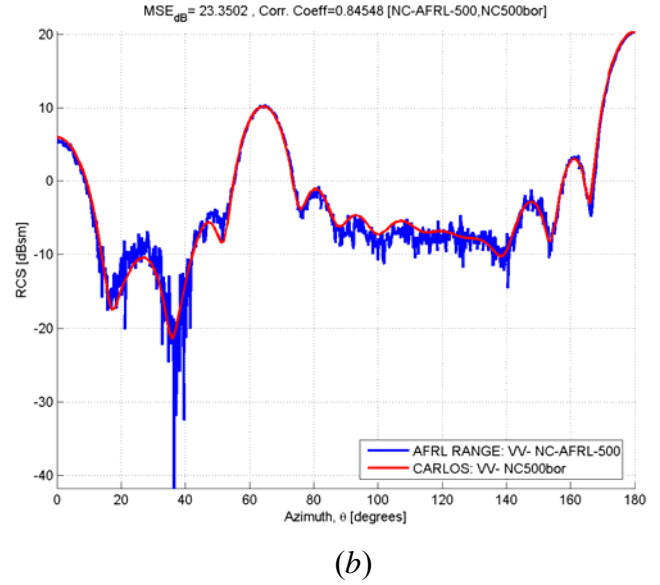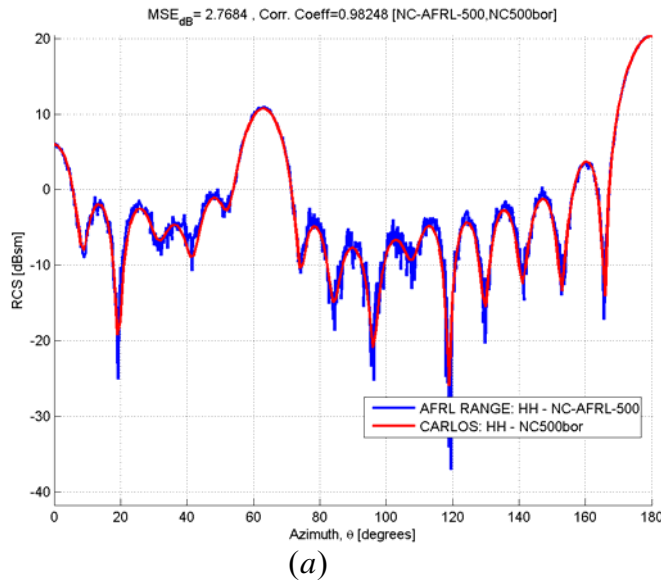
Figure 4-11: Measured versus predicted RCS of the missile nose cone at 500 MHz for a) CARLOS-BOR HH-polarization, b) CARLOS BOR VV-polarization, c) FISC HH-polarization, d) FISC VV-polarization.

4.3 Booster stage RCS: CARLOS-BOR, CARLOS-3-D, and FISC, 400, 500 MHz

The hard-coded maximum edge limit for CARLOS-3D of 70,000 edges was exceeded by the 400 MHz $\lambda/12$ discretization facet model which had 70,302 edges. Therefore, only the RCS for the 400 MHz $\lambda/10$ model having 48729 edges was predicted using CARLOS 3-D.

Table 4-8: FISC, CARLOS trace references for booster stage at 400/500 MHz

Trace reference	Discretization	Resolution	Geometry Input
bstr40015	$\lambda/15$	1°	Facet file
BSTR-C-40010	$\lambda/10$	1°	Facet file
BBOR400	$\lambda/20$	1°	BOR
BBOR400-8	$\lambda/90$	1°	BOR

The measured data for the cavity aspect does not match the predicted data because the depth of the cavity is drilled 0.82 inches shorter than is specified in Figure 3-1. Table 4-9 and Table 4-10 compare hip-pocket RCS estimations to measured and predicted results for the booster stage. The 0˚ aspect presents a slightly larger physical area to the receiver than the upper cylinder. The area difference is due to the cone frustrum which provides a transition from the cylinder radius of 0.75 meters to the booster radius of 0.875 meters at an angle of 45˚. Due to the 45˚ angle, the *area* of the cone frustrum contributes little to the specular RCS value of the end-cap. This is an excellent example of how shaping affects RCS; despite the increased physical area there is no increase to the RCS from this increased physical area. Therefore, the booster RCS values for the end-cap of the booster, upper cylinder, and nosecone are nearly the same for this aspect. The slight RCS differences (0.4/0.7 dBsm for 400/500 MHz respectively) when compared to values for the cylinder at the same aspect is due to each object having different edge

Table 4-9: 400 MHz booster stage RCS estimations

Measurement	Formula	Formula result	FISC	CARLOS
Approximate beam width of main beam	$\theta_{null-to-null} = 57° \dfrac{\lambda}{L}$	3.63°	4°	4°
Specular Reflection Singly Curved Surface	$ka\ell^2$	29.47 dBsm	29.47dBsm HH 28.72dBsmVV	29.48dBsmHH 28.76dBsmVV
Specular reflection end-cap	$\sigma = 4\pi \dfrac{A^2}{\lambda^2}$	18.43 dBsm	18.41 dBsm HH 18.45 dBsm VV	18.57 dBsm HH 18.57 dBsm VV
RCS at 180˚, cavity aspect	-	-	15.13 dBsm HH 15.34 dBsm VV	16.55 dBsm HH 16.55 dBsm VV
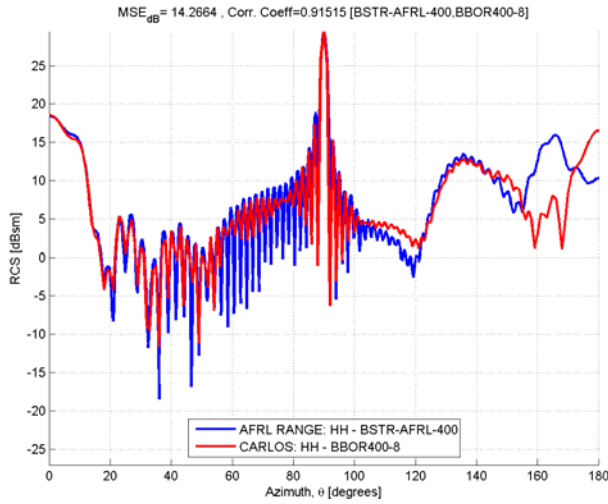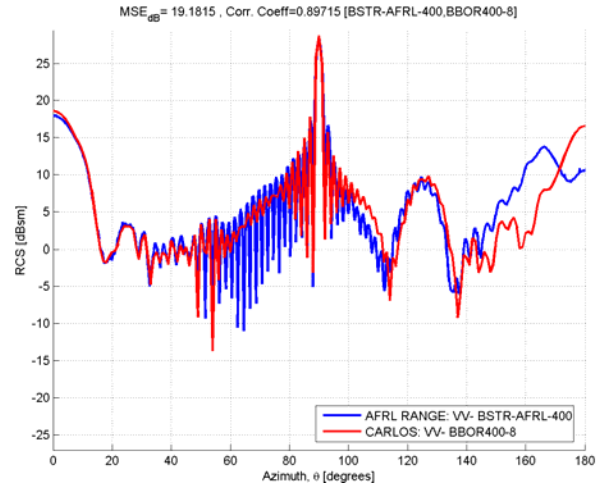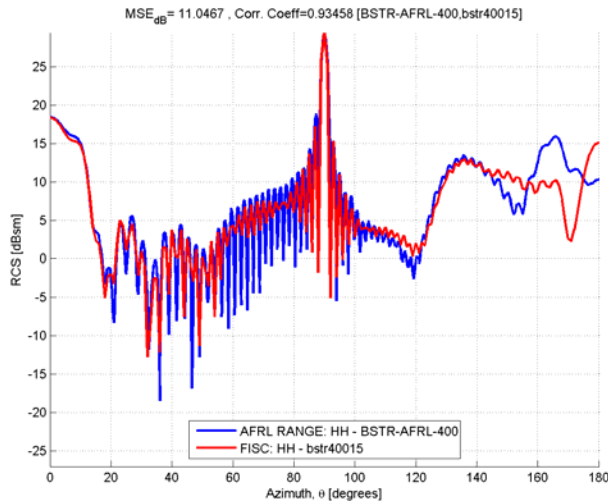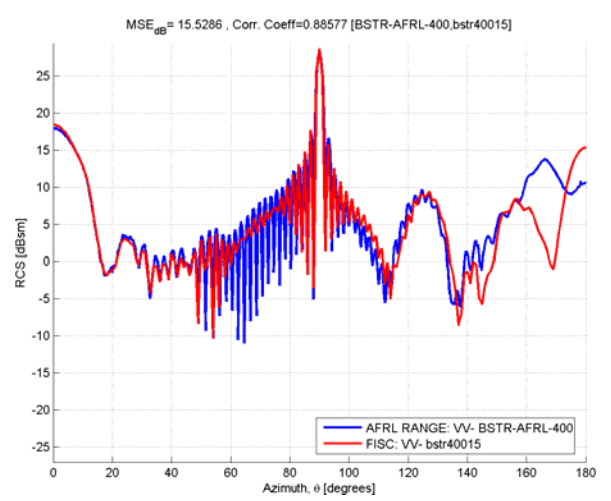
Figure 4-12: Measured versus predicted RCS of the missile nose cone at 400 MHz for a) CARLOS-BOR HH-polarization, b) CARLOS BOR VV-polarization, c) FISC HH-polarization, d) FISC VV-polarization.

Table 4-10: 500 MHz booster stage RCS estimations

Measurement	Formula	Formula result	FISC	CARLOS
Approximate beam width of main beam	$\theta_{null-to-null} = 57° \dfrac{\lambda}{L}$	3.1°	3°	3°
Specular Reflection Singly Curved Surface	$ka\ell^2$	30.448 dBsm	30.67dBsm HH 30.59 dBsm VV	30.67 dBsm HH 30.64 dBsmVV
Specular reflection end-cap	$\sigma = 4\pi \dfrac{A^2}{\lambda^2}$	20.37 dBsm	20.98 dBsm HH 20.84 dBsm VV	20.98 dBsm HH 20.84 dBsm VV
RCS at 180˚, cavity aspect	-	-	12.71 dBsm HH 12.77 dBsm VV	13.83 dBsm HH 13.83 dBsm VV
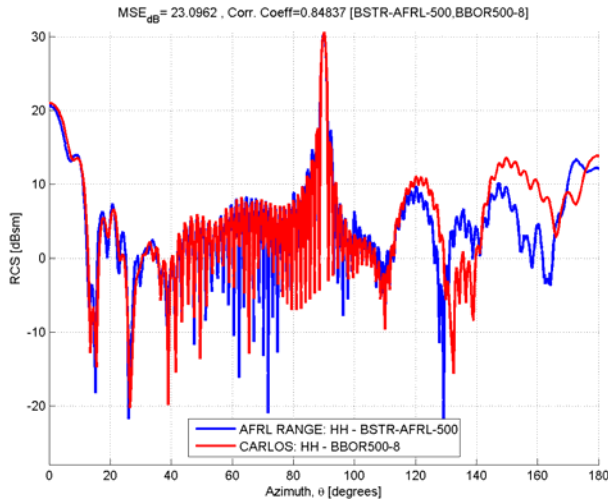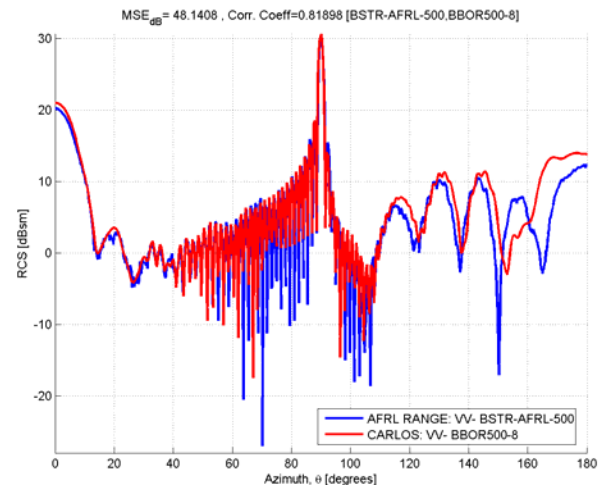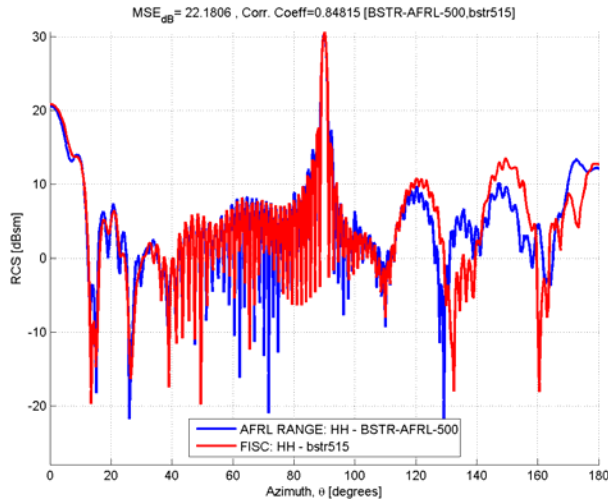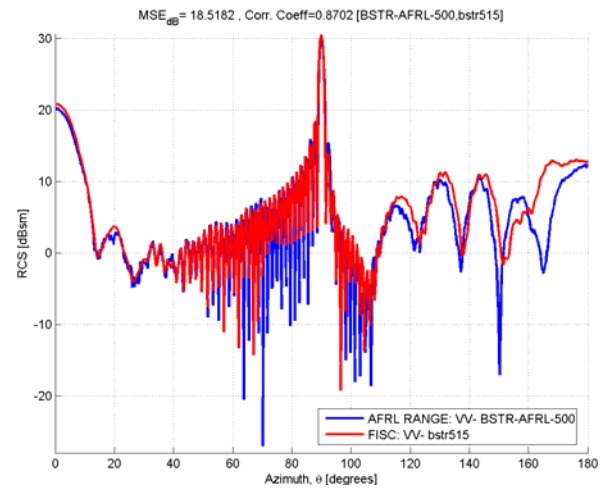
Figure 4-13: Measured versus predicted RCS of the missile nose cone at 500 MHz for a) CARLOS-BOR HH-polarization, b) CARLOS BOR VV-polarization, c) FISC HH-polarization, d) FISC VV-polarization.

discontinuities further along the body when encountered by the incident field at 0˚. The RCS of the booster stage at the 0˚ and 180˚aspects (end-cap or cavity aspects), should yield identical values for VV and HH polarizations since the geometry is the same with respect to the electric field for either polarization. FISC yields slightly different results for VV and HH at these angles due to the nature of the iterative solver arriving at an answer than is within error bounds. CARLOS solves for the currents and therefore has an identical value for both polarizations.

4.4   Missile RCS Comparisons

Convergence is shown in Figure 4-15 and Figure 4-16 to examine predicted RCS differences when using FISC's option for medium or high precision. The precision option affects the number of Gaussian integration points, modes used in MLFMA and the final residue error in the iterative method. FISC automatically sets these levels based on the choice of precision. Table 4-11 lists RCS pattern traces references.

4.4.1   400, 500 MHz convergence in FISC

As discretization increased from $\lambda/10 \rightarrow \lambda/15$, shown in Figure 4-15, the RCS solutions converge to the high precision solution at $\lambda/15$, hsg415 trace. Note the reduction in MSE_{dBsm} and the increase in the correlation coefficient when compared to the high precision hsg415 result.

Table 4-11: 400/500 MHz missile FISC trace references

Trace reference	Discretization	Resolution	Precision
hsg415/515	$\lambda/15$	0.5°	High
msg40010/50010	$\lambda/10$	1°	Medium
msg40012/50012	$\lambda/12$	1°	Medium
msg40015	$\lambda/15$	1°	Medium

Since the full-scale model is computationally intense and requires a long solution time, lower resolution CAD models were sampled in azimuth less than Nyquist criterion specifies and also medium precision. Using equation (3.2) Nyquist criterion for the missile requires azimuth sampling to be 0.9° or less to avoid aliasing. For the VV polarization result shown in Figure 4-15, the $\lambda/12$ undersampled RCS compares better (lower MSE_{dBsm} and higher correlation coefficient) than $\lambda/15$ undersampled RCS. This seemingly illogical result is due to the fact that the properly sampled RCS must be down-sampled to compare with the lower resolution data. However, when compared to measured data, the higher resolution data scores better in MSE_{dBsm} and have a better correlation. Also, all cases sampled at Nyquist or better show that the converged, ie. higher resolution data is the most accurate. Figure 4-14 shows where lobing detail is lost when the Nyquist criterion is not met.
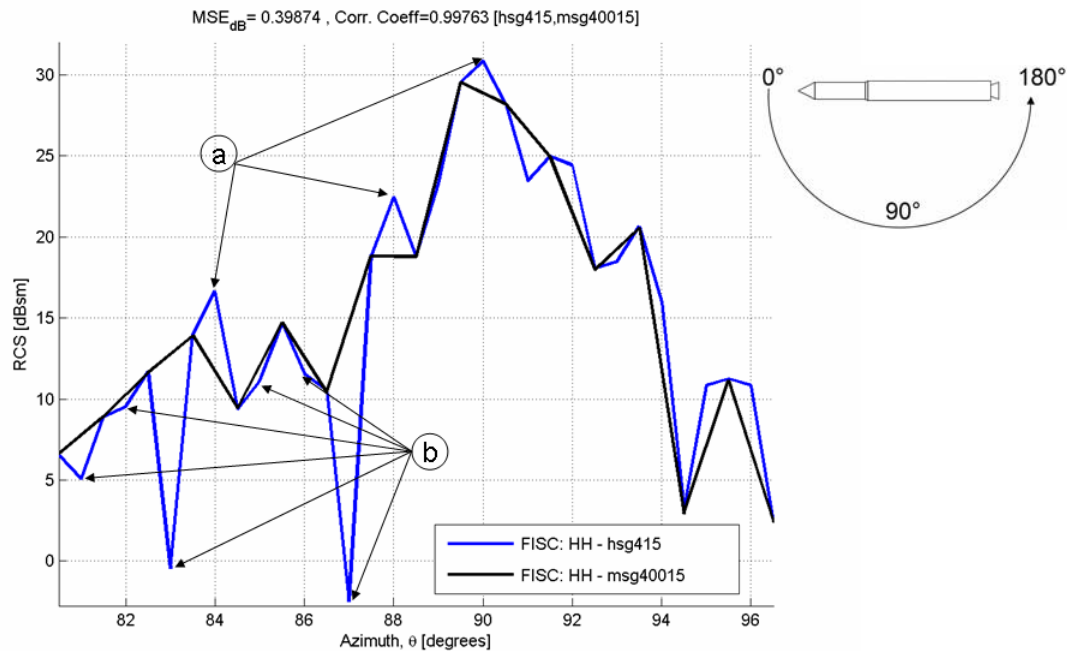
Figure 4-14: Zoom-view of Figure 4-15 showing aliasing due to undersampling. (a) shows angles with missed peaks, (b) shows angles with missed nulls
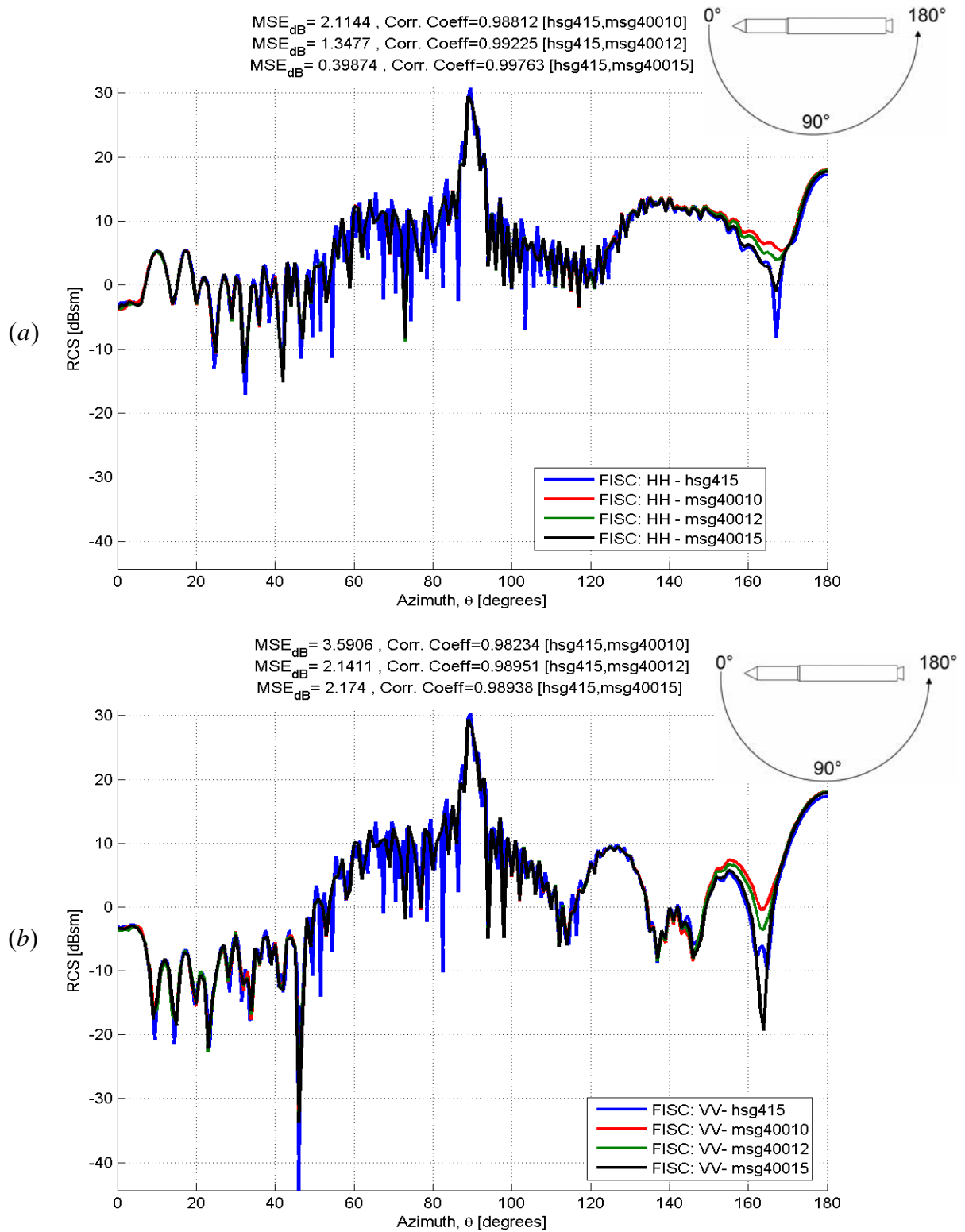
Figure 4-15: FISC RCS prediction of full-scale missile model at (a) 400 MHz, HH polarization and (b) 400 MHz, VV polarization showing convergence with increasing grid densities given in Table 4-11
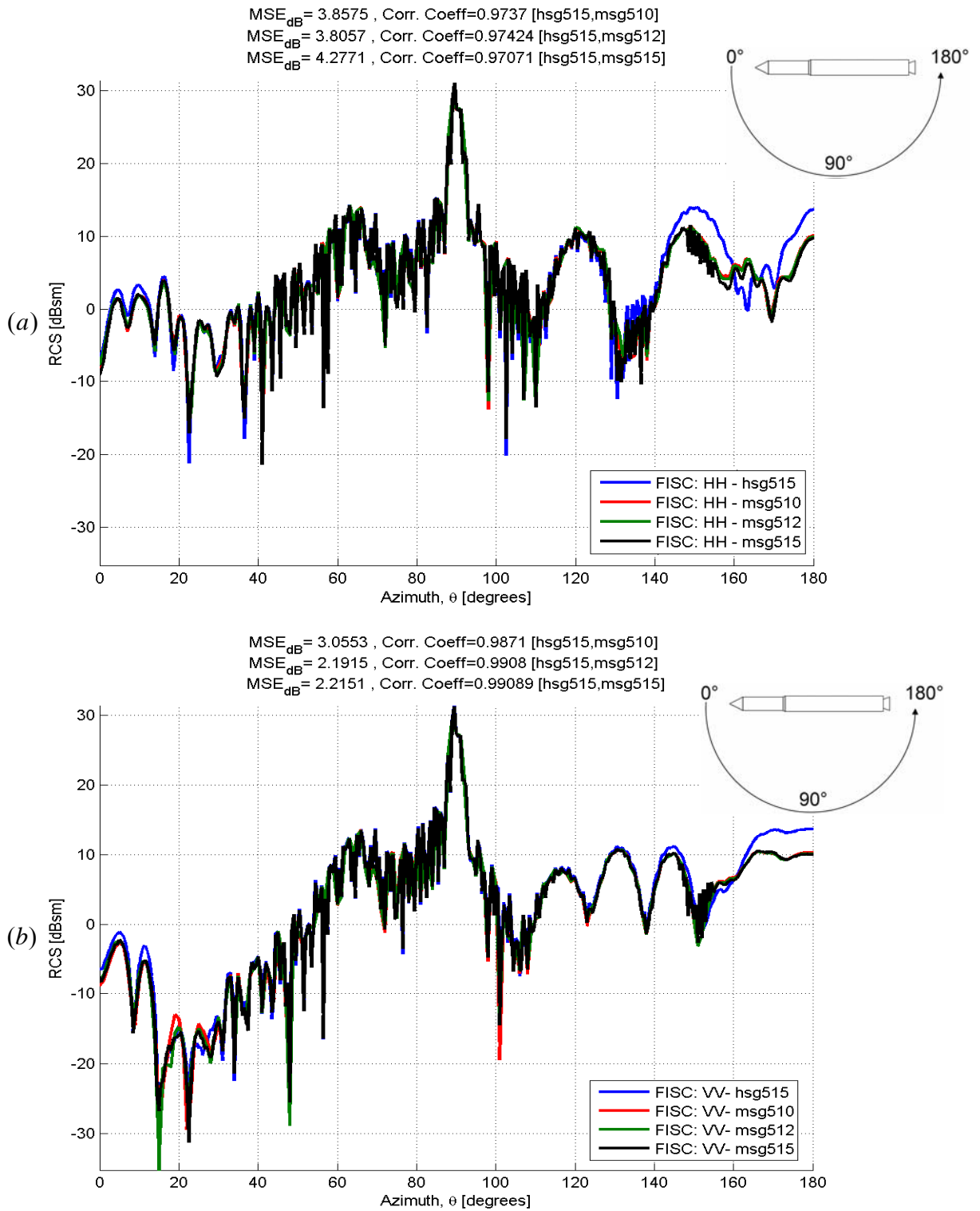
Figure 4-16: FISC RCS prediction of full-scale missile model at (a) 500 MHz, HH polarization and (b) 500 MHz, VV polarization showing convergence with increasing grid densities given in Table 4-11

4.4.2   400, 500MHz Convergence, CARLOS BOR

CARLOS BOR convergence is shown in Figure 4-17 and Figure 4-18 at 400 and 500
MHz by allowing the body of revolution segments per wavelength (BOR_SEG) range
from $\lambda/20$ (default setting) to $\lambda/90$. The solution showed convergence at $\lambda/70$ for the
missile with no significant accuracy gain when discretized to $\lambda/90$. Table 4-13 lists trace
references used for the RCS plots in Figure 4-17 and Figure 4-18.

Table 4-12: 400/500 MHz Missile CARLOS Trace references

Trace reference	Discretization	Resolution
MSBOR400-8	$\lambda/90$	0.5°
MSBOR400	$\lambda/20$	0.5°
MSBOR400-4	$\lambda/50$	0.5°
MSBOR400-6	$\lambda/70$	0.5°
MSBOR500-8	$\lambda/90$	0.5°
MSBOR500	$\lambda/20$	0.5°
MSBOR500-4	$\lambda/50$	0.5°
MSBOR500-6	$\lambda/70$	0.5°
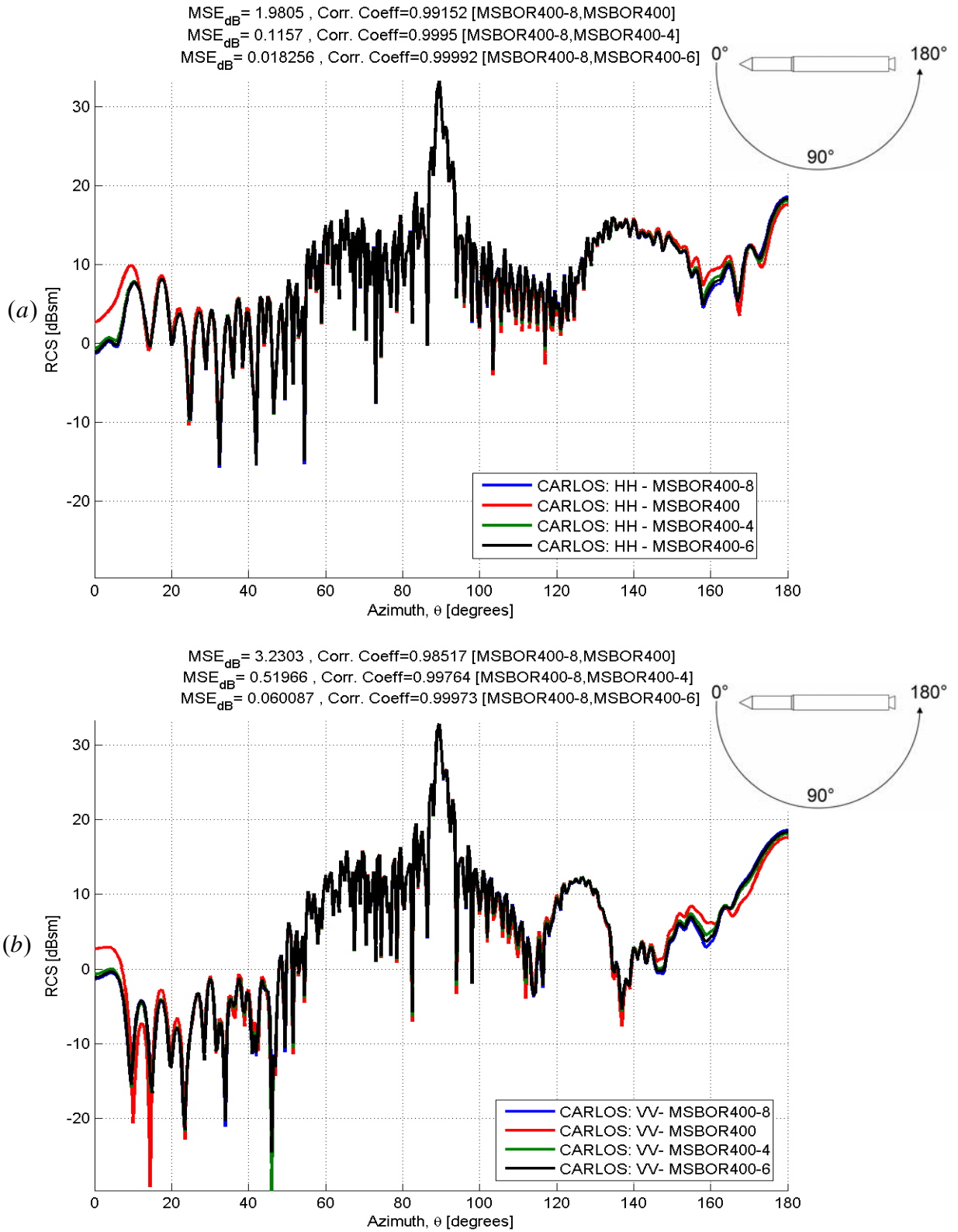
Figure 4-17: CARLOS BOR 400 MHz RCS prediction of missile model (a) HH polarization, (b) VV polarization, showing convergence, grid densities given in Table 4-12
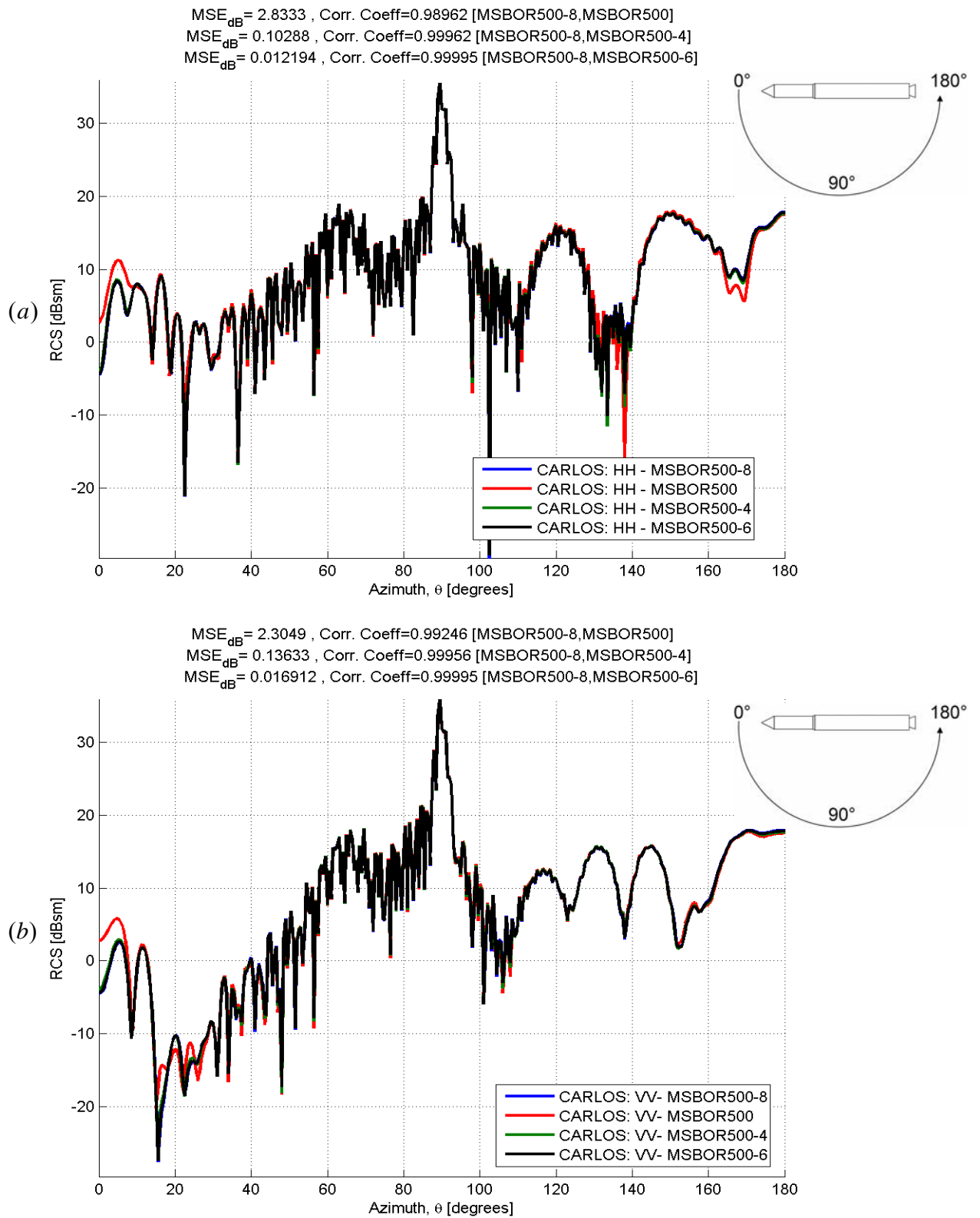
Figure 4-18: CARLOS BOR 500 MHz RCS prediction of missile model (a) HH polarization, (b) VV polarization, showing convergence, grid densities given in Table 4-12.

4.4.3 400, 500 MHz Missile RCS Comparison: CARLOS-BOR, FISC, and Measured Data

FISC and CARLOS predicted results compare least well for the cavity as seen in Figure 4-19 and Figure 4-20. FISC calculates deeper nulls than is predicted by CARLOS or seen in measured data. CARLOS scores better with respect to MSE_{dBsm} and CC values for both polarizations at 400 MHz and at 500 MHz for the VV-polarization. At 500 MHz CARLOS and FISC have better agreement with each other than the measured results. Due to this agreement of the two codes there is most likely a difference between the physical cavity and modeled cavity. Five differences between the physical and CAD models are listed in Section 3.1.1, including finite tolerance of measurements, surface roughness, and the interior angle of the cavity. The most significant difference is the rounded back wall of the cavity. An inwardly-pointed back cavity wall is a dihedral structure that creates significantly different propagation patterns within the cavity than a rounded back wall. The rounded back wall would have a specular response that would be combined with other scatterers at this aspect. For further analysis, a range profile is included in Section 4.5 to identify scatterers and their effect on lobing structure.
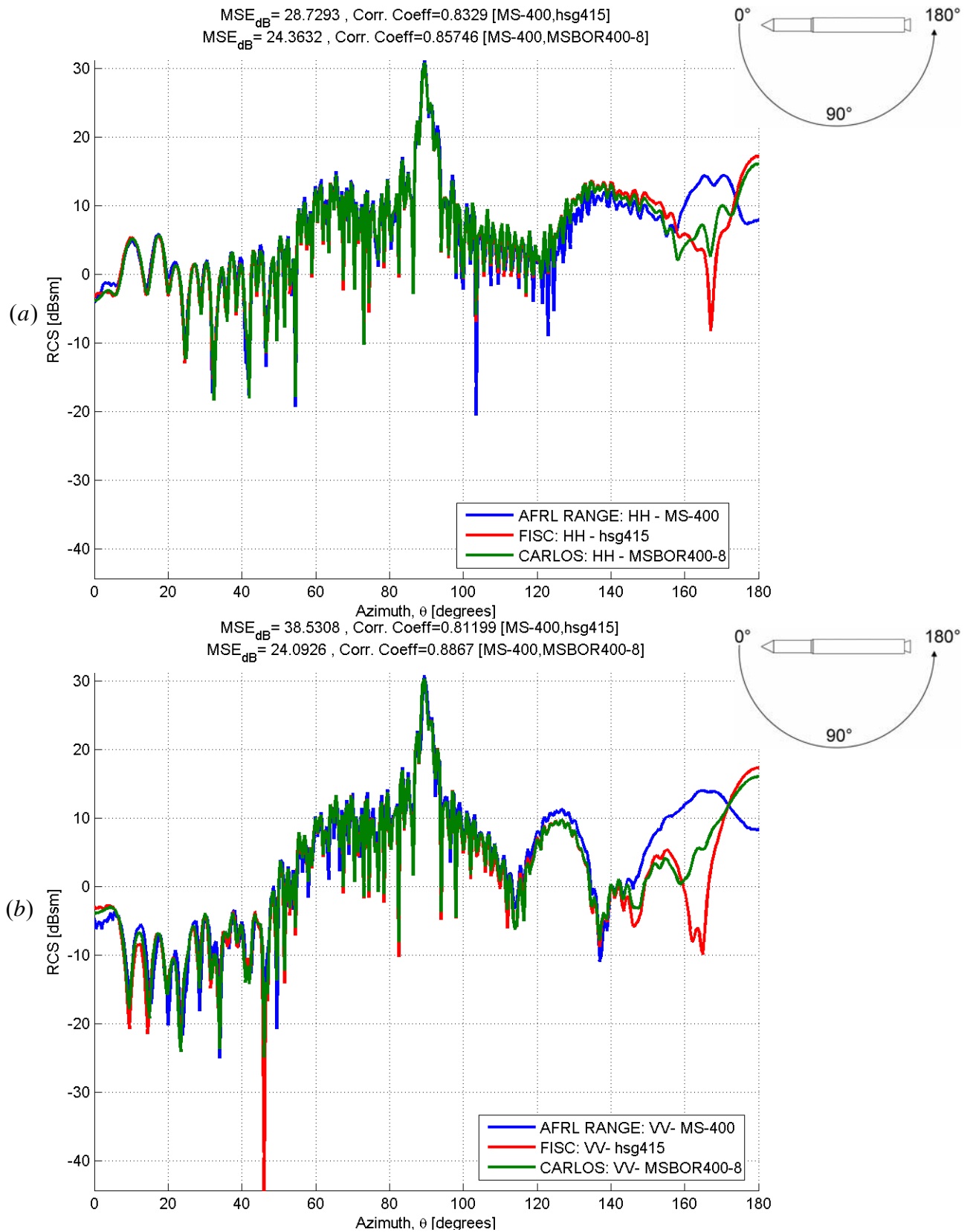
Figure 4-19: FISC and CARLOS-BOR 400 MHz comparison of full-scale missile model for (a) HH polarization (b) VV polarization
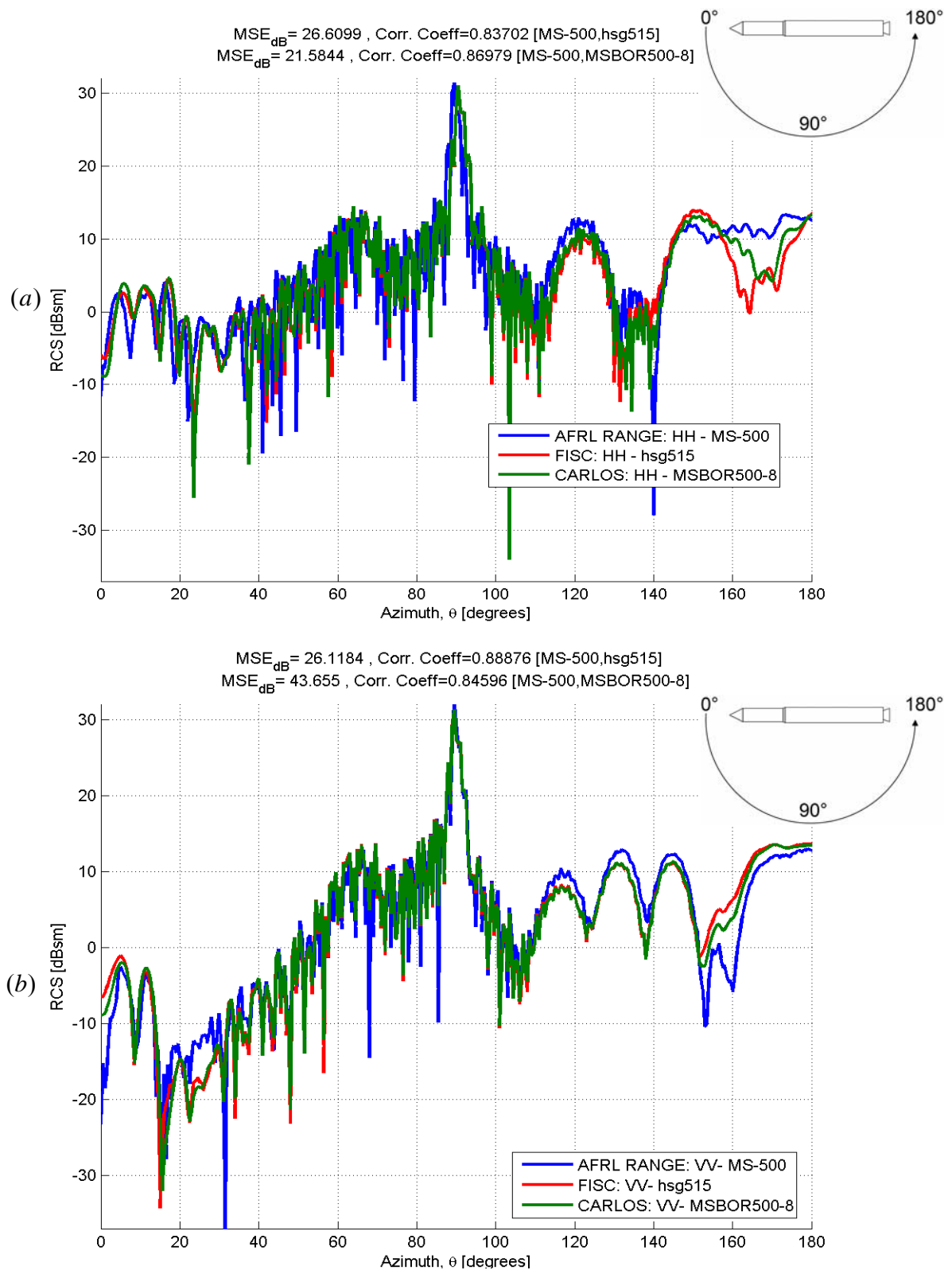
Figure 4-20: FISC and CARLOS-BOR 500 MHz comparison of full-scale missile model for (a) HH polarization (b) VV polarization

4.5 *Range profile of missile model*

Shown below are 2-D range profiles of the missile model from four aspects for HH polarization. These range profiles were chosen to highlight scatterers on the missile body. A properly-scaled missile is overlaid onto the plots to show scatterer contributions. Figure 4-21(a), shows diffraction at edge continuities at various points along the missile. Edge discontinuities are readily distinguishable at the junctions of a) nose cone to upper cylinder, b) cone frustrum between the upper missile cylinder and booster stage, c) booster stage base discontinuity, and d) exhaust nozzle rim.

By keeping the image at the exact location in range and rotating appropriately, Figure 4-21(b) shows how the magnitude of the scatterers and their locations in range change due to the rotation. Figure 4-22(a) shows that nearly all monostatic scattering at 150˚is due to the cavity and exhaust nozzle. This is not surprising since the exhaust nozzle when viewed from that angle presents a dihedral structure to the transmitter and a specular angle from the inside surface of the nozzle. Figure 4-22 (b) shows ringing from the exhaust cavity that continues to provide a response across the range profile. The lobe structure beyond the beginning of the cavity location is due to the superposition of sidelobes of the impulse response and is related to the fractional bandwidth defined in (1.1) and shown in Figure 4-23 [11]. Note, however, that Figure 4-23 does not show absolute values as is done for the range profiles and also the *x*-axis is a function of normalized time instead of distance. The parameters of the range profiles are listed in table 11. From range profiles, target scatterers of azimuth-dependent magnitudes are identified in Figure 4-24.
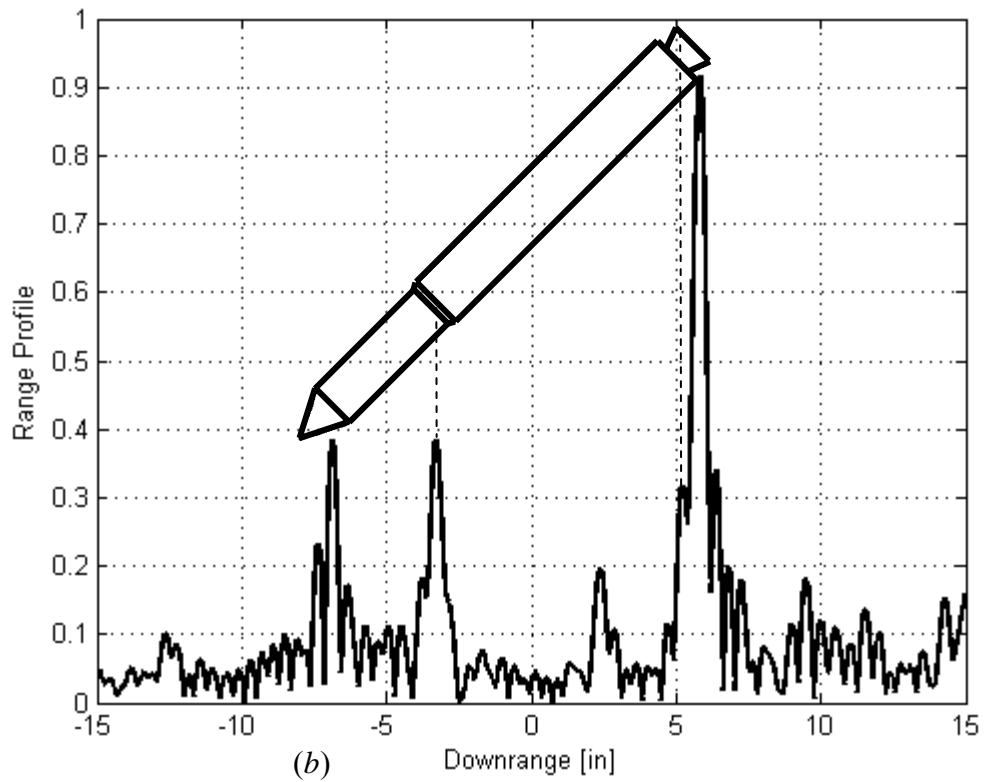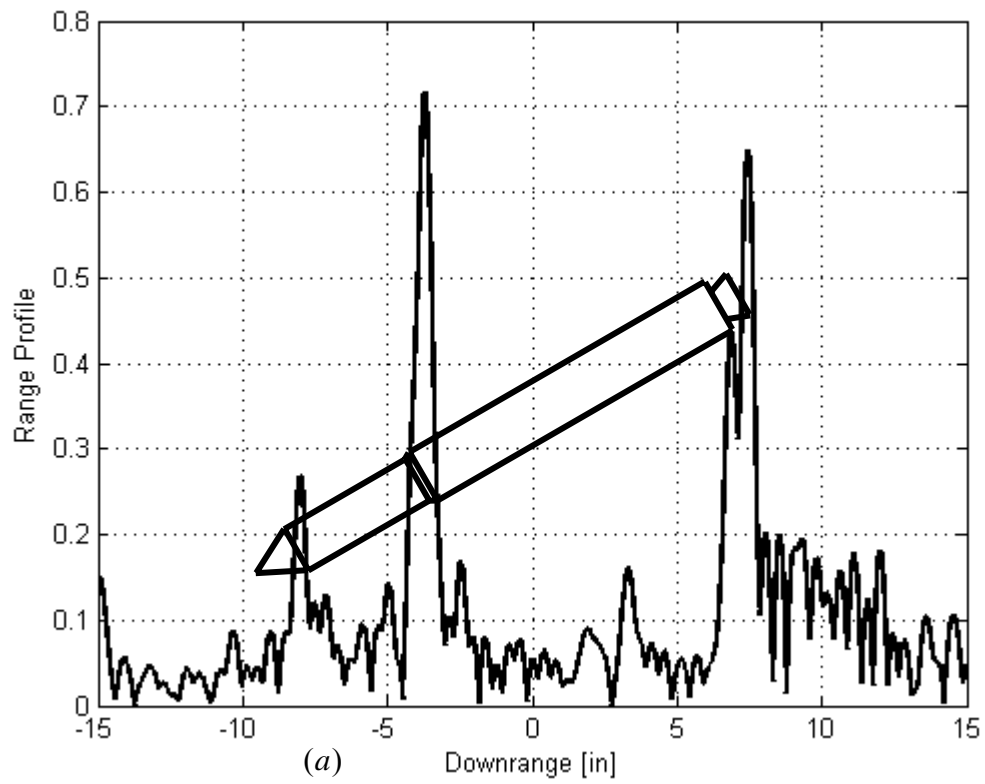
Figure 4-21: Missile model impulse response at (a) 30° and (b) 45°, HH polarization
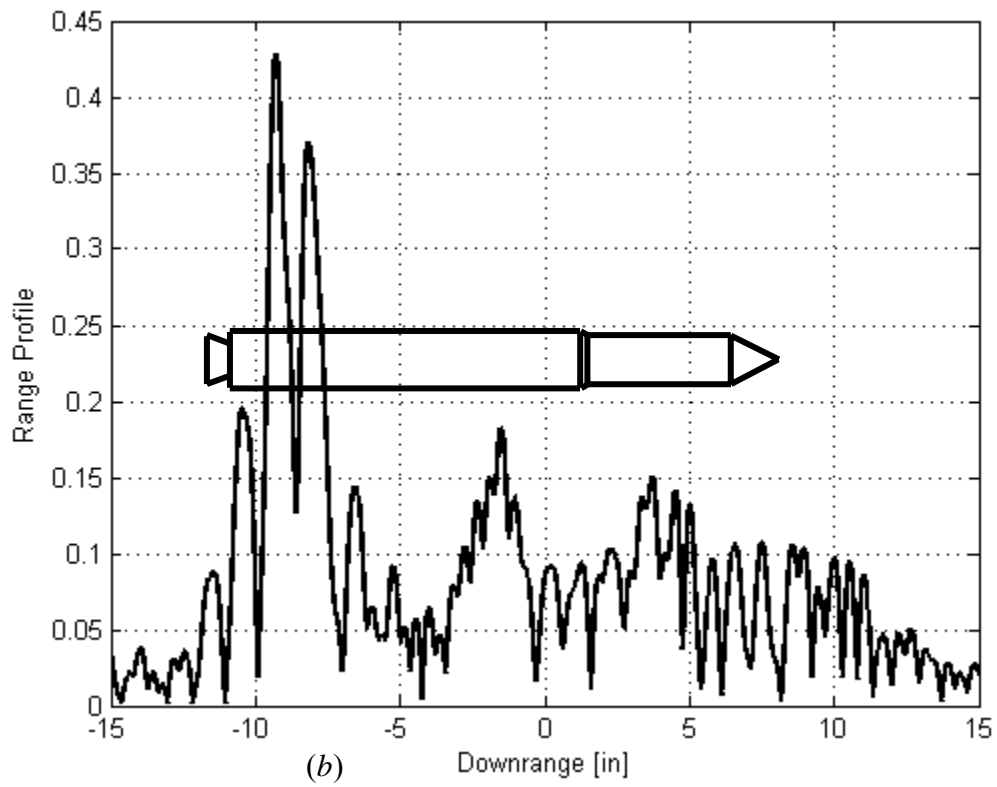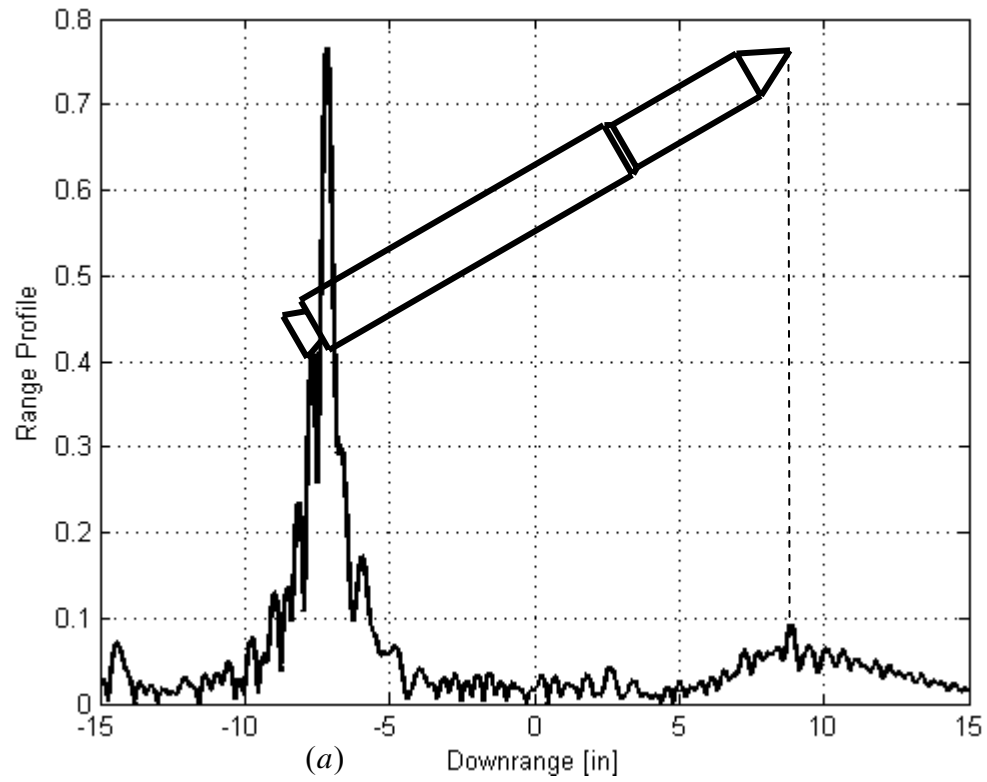
Figure 4-22: Missile model impulse response at (a) 150° and (b) 180°, HH polarization

Table 4-13: Range profile parameters

Figure	Azimuth (degrees)	Frequency sweep
Figure 4-21(a)	30°	2:0.1:18 GHz
Figure 4-21(b)	45°	2:0.1:18 GHz
Figure 4-22(c)	150°	2:0.1:18 GHz
Figure 4-22(d)	180°	2:0.1:18 GHz

$$(B/F) = \frac{18GHz - 2GHz}{16GHz} = 1 \qquad (1.1)$$
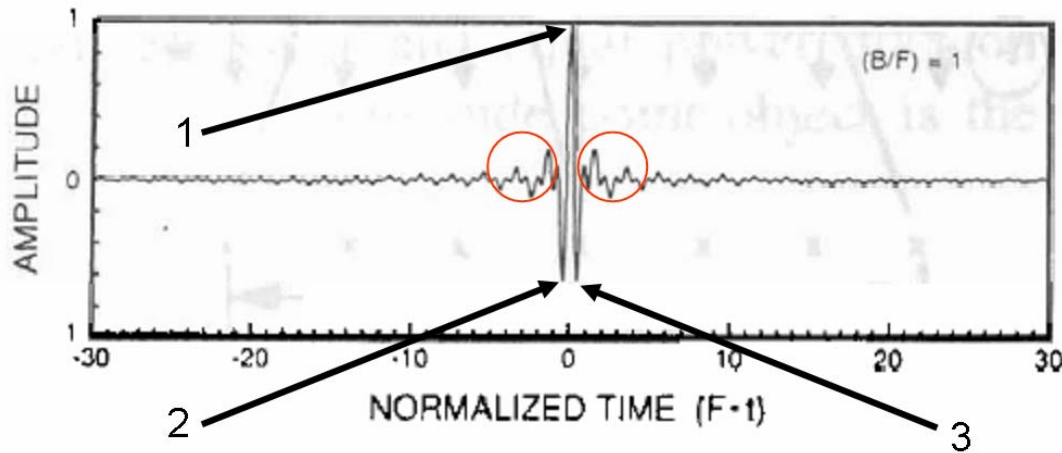
Figure 4-23: Impulse Response for Fractional Bandwith = 1. Peaks 2 and 3 are side lobes preceding and following the main lobe, peak number 1 The circled areas show additional sidelobes [11].

4.5.1   Lobe structure analysis

Recall from section 2.13, RCS fluctuations in terms of lobe widths can be characterized by examining the spatial distribution of scatterers, where lobe widths are inversely proportional to the cross-range extent of the target. At 0˚ the cross range extent of the target is the smallest therefore RCS lobes are wider and the received signal fluctuates more slowly around this observation angle. Figure 4-24 shows scatterer identified from range profiles for the missile model.
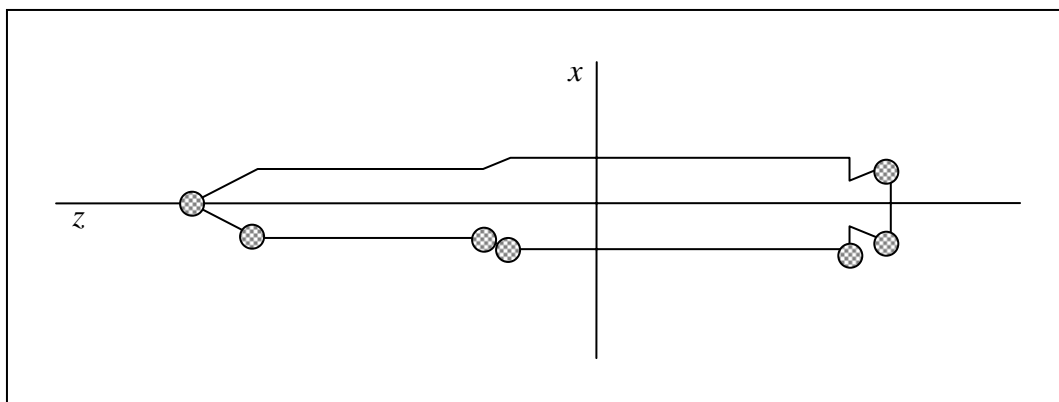
Figure 4-24: Target scatterers identified from range profiles

The spatial extent of scatterers is large in the side-on (z) dimension and small in the

nose-on dimension (x) as shown in Table 4-14.

Table 4-14: Spatial extent of scatterers of missile target

Frequency	Spatial Extent (λ)		Ratio $\left(\dfrac{z}{x}\right)$
	x	z	
400 MHz	$2\,\lambda$	$24\,\lambda$	12
500 MHz	$2.5\,\lambda$	$30\,\lambda$	12
1 GHz	$5\,\lambda$	$60\,\lambda$	12
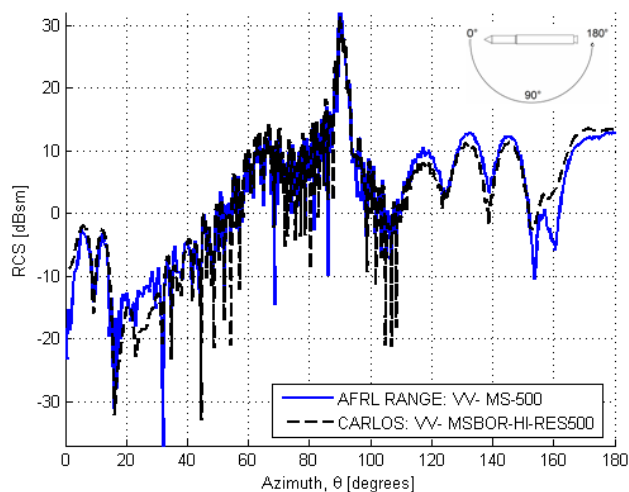
(a)
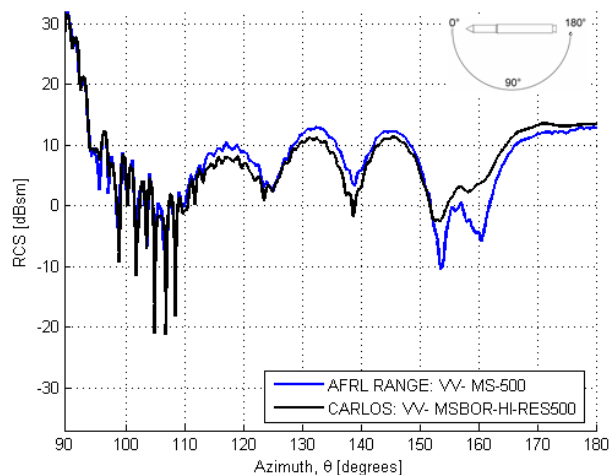
(b)

Figure 4-25: 500 MHz Missile RCS (a) 0-180° (b) 90-180° zoom-view

As seen in Figure 4-25, the widest lobes occur at the nose on and exhaust cavity aspect angles. The exhaust cavity is a reentrant structure [4] that reflects incident radar energy and tends to behave as a corner reflector. The lobe widths become increasingly narrow as the observation angle approaches broadside. With scatterers spaced widely apart there is more opportunity for constructive and destructive interference as the observation angle is varied. The RCS pattern of the target can be more easily seen if the azimuth scale is expanded; a 90° to 180° plot of the missile is shown in Figure 4-25. At a 90° observation angle, the maximum cross-range extent of scatterers in the z-dimension 12 times larger than the x-dimension, and the resultant RCS lobe widths are about 12 times smaller than at the 0° observation angle.

4.6   IBC results for flat plates

In this section, results are presented for comparison of measured data of flat PEC and MRAM-coated PEC flat plates. Section 4.6.1 compares PO predictions developed in section 2.19 to measured data. The motivation is to see how well a PO-type prediction that uses material parameters, such as used in Xpatch®, compares with IBC results from FISC. Section 4.6.2 compares measured results with results using FISC's default IBC formulation. Improvement in IBC results is investigated with the use of IBCs that are generalized to incorporate angle-dependence and polarization-dependence. Figure 4-26 shows the 9 GHz measured results for the PEC and MRAM-coated PEC plates. For HH polarization, the traveling wave, as indicated by the wide lobe seen near grazing on the PEC trace in Figure 4-26 (a), is greatly reduced due by the MRAM. Since the MRAM layer is thin, the electric field at the surface of the MRAM is close the PEC interface. Boundary conditions at a PEC interface force tangential electric fields to zero while the

tangential magnetic field is at its maximum. Due to the high permeability of the MRAM, magnetic energy from the incident wave is stored in the material. As the magnetic field of the incident wave oscillates, energy is expended due to reorientation of magnetic domains in the material. Reorientation of these magnetic domains requires energy and the resultant vibrational motion creates heat. The effect of MRAM on RCS is the most evident for the HH-polarization due to reduction of backscatter from a traveling wave. Recall that a traveling wave occurs when a component of the electric field lies in the plane of incidence. Stated otherwise, for HH-polarization, the components of electric field that are parallel with the plate surface drive a current across the plate (positive or negative) in the direction of propagation. Upon reaching edge continuities at the front and back edges of the plate, diffraction occurs where the current radiates a cylindrical wave. As a result of this diffraction, current sloshes back and forth between the front edge and back edge. In HH-polarization, (refer to Figure 2-20) the magnetic field is tangential to the surface for any incident angle in azimuth resulting in a maximum surface current and a greater loss of energy to the MRAM than for VV-polarization. This energy loss results in less available current to diffract at edge discontinuities and a big reduction in backscatter from a traveling wave. For a baseline of FISC performance compared to measured data Figure 4-27 shows FISC's PEC plate prediction. For VV-polarization leading edge scattering is attenuated slightly by the MRAM. Attenuation of the traveling wave, diffracted wave and leading edge attenuation are not accommodated by the PO approximation results of section 4.6.1
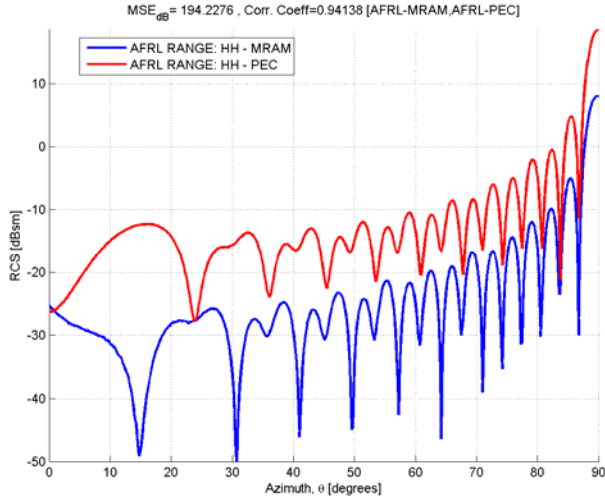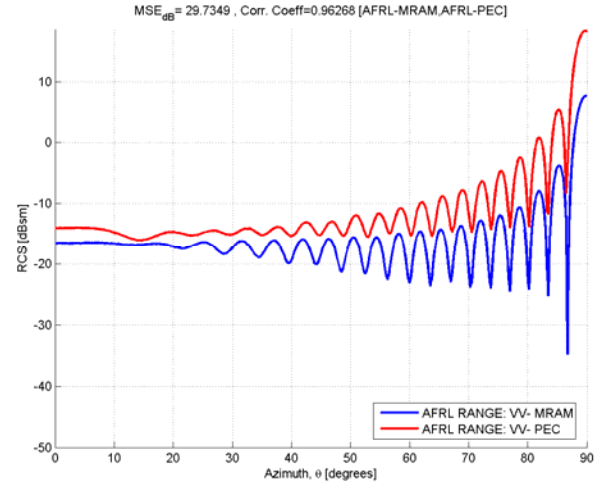
Figure 4-26: RCS of a 12″×12″ PEC and MRAM-coated PEC plate at 9 GHz, (a) HH-polarization, (b) VV-polarization
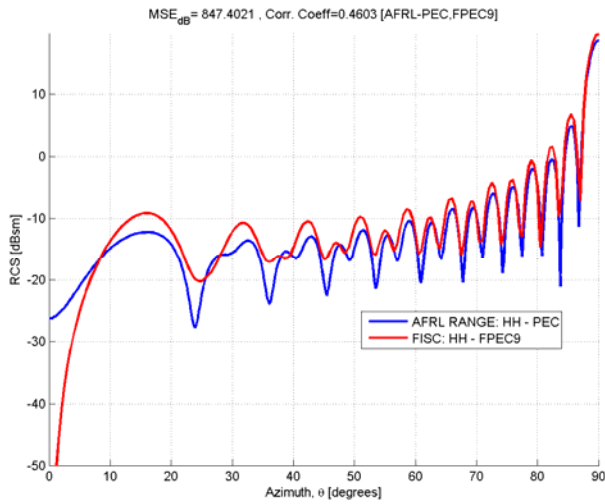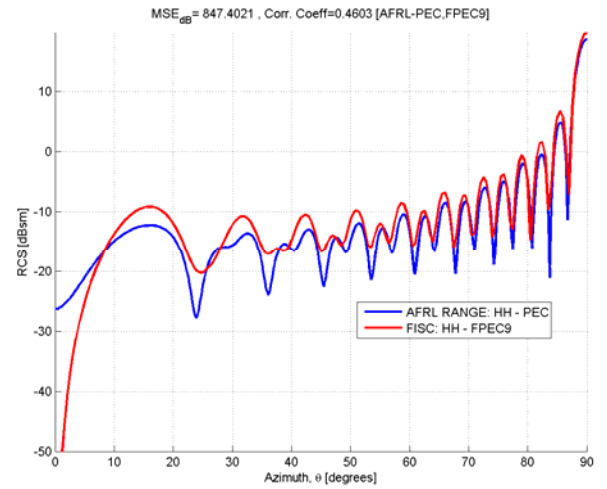
Figure 4-27: FISC prediction of a 12″×12″ PEC plate versus measured data at 9 GHz for (a) HH-polarization, (b) VV-polarization

4.6.1   PO approximation of a material-coated PEC plate

The RCS of measured data for a PEC and MRAM-coated PEC flat plates compared with

PO predicted data is shown in Figure 4-28. The AFRL traces are measured results for

MRAM-coated and PEC plates. At specular incidence, approximately 10.67dB attenuation is seen for the MRAM plate for both polarizations which exceeds the manufacturer's predicted 9dB attenuation loss shown in Figure 3-6. The blue trace is PO predicted data using measured material parameters from the waveguide material parameters given in Table 3-8. The sensitivity of the PO prediction to input material parameters is shown by the red bars where the upper limit is measured data from focus arch beam system and the lower limit is manufacturer-provided data. The range of PO prediction results from the input material parameters spans across the measured RCS for the MRAM plate from the specular angle until nearly 15° off specular. Thereafter, PO fails to model the physical behavior of scattering from the MRAM-coated, PEC finite-width plate. Recall from (2.81) that PO assumes a uniform current across the surface of the plate. For monostatic RCS at specular angles, the RCS contributions from currents that are approximately uniform dominate. This is not true at angles away from specular where other mechanisms such as traveling waves and edge diffraction dominate. This can be seen well for HH-polarization at angles far off of specular where traveling waves are dominant. Despite these shortcomings, the predicted PO results are within 3dBsm of the measured MRAM result from normal to approximately 20° off of specular for VV-polarization and to 35° for HH-polarization.

4.6.2   FISC IBC results

FISC results must shown in Figure 4-29 through must be qualified: the shown results did not converge within the specified error bounds after 800 iterations. Each incident angle required 3 hours of computation time. Results from test cases where the error-bounds were relaxed from 200e-3 to 400e-3 yielded approximately the same results.
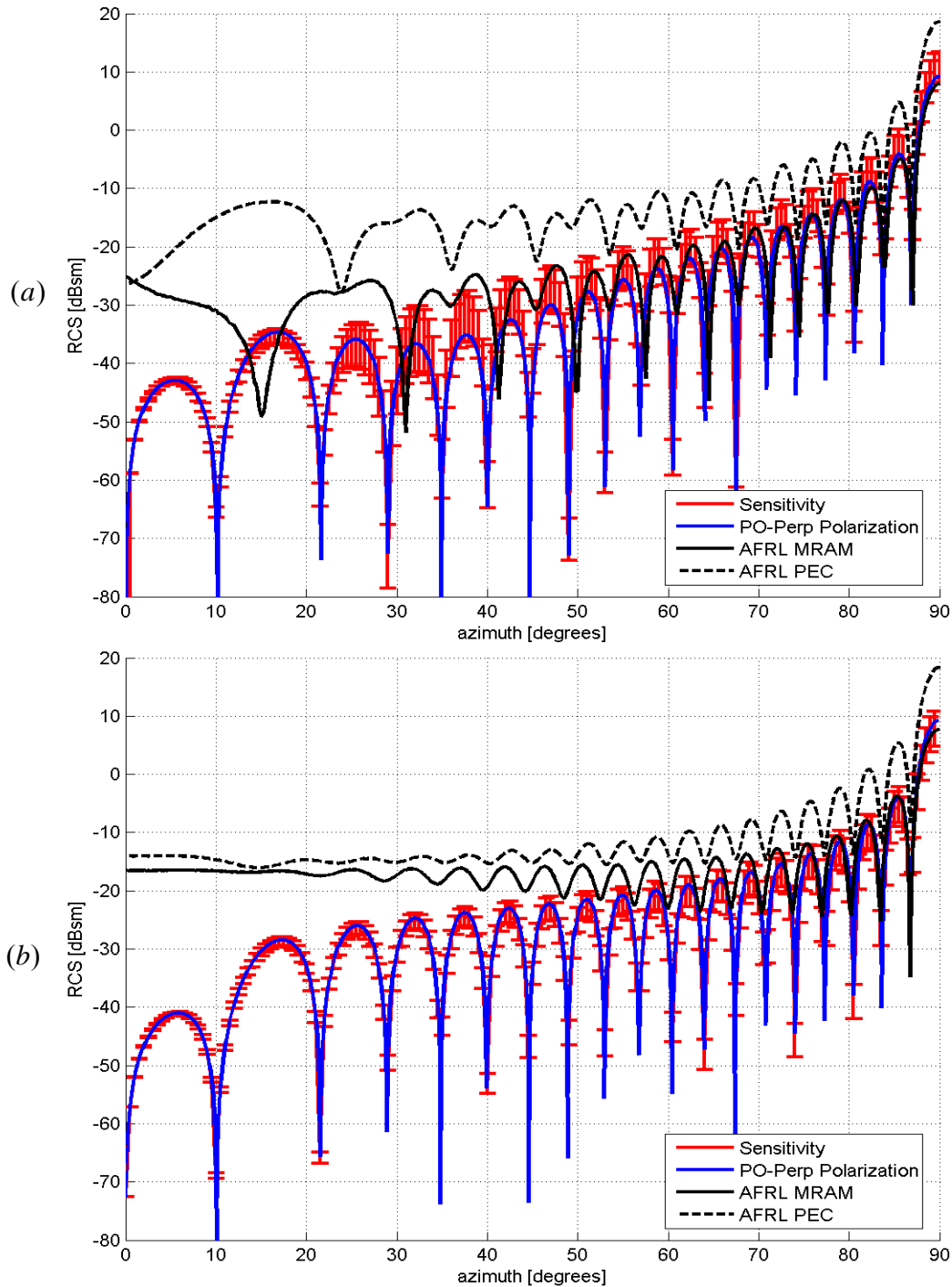
Figure 4-28: RCS of a finite-width, MRAM-coated PEC plate, at 9 GHz comparing measured data to a PO prediction; the AFRL traces are measured results for MRAM-coated and PEC plates. The sensitivity of the prediction is shown by the red bars where the blue line is data from a waveguide measurement, the upper limit is measured data from focus arch beam system and the lower limit is manufacturer-provided data; (a) perpendicular polarization, (corresponding to VV-polarization) (b) parallel polarization, (corresponding to HH-polarization).

The FISC-generated results, did not compare favorably to either the PO-approximation results nor the measured data as shown below where the red trace uses manufacturer-provided material parameters and FISC's IBC formulation to produce one one surface impedance value for every angle and both polarizations. Note that there are anomalous spikes where FISC diverged from the error bound specified in the FISC input page.

(a)   (b)
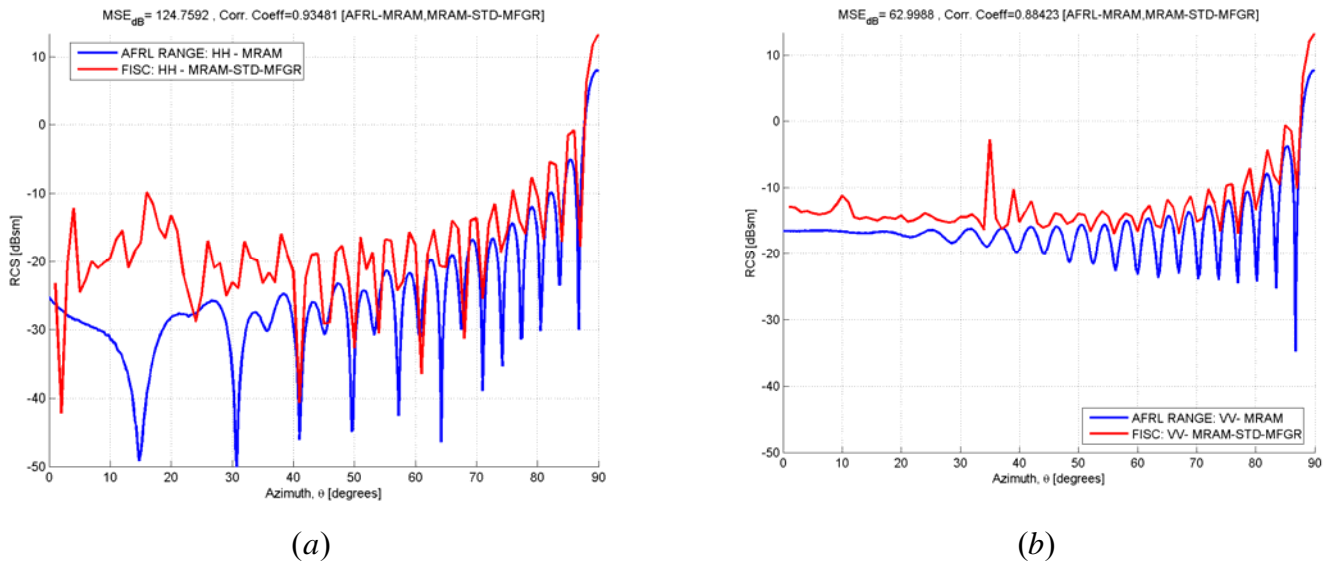
Figure 4-29: : FISC prediction of a 12″×12″ MRAM-coated PEC plate versus measured data at 9 GHz using angle-independent and polarization-independent IBC formulation for (a) HH-polarization, (b) VV-polarization

4.6.3 *Investigation of improved IBC results using modified IBC formulation*

Recall from (2.91) surface impedance is a function of frequency, material thickness, material parameters, polarization and angle of incidence. For each polarization and angle of incidence a separate input page was generated to produce figures. RCS was also predicted for the upper and lower material measurements and manufacturer data listed in Table 3-8 but no significant improvement was seen over the manufacturer-provided data.. FISC results show that the IBC results tended to have the character of the predicted PEC results and did not match well to the measured MRAM results. The conclusion is that for

a huge effort didn't result in any noticeable prediction improvement from the polarization and angle independent formulation.
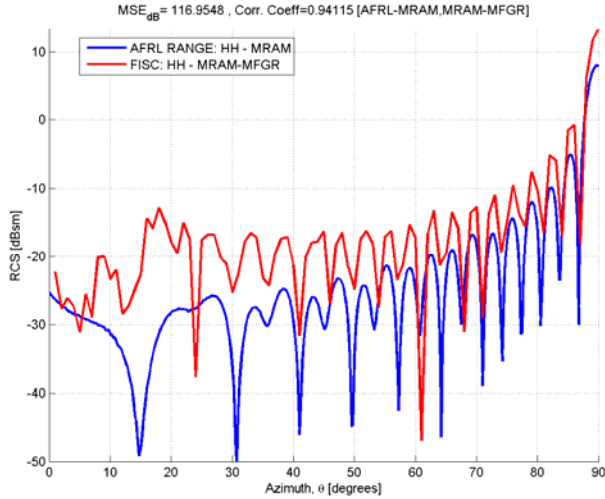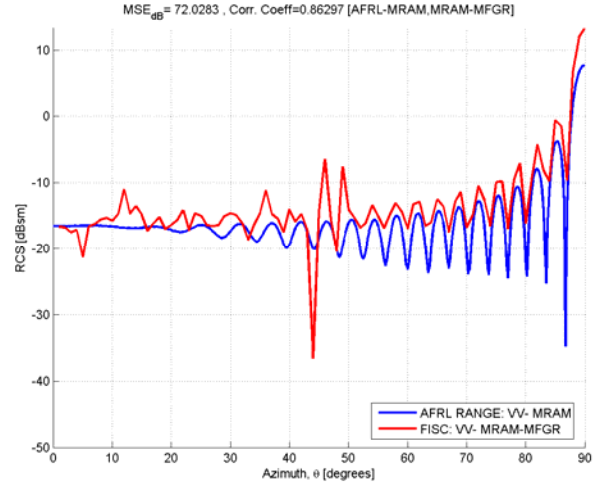
(a)   (b)

Figure 4-30: : FISC prediction of a 12″×12″ MRAM-coated PEC plate versus measured data at 9 GHz using angle-dependent and polarization-dependent IBC formulation for (a) HH-polarization, (b) VV-polarization
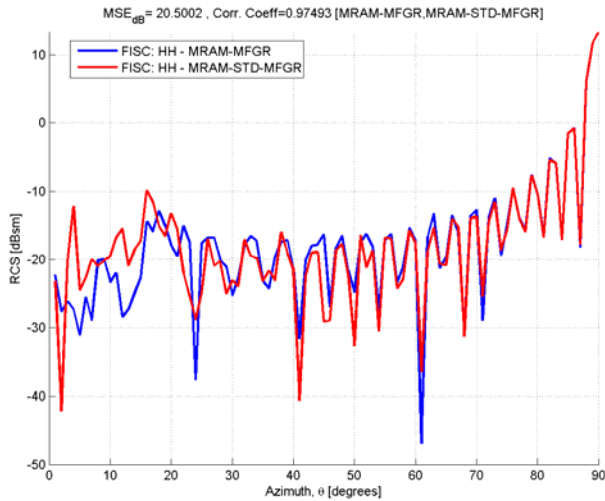
(a)   (b)

Figure 4-31: FISC predictions of a 12″×12″ MRAM-coated PEC plate, with FISC standard IBC versus generalized IBC formulation at 9GHz for (a) HH-polarization, (b) VV-polarization, the red trace is FISC's standard IBC

4.7 IBC results using large PEC and MRAM coated PEC cone

This section examines RCS predictions for a MRAM-coated PEC right-circular cone using FISC's standard IBC formulation. The geometry of the cone violates several of the assumptions for IBCs. IBCs assume an infinite, planar surface. With the cone, tip and edge diffraction are present and not accounted for by IBC formulation. Guided surface waves and traveling waves and are not accommodated by IBCs. Guided surface currents are present for the MRAM-coated cone due to edge diffraction setting up modes and guided surface waves within the material. Also, traveling waves are present when components of the electric field lie in the plane of incidence. IBC performance is best at angles normal to the surface and is expected to yield poor performance at other observation angles. Angles around the tip will yield especially poor performance since the cone is not even locally planar in that region. Figure 4-32 shows the measured results for the PEC and MRAM cone, adfashows the FISC MRAM-coated cone results little variation from the predicted PEC results.

(a)   (b)
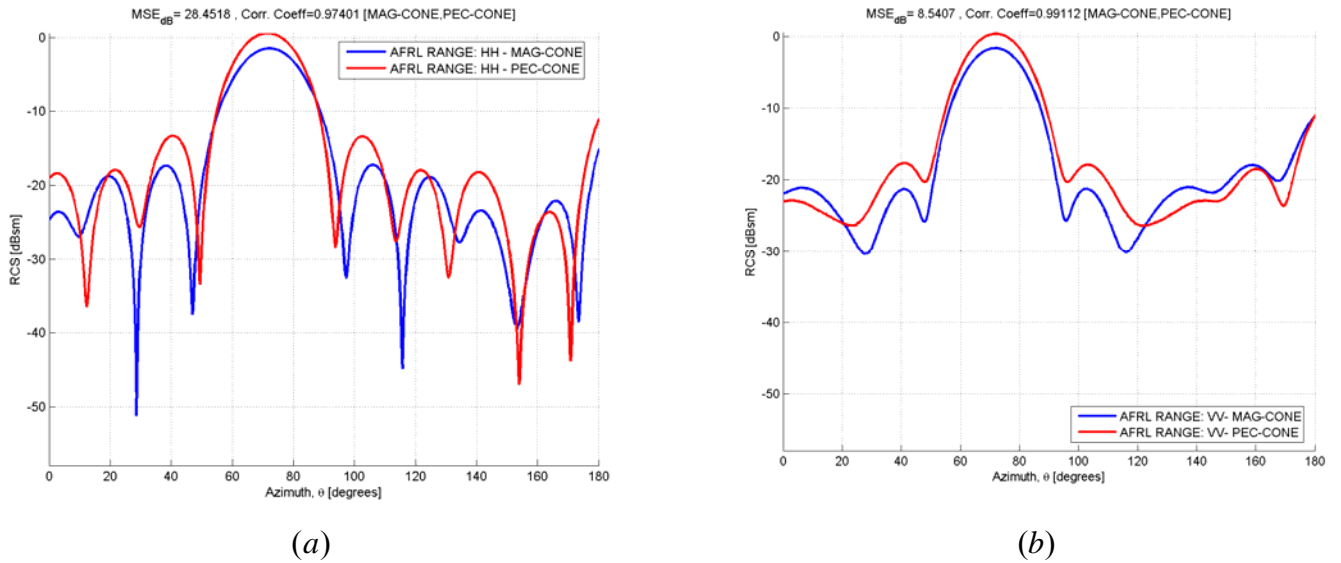
Figure 4-32: Measured data for a 9″×9″ PEC and MRAM-coated PEC cone, at 2GHz for (a) HH-polarization, (b) VV-polarization
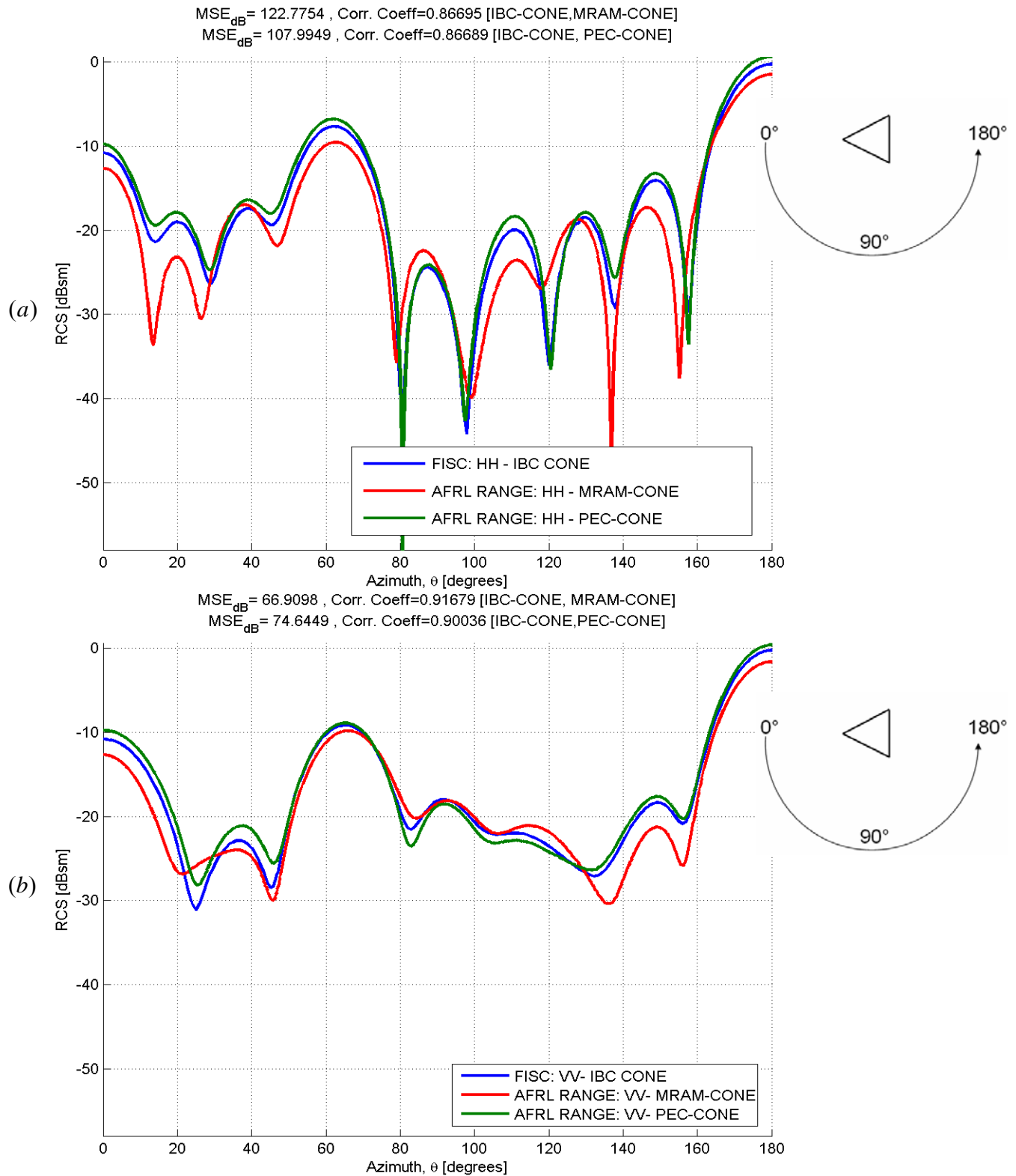
Figure 4-33: Measured data and FISC predicted RCS using standard IBC formulation for a 9″×9″ PEC and MRAM-coated PEC cone, at 2GHz for (a) HH-polarization, (b) VV-polarization

4.8   SAF, FISC, CARLOS-3D Performance

This section examines the CPU time and memory required to produce the RCS data for CARLOS-3D, FISC and SAF. SAF data were generated using a Dell Intel® Pentium® 4, 2.66 GHz processor with 1 GB of memory using a Linux operating system. RCS data for FISC and CARLOS were generated using SGI 3900 Origin processing nodes at the Aeronautic Systems Center (ASC) Major Shared Resource Center (MSRC). Each SGI processor has 1 Gigabyte (GB) of memory, the operating system is IRIX UNIX, and the processor is a 700 MHz, MIPS R16000 processor. FISC is a serial code that can only run on one processor at a time. However, when using computing resources at the ASC MSRC, should more than 1GB of memory be required, the additional memory can be allocated by requesting another processor through the batch queueing system. CARLOS- is a parallel code and up to 16 processors were used to generate data. No matter how many processors are specified, the upper limit on the number of unknowns for version 4.4.1 is hard-coded at 70k unknowns. By specifying more processors, solution time for CARLOS is reduced by a factor of the number of processors used. SAF data were generated using a Dell Intel® Pentium® 4, 2.66 GHz processor with 1 GB of memory using a Linux operating system. Figure 4-34 through Figure 4-37 show the actual memory usage and CPU times required to generate the RCS plots discussed in Chapter 4. These data were recorded in the FISC, SAF, and CARLOS output pages. For CARLOS-3D memory usage to store the impedance matrix was precisely the size of the matrix itself (multiplied times 8 bytes for each element), so no graphs were generated. Recall from Sections 2.17 and 2.18, the demonstrated memory and CPU time requirement for FISC and SAF when using MLFMA is $O(N \log N)$. This performance is verified from

the observed performance. The order was determined by performing a linear regression of the data points from output files. Memory requirements and CPU time may be empirically estimated from the data given in Table 4-15. Simply choose the target type for the code used, refer to the function listed in the appropriate graph, substitute in the number of edges and solve. Note that the estimates are most accurate when the target and processor type are similar. For CARLOS, performance estimates are given for one processor. Simply divide the answer by the number of processors used. The number of edges in column 3 of Table 4-15 gives the range of edges that was used to create the estimate.

Table 4-15: Empirically-derived estimation formulas for CPU time and Memory

Code	P	# Edges	Target type	M/C	Estimate	m/h
F	SGI	4.9-18k	Nosecone	C	$0.000467N \log_{10}(N) - 0.68$	m
F	SGI	4.9-18k	Nosecone	M	$0.000891N \log_{10}(N) - 5.2$	-
F	SGI	5.4-54k	Cylinder	C	$0.00046N \log_{10}(N) + 1.81$	m
F	SGI	5.4-54k	Cylinder	M	same as previous row	-
F	SGI	4.9-171k	Booster	C	$0.000135N \log_{10}(N) - 0.88$	h
F	SGI	4.9-171k	Booster	M	$0.000587N \log_{10}(N) + 46.55$	
F	SGI	49-265k	Missile	C	$8.8e\text{-}005N \log_{10}(N) - 24.3$	
F	SGI	49-265k	Missile	M	$0.000377N \log_{10}(N) + 6.37$	
S	P4	5.4-54k	Cylinder	C	$0.000495N \log_{10}(N) + 6.76$	m
S	P4	5.4-54k	Cylinder	M	$0.000493N \log_{10}(N) + 343.23$	-
C	SGI	7-14k	Nosecone	C	$5.5114e\text{-}011N^3 + 9.65$	h
C	SGI	7-14k	Nosecone	M	$\leq N^2$	-
C	SGI	15k-54k	Cylinder	C	$3.9885e\text{-}0011N^3 + 1.81$	h
C	SGI	15k-54k	Cylinder	M	$\leq N^2$	-

Code: C=CARLOS-3D, F=FISC, S=SAF
Processor(P): SGI=SGI 3900 Origin, 1 GB RAM, IRIX OS, 700 MHz, MIPS R16000
P4= Intel® Pentium® 4, 2.66 GHz processor
M/C: M=Memory estimate
C=CPU time estimate
m/h m=minutes
h=hours
- = Not applicable
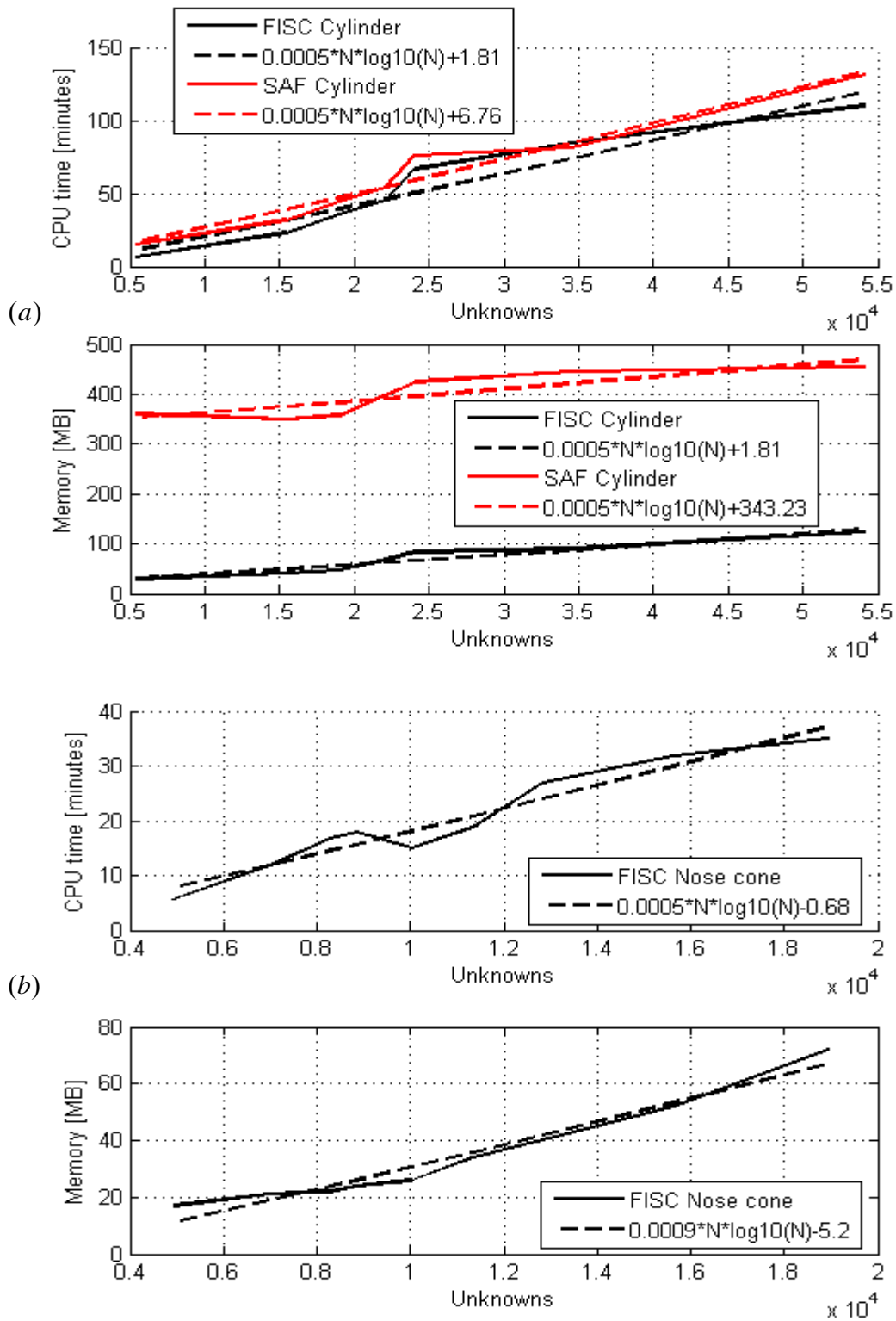
Figure 4-34: Performance data in CPU time and memory for (a) FISC and SAF Cylinder
(b) FISC nose cone

(*a*)

(*b*)
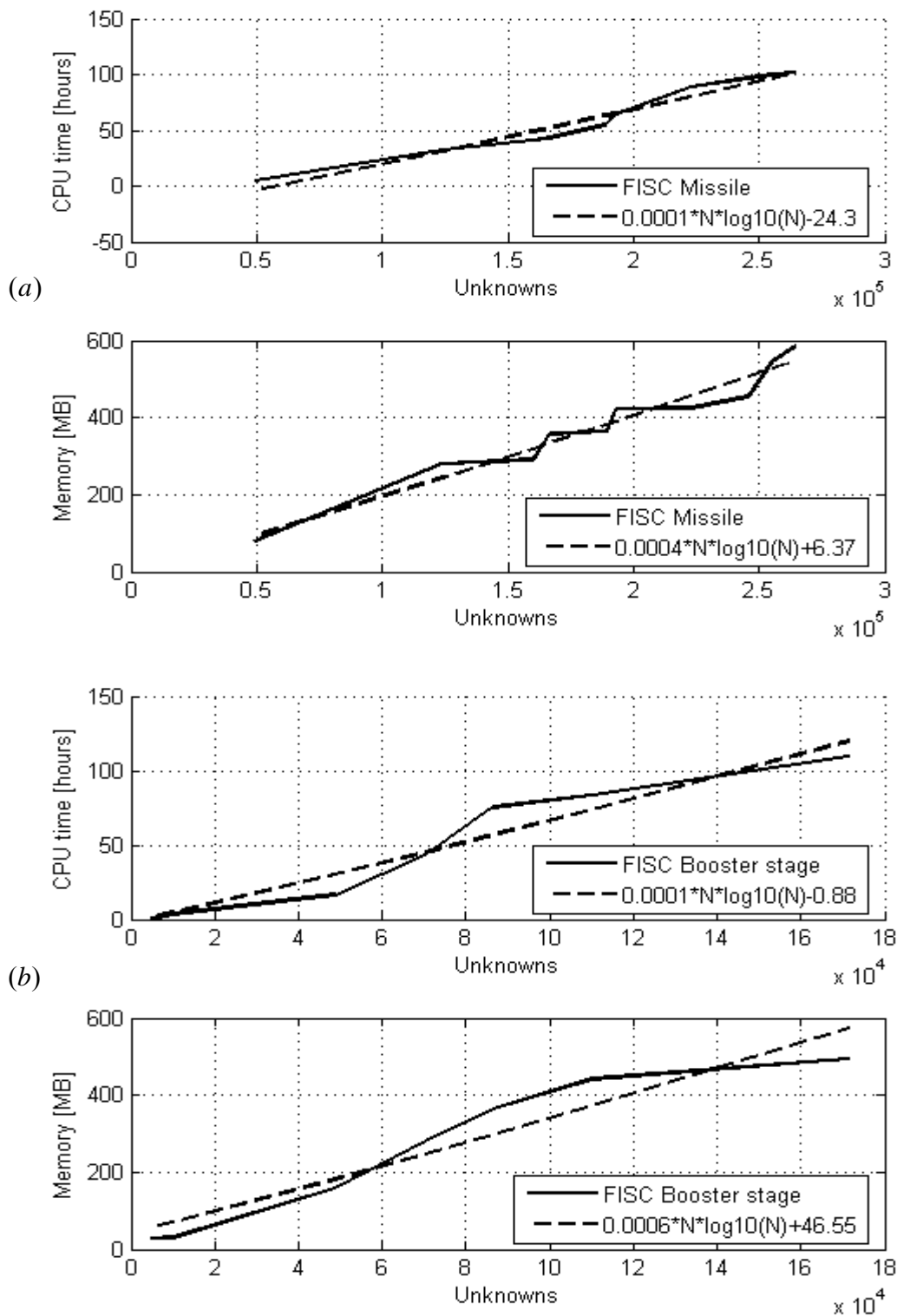
Figure 4-35: Performance data in CPU time and memory for (a) FISC missile and (b) FISC booster stage
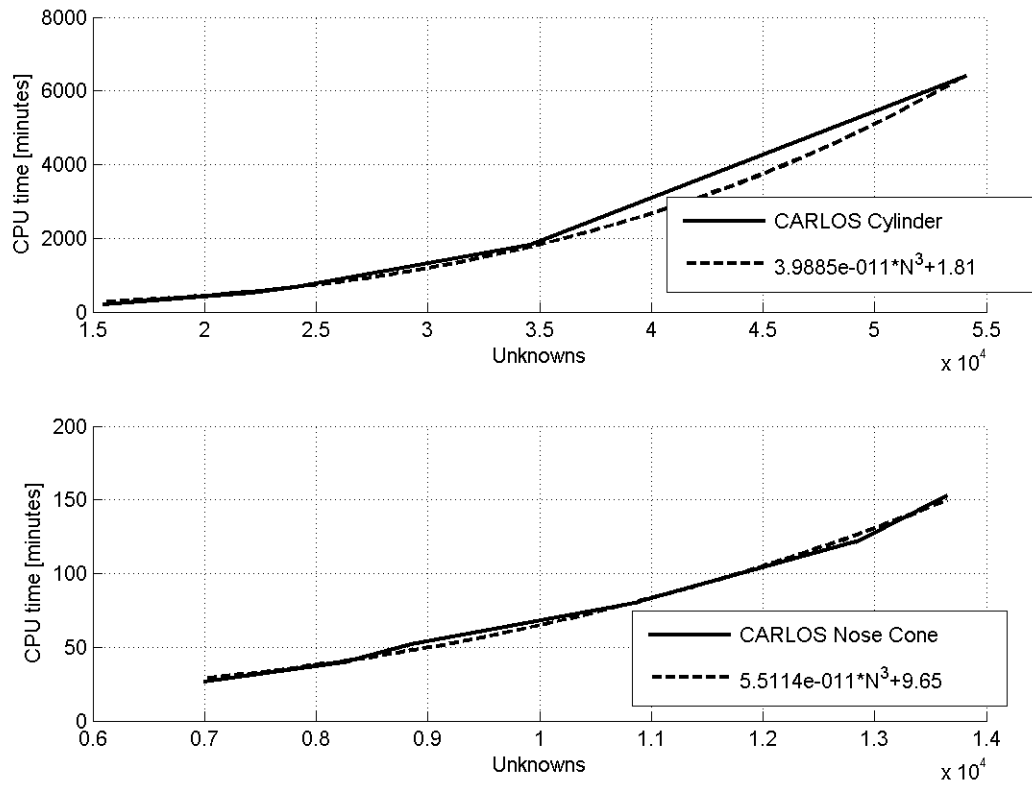
Figure 4-36: CARLOS performance in CPU time for (a) cylinder (b) nose cone

(*a*) (*b*)
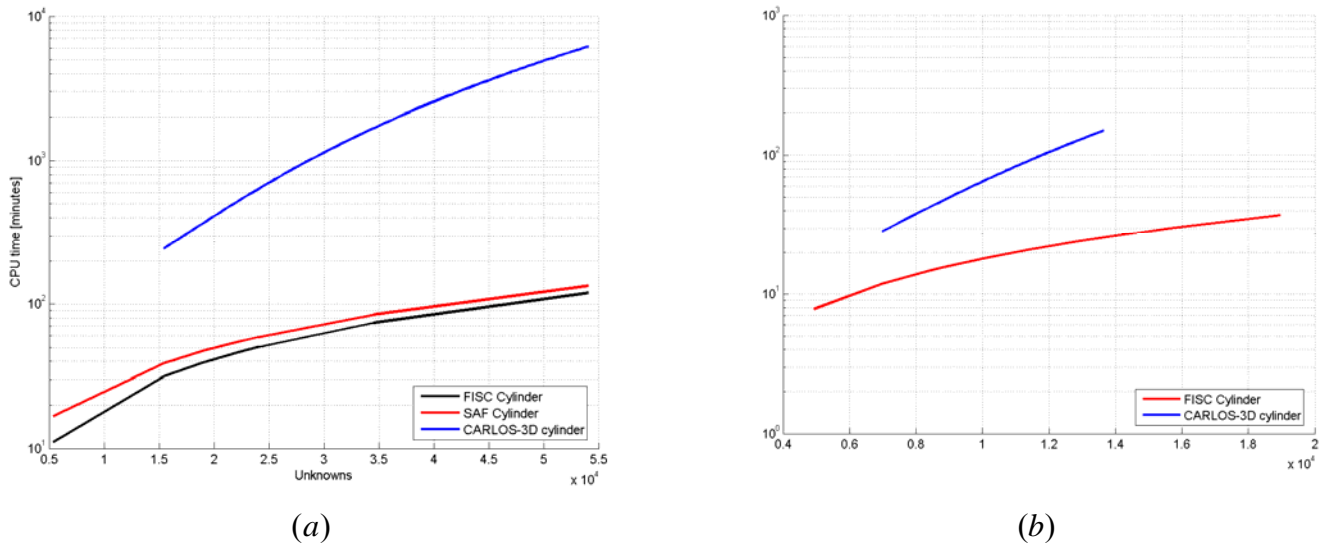
Figure 4-37: : CPU time performance comparisons (a) FISC, SAF, and CARLOS-3D CPU time for the cylinder RCS prediction (b) FISC and CARLOS-3D CPU time for the nose cone RCS prediction

4.9   Summary

The results show that FISC, SAF, and CARLOS produce accurate RCS predictions for simple, closed PEC targets. For the missile cavity FISC and CARLOS no longer had the tight agreement prevalent in RCS patterns for closed structures. For the missile tip, CARLOS-BOR and FISC diverged slightly but this may be attributable to differences between the CARLOS-BOR geometry and the finitely meshed tip of the facet file.

It was shown that lobing structure can be estimated by the examining the ratio of the spatial extent of scatterers. While this is not an exact method to verify lobing structure, it does yield a good rule-of-thumb for lobe widths.

The FISC IBC feature does a poor job in predicting RCS for material-coated PEC objects. For the best case scenario of a large flat MRAM-coated PEC plate at specular , FISC RCS prediction is off by over 5dBsm. FISC IBC prediction of the MRAM-coated PEC cone yields results closer to measured data for the PEC cone than measurements for the MRAM cone. Investigation into incorporating angle-dependent and polarization surface impedance yielded no improvement. Additionally, solution time significantly increased for IBC predictions and converged solutions could not be obtained. PO approximations performed better at specular than FISC IBC formulation.

FISC and SAF demonstrated $O(N \log N)$ performance in terms of memory and computational time. The order was determined by linear regression and a table of formulas was created for empirical memory and computational time estimation. CARLOS-3D demonstrated solution speed of $O(N^3)$. While this may be expensive in terms of computation time, as a parallel code, CARLOS can utilize multiple processors.

5 *Conclusions*

The capabilities of three computational electromagnetic codes were compared for use in production of RCS signature assessments at low frequencies in terms of performance, accuracy, and features: FISC, CARLOS-3D, and SAF. Predicted and measured RCS of several simple objects and a complex target was analyzed. Verification of code performance in memory and processing time based on varying levels of unknowns was performed. A comparison was conducted between measured and predicted results for two PEC objects coated with magnetic radar absorbent material (MRAM). The RCS for an MRAM-coated PEC 12″×12″ flat plate and a 9″×9″ MRAM-coated PEC right circular cone are measured in Air Force Research Laboratory compact RCS/antenna measurement range and then compared to results from FISC using its impedance boundary condition (IBC) feature. A physical optics method for predicting RCS of a material-coated PEC plate is also developed as a third data set to compare with the measured data and FISC predictions using IBCs for flat MRAM-coated plates. The IBC formulation was generalized for polarization and angle-dependent impedances to investigate prediction improvement. Results of this thesis show that the three codes offer good accuracy for predicting PEC shapes. FISC and SAF offer a significant advantage in computation time due to MLFMA. FISC's IBC formulation does a poor job of predicting RCS of MRAM-coated PEC objects.

5.1 Future Research

5.1.1 Material-coating RCS performance analysis

Throughout this research the ultimate goal was to evaluate the capabilities of FISC, CARLOS-3D, and SAF for purposes of RCS signature data production. It was shown that each of these codes performed well and had closely correlated results for PEC objects. Realistically, targets of interest have material coatings that greatly affect RCS. A natural extension of this research would be to examine the RCS performance of SAF and CARLOS with material-coated PEC objects.

5.1.2 Cavity structure RCS performance analysis

Another topic area would be a careful analysis of the RCS performance with cavity structures. Just as this thesis used PO approximations as a comparison to IBC performance, 2-D finite-difference time domain and finite-element methods are easily implemented to compare with CEM code cavity predictions.

5.1.3 CARLOS iterative solver

Use of CARLOS' iterative solver was not performed during this thesis. Although FMM is not incorporated into CARLOS, comparative empirical data analysis would help determine if using CARLOS with an iterative solver makes it more useful for RCS production.

Appendix A. Integral Proof

This appendix contains the proof for the integral relations shown in (2.65) and (2.82).

$$\int_{-a/2}^{a/2} e^{jk_0 x' \sin\theta\cos\phi} dx' = \mathrm{sinc}X ; \qquad\qquad (A.1)$$

details:

$$\text{let } u = jk_0 x' \sin\theta\cos\phi$$

$$\text{then } du = jk_0 \sin\theta\cos\phi dx' \Rightarrow \frac{du}{jk_0 \sin\theta\cos\phi} = dx'$$

$$\frac{1}{jk_0 \sin\theta\cos\phi} \int_{-a/2}^{a/2} e^u du = \frac{1}{jk_0 \sin\theta\cos\phi} \left. e^u \right|_{\frac{-a}{2}}^{\frac{a}{2}} ; \text{ evaluate and multiply by unity}$$

$$= \frac{e^{j\frac{a}{2}k_0 \sin\theta\cos\phi} - e^{-j\frac{a}{2}k_0 \sin\theta\cos\phi}}{jk_0 \sin\theta\cos\phi} \cdot \frac{\frac{a}{2}}{\frac{a}{2}}$$

note:

$$\mathrm{sinc}x = \frac{\sin x}{x} ; \quad \sin x = \frac{e^{jx} - e^{-jx}}{2j}$$

let $X = \dfrac{a}{2} k_0 \sin\theta\cos\phi$;

Grouping terms:

$$\int_{-a/2}^{a/2} e^{jk_0 x' \sin\theta\cos\phi} dx' = a\frac{e^{jX} - e^{-jX}}{2jX} = a\,\mathrm{sinc}X ;$$

Appendix B.   CARLOS Input Sections Overview

1. Title Section – Problem description
2. Namelist Input section: $OPTION variable=value, … $END
3. Frequency Input Section
4. Dielectric Region Input Section, a.k.a Material Boundary Condition
5. Surface Definition Input Section (2D-BOT, BOR, PATCH, or WIRE)
   a. BOR (body of revolution) Surface Input Section: GEOM=BOR.
   b. 3D Input Section (AIM Algorithms)   GEOM=AIM
   c. 3D Input Section (PATCH GEOMETRY)   GEOM=PATCH
   d. 3D Input Section (FACET FILE DESCRIPTION)
6. Pattern Cut and Plane Wave Excitation Section
7. Near-Field Post Processing Section
8. Parameter Mapping Run Section
9. Stack File Input Section
10. User Function Section
11. FMM Section for 3D

Appendix C. CARLOS Sample Input Page (Body of Revolution)

Cylinder with flat end caps
$OPTION ifree=-1 freq =.true. alpha=0.4
trans=.true. tol3d=0.0001 bor_seg=20
mono=1 units='CM' quad = .true.
$END
DFREQ=2
8.0 16.0
0
BOR
0 0 0
-19 pec disk
0 -1 1
0.0 0.0 5.0 0.0 1.0e-20 0.0

-51 pec cylinder wall
0 -1 -1
5.0 0.0 5.0 10.0 0.0 0.0

-19 pec disk
0 -1 -1
0.0 10.0 5.0 10.0 1.0e-20 0.0
0
0
END
181
0.0 1.0 0.0 180.0

Title Section:
Problem description, max 80 columns

Namelist:
Free space region is -1, this means that the free space region does not need to be entered as one of the NREG regions.
Input frequency in GHZ
Alpha =0.4 is the CFIE weighting coefficient: CFIE=alpha*EFIE+(1-alpha)*MFIE. If any of the surfaces are infinitely thin, Carlos sets Alpha=1 for that surface.
Trans=.true. (Sx,Sy,Sz) & (Tx,Ty,Tz) for each surface
Tol3d=0.0001 tolerance to collapse vertex pts. Less than the tolerance and the vertex pts set to same pt
bor_seg=20
Monostatic, CM
quad = .true. quad patch surfaces are allowed in the #D geometry input. (pg 36)The type of surface is specified by an additional value...

Frequency Input Section:
DFREQ=2 2 discrete frequencies (FR1 & FR2) due to the freq =.true. from namelist section, otherwise it would have to be wavenumbers, ie. BK1 and BK2

Surface Definition Input Section (Here BOR):
Mode 1, usually set to zero (SNN Fourier mode)
Mode 2, largest NN Fourier mode
NGAUSS, set to 0 program chooses max(2*k*rho+1)
NP - # points, (odd) to describe a surface
NIR - # interior region away from which surface normal points
NER Number (index) of exterior region
ITYPB Type of surface, 1 = PEC
ZB: if NP is negative
READ(5,*) RB1,ZB1,ZB2,RBC,ZBC

Dielectric Region Input:
0 set to zero here because there are no OTHER dielectric regions other than the one established by setting ifree=-1 in the namelist

---

Surface Definition Input:
BOR for body of revolution

Pattern Cut and Plane-Wave Excitation:
NANG – number of angles
ANG = fix angle at # degrees
IANG = fix 1 for Phi, fix 2 for theta
ANG1 = starting angle ANG2 = ending angle

Appendix D.   SAF Sample Input Page

```
#--- SAF v3.1 Input page
#    User comment: Modified 8/11/05
#********************************
#A: Target and Radar configuration
#********************************
#---Target_type: 1= with surface mesh for PEC or IBC surfaces
#                2= with volume mesh for complex (eps, mu) material
#                3= with both surface and volume meshes
#                   When both meshes are present, even if they don't touch
#                   each other, they have to be "paired" as follows: Triangular
#                   facet with 3 nodes goes with tet with 4 nodes (tri3 with
#                   tet4); quad4 with hex8; and quad9 with hex27.
#                0= No target and both mesh files given below will not
#                   be read (dummies). This option is for computuing
#                   primary patterns/fields in ADV02, ADV03 ...
 1
#---Enter a surface mesh file (enter a dummy file if target_type=2)
target.facet
#---Enter a volume mesh file (enter a dummy file if target_type=1)
volume.hex
#---Length unit:  1=inch, 2=cm, 3=meter, 4=mm, 5=mil.
#   The same length unit is used in all CAD files and input entries.
#   The time convention is exp(+jwt)
 3
#---Frequency(GHz): start, stop, and nstep.
#   (nstep is # of increments e.g. nstep=0 for 1 point)
 0.5 0.5 0
#---If ADV02(antenna pattern) or ADV03(antenna coupling) is on, the
#   remainder of Sec.A is dummy.
#---Incident polarization: 1 = E-theta(Vertical pol.),
#                          2 = E-phi  (Horizontal pol.),
#                          3 = Both pols.
 3
#---Radar configuration: 1=monostatic RCS,  2=bistatic RCS.
 1
#---Incident EL: start, stop, and nstep (All angles in deg: EL=90-theta).
#   (nstep is # of increments e.g. nstep=0 for 1 point)
90.0 0.0 0
#---Incident AZ: start, stop, and nstep (AZ=-phi).
 0.0 0.0 0
#---Observation EL: start, stop, and nstep (dummy for mono).
90.0  -90.0 15
#---Observation AZ: start, stop, and nstep (dummy for mono).
 0.0 0.0 0
#***********
#B: MATERIAL
#***********
#---Is the entire target PEC?   1=yes,  0=no.
 1
#---If PEC, the rest of Section D is dummy.
#   If non-PEC, enter total # of materials (N_material):
#   (Do not count PEC in N_material. PEC is identified by ICOAT=0)
 5
#---For each material, identify its ICOAT and IBOUNDARY:
```

```
#   ICOAT = any positive integer from 1 on (need not be consecutive).
#   IBOUNDARY = 1 if impedance boundary condition IBC (surface mesh)
#               2 if resistive sheet RS (surface mesh)
#              11 if material with complex epsilon and mu (volume mesh)
#   For each material, fill in one of the following templates.
#^^^ a new material: IBC with impedance input
#---ICOAT (any positive integer from 1 up)
 1
#---IBOUNDARY
 1
#---Complex surface impedance in ohm e.g (35.45 -90.76)
#   The IBC surface must be a closed surface such as a sphere.
 (345.0,67.6)
#^^^ a new material: RS with resistivity input
#---ICOAT (any positive integer from 1 up)
 2
#---IBOUNDARY
 2
#---Complex resistivity in ohm per square e.g (1500.24 -2500.76)
 (0.0,-4000.0)
#^^^ a new material: Bulk material
#---ICOAT (any positive integer from 1 up)
 3
#---IBOUNDARY
 11
#---Relative complex epsilon and mu e.g. (3.25,-0.04) (2.45,-0.32)
#   Time convention is exp(jwt) so negative imaginary part
#   represents loss
 (4.0,-2.0) (1.0,-0.0)
#^^^ a new material: IBC with epsilon/mu/thickness input
#---ICOAT (any positive integer from 1 up)
 4
#---IBOUNDARY (Special case 1 for IBC)
 1    SPECIAL=1   LAYER=1
#---Use IBC to approximate thin dense material layers over a PEC backing.
#   The IBC surface must be closed such that only one side is exposed.
#   Enter complex epsilon, mu, thickness(in unit specified in Sec.A). Use
#   one line for a layer and start with the layer fartherest from the
#   incident field (innermost to the PEC).
(3.42, -0.3) (1.8, -1.2)  0.03
#^^^ a new material: RS with epsilon/thickness input
#---ICOAT (any positive integer from 1 up)
 5
#---IBOUNDARY (Special case 5 for RS. See manual for other cases)
 2    SPECIAL=5
#---Use RS to approximate a thin dielectric layer in the free space.
#   Enter complex epsilon, thickness(in unit specified in Sec.A)
(2.45, -0.12) 0.045
#############################
#C: Optional Advanced features
#############################
# Advanced features are recognized by key words such as "#ADVANCE03". Hence not
# all advanced features need be present in an input page and they can be
# arranged not in order.
#--------------------------
#ADVANCE01: ACCURACY SETTING
#--------------------------
```

```
# Option to set different level of accuracies: 1=yes, 0=no
 0
# If "yes", select an accuracy level:
# 0=Low, 1=Mid(default), 2=High, 99=Using LUD not MLFMA iterative solver
 1
#-----------------------------------
#ADVANCE02: Installed Antenna Pattern
#-----------------------------------
# In this feature, SAF is used to compute the installed antenna pattern
# in the presence of a scatterer described by the CAD file given in Sec.A
# Option to use this feature: 1=yes and 0=no.
0
# The CAD file is described in the main coordinate(Coord0), and the antenna in
# its own Coord1. Enter the xyz of the origin of Coord1 in Coord0.
0.0  0.0  0.0
# Enter unitary base vectors x1 and y1 of Coord1 in Coord0.
1.0  0.0  0.0
0.0  1.0  0.0
# The antenna is an array of N identical elements.
# Options to describe the element pattern are:
#   Format         //Explanation
#   0 horn.antpat  //Far-field pattern in an external file (Use gen_antpat.f)
#   1              //Electric dipole along z in Coord1 with NF(near-field
terms)
#   2              //Magnetic dipole along z in Coord1 with NF
#   3  5.2         //Electric dipole of length 5.2 along z in Coord1 with NF
#   6  2.6 121     //Electric V-dipole with arm length 2.6 and V-angle 121 deg
#                    The dipole is in zx-plane and the bend is from z,with NF.
# If electric dipole or magnetic dipole (Option 1 or 2 above) is selected
# as element, then there is an additional option to specify the orientation
# of each element by entering a phrase "any direction" or "direction=any", such
# as  "2 any direction".
1
# Enter N, the number of array elements in the antenna.
1
# For each element, enter its location xyz in Coord1, its
# relative excitation magnitude and phase(deg) in a new line.
# For the special case that element directions are allowed to vary, enter
# unit vector ux,uy,uz as the 6, 7, 8th columns.
0.0, 0.0, 0.0,        1.0, 0.0
# Enter M_Vcut, the number of installed vertical pattern cuts to be calculated.
# (Enter "GREATCIRCLE" after the M_Vcut if great circle output is needed)
1
# For each Vcut, enter AZ(deg in Coord0), EL1, EL2, steps.
0.0, 0.0, 360.0, 360
# Enter M_Hcut, the number of installed horiz. pattern cuts to be calculated.
# (Enter "GREATCIRCLE" after the M_Hcut if great circle output is needed)
1
# For each Hcut, enter EL(deg in Coord0), AZ1, AZ2, steps.
0.0, 0.0, 360.0, 360
# Two options to normalize the directivity of the installed patterns:
#   1= Normalized wrt the power of the primary antenna pattern(fast)
#   2= Normalized wrt the power of the installed antenna pattern(accurate)
1
#--------------------------
#ADVANCE03: ANTENNA COUPLING
#--------------------------
```

```
# Option to calculate antenna coupling between a Tx array and a Rx array:
# 1=yes and 0=no.
0
# The CAD file is described in the main coordinate(Coord0), and Tx antenna in
# its own Coord1. Enter the xyz of the origin of Coord1 in Coord0.
100.0  0.0  100.0
# Enter the base vectors x1 and y1 of Coord1 in Coord0.
-0.707107  0.0  0.707107
 0.0  1.0  0.0
# Tx antenna is an array of N identical elements.
# All elements in an array have the same pattern.
# Options to describe the element pattern are:
#   Format         //Explanation
#   0 horn.antpat  //Far-field pattern in an external file (Use gen_antpat.f)
#   1              //Electric dipole along z in Coord1 with NF(near-field
terms)
#   2              //Magnetic dipole along z in Coord1 with NF
#   3  5.2         //Electric dipole of length 5.2 along z in Coord1 with NF)
 1
# Enter N of Tx array
 1
# For each Tx element, enter its location xyz in Coord1, its
# relative excitation magnitude and phase(deg) in a new line.
0.0,  0.0,  0.0,        1.0,  0.0
# The CAD file is described in the main coordinate(Coord0), and Rx antenna in
# its own Coord2. Enter the xyz of the origin of Coord2 in Coord0 using one of
# the following two formats:
# ---Format 1:
#   1  3            (Format, number of Rx origin positions)
#   x01  y01  z01   (Rx position-1)
#   x02  y02  z02   (Rx position-2)
#   x03  y03  z03   (Rx position-last)
# ---Format 2:
#   2  5          (Format, number of linear increments)
#   x0_str y0_str z0_str  x0_end y0_end z0_end
1 1
0.  0.   141.421
# Enter the base vectors x2 and y2 of Coord2 in Coord0.
-0.5  -0.86602  0.0
-0.86602   0.5  0.0
# Rx antenna is an array of M identical elements.
# All elements in an array have the same pattern.
# Options to describe the element pattern are:
#   Format         //Explanation
#   0 horn.antpat  //Far-field pattern in an external file (Use gen_antpat.f)
#   1              //Electric dipole along z in Coord2 with NF(near-field
terms)
#   2              //Magnetic dipole along z in Coord2 with NF
#   3  5.2         //Electric dipole of length 5.2 along z in Coord1 with NF)
#   6  2.6 121     //Electric V-dipole with arm length 2.6 and V-angle 121 deg
#                    The dipole is in zx-plane and the bend is from z,with NF.
 1
# Enter M of Rx array
1
# For each Rx element, enter its location xyz in Coord2, its
# relative excitation magnitude and phase(deg) in a new line.
0.0,  0.0,  0.0,        1.0,  0.0
```

```
# Option to change the phase of Rx elements listed above: 1=yes, 0=no
0
# If yes to phase change, Rx is then a co-phasal array whose main beam is in
# the (theta, phi) direction in Coord2. Enter (theta, phi) in deg in one of two
# formats in the following:
# ---Format 1:
#    1  3          (Format, number of beam positions)
#    theta1, phi1
#    theta2, phi2
#    theta_last, phi_last
# ---Format 2:
#    2  26         (Format, number of linear increments)
#    theta_str phi_str   theta_end phi_end
2   12
0.0   45.    60.    45.
# Antenna coupling is calculated by integrating fields over a closed surface S
# enclosing the Rx array and excluding the scatterer. If the direct incident
# field is to be included the coupling calculation, the S should exclude the Tx
# array also. Two options for S:
#  1 = a box, 2=a closed surface described by a CAD file
#  3 = use far-field approximation (no need to set box or file name)
2
# If S is a box, enter x1 x2 y1 y2 z1 z2 in main Coord0
-1.5 1.5  -1.5 1.5  -1.5  1.5
# If S is described by an external CAD file, enter its name (e.g. box.facet or
# sphere.quad)
sphere_100.quad
# The coupling integration over surface S is done by a mesh spacing d.
# Enter d in the same unit as target (typically 0.1 to 0.5 wavelength)
0.1
# Coupling calculation is normally done by using TOTAL (incid + scat) field.
For
# special applications, (e.g. computing near-field bistatic RCS), this
# calculation may be done with the scat field only.
# Option of using scat field only: 1=yes, 0=no
1
#--------------------------------
#ADVANCE04: FREQUENCY INTERPOLATION
#--------------------------------
# Option to use frequency interpolation for scattered field: 1=yes, 0=no
 0
# Enter the number of frequencies that SAF will calculate their fields without
# interpolation. (This number is generally smaller than that given in Sec.A
# and with a lower bound of 10*(L2-L1) where (L2,L1) is the target size in
# wavelength at (high, low) frequencies.
 5
#--------------------------------
#ADVANCE05: APPROXIMATE GROUND PLANE
#--------------------------------
# Option to add the effect of ground plane under the
# target using an approximate method: 1=yes, 0=no
0
# The ground plane is made of N material layers over a dielectric half space.
# Enter number of layers
1
# Consider an example of N=2.The input has N+1 lines:
#      0.37    (2.5, -0.2)   (1.6, -0.7)  0.1
```

```
#      -0.12   (4.3, -0.1)   (1.0,  0.0)  0.1
#      -0.96   (1.6,  0.0)   (1.0,  0.0)  0.0
# Here the top layer is at z=0.37 length unit, and its relative epsilon and mu
# are given by the next two complex numbers. The last column is conductivity
# in siemens per meter (S/m). The middle layer starts at z=-0.12
# and the dielectric half space starts at z=-0.96. If the half space is a PEC,
# replace the last line by
#      -0.96   PEC
0.00   (2.5, -0.2)   (1.6, -0.7)   0.01
-0.96   (1.6,  0.0)   (1.0,  0.0)   0.0
#------------------------------------------------
#ADVANCE06: BISTATIC TO MONOSTATIC APPROXIMATION
#------------------------------------------------
# Option of approximating monostatic RCS by bistatic: 1=yes, 0=no
 0
# This approximation is valid within a small bistatic angle "DEL" in degree.
# Typically, DEL=25/sqrt(D), where D is the target size in wavelength.
# For example, DEL=2.5 deg for D=100 WL. Set DEL=0.0 if its value is to be
# determined internally.
 6.0
#----------------------------
#ADVANCE07: NEAR-FIELD OUTPUT
#----------------------------
# Option to output near-field: 1=yes, 0=no
 0
# The following fields are available for output:
#   1 --- Primary field only (incident field or transmitter field)
#   2 --- Scattered E-field
#   3 --- Total E-field (=incident+scattered)
#   4 --- Primary E-field and ETA0*H field (ETA0=120*pi ohm)
#   5 --- Scattered E-field and ETA0*H field
#   6 --- Total E-field and ETA0*H field
# Enter your selection:
 2
# The observation locations for the near-field can be
# specified in two ways:
#   Method 1 --- start stop nstep
#   Method 2 --- give a facet or quad file in the standard format
#   Method 3 --- a. Applicable to PEC (not coated) targets only.
#                b. Nearfield obs points fall on the scatterer surface
#                c. Best in speed
#   Method 4 --- Use the interior points of the facet/quad file given below
# Enter your selection (if method=4, also enter the number of points per
# facet/quad, namely 4 1 or 4 4)
 2
# In case of Method 1, enter: x1 y1 z1  x2 y2 z2  nstep
# Unit is the same as that of the target, and nstep=0 means one point.
0.0  10.2  -4.3  2.3  0.8  0.15  30
# In case of Method 2, enter the name of a facet/quad file
#    whose vertices are observation points of the near-field.
# In case of Method 3, give a name for the facet/quad file that will be output
#    by SAF, e.g. tank_refined.facet. This file describes the same traget
#    gemotry as the input CAD file in Sec.A, but its mesh may be refined or
#    its ordering of nodes changed.
# In case of Method 4, enter the name of a facet/quad file whose interior
#    points are observation points of the near-field.
#
```

```
# Format for entering CAD files for observation points
#    Example for 1 CAD file:
#       obv1.facet
#    Example for 3 CAD files
#       obv1.facet    MULTIPLECAD 3
#       obv2.facet
#       obv3.facet
obv1.facet
#----------------------------------------------------
#ADVANCE08: RCS EXTRAPOLATION IN FREQUENCY AND ANGLES
#----------------------------------------------------
# This option allows a rapid computation by extrapolation of RCS over
# a very dense grid in frequency/EL/AZ, as specified in Sec.A .
# Option to use this extrapolation: 1=yes, 0=no
0
# Suppose the steps given in Sec.A for (frequency, EL, AZ) is (255, 0, 63).
# A new, sparser grid with steps (20, 0, 11) for example may be chosen for
# RCS calculations. Next RCS values are extrapolated to fill the original
# dense grid. This option saves computation time. In addition, it produces
# a less_noisy RCS variation over the dense grid. This feature works well
# if the scattering is dominated by one-bounce contribution.
# Enter your new, sparser steps in frequency, EL and AZ:
4 5 0
#-------------------------------
#ADVANCE09: ADDITIONAL JOB CONTROL
#-------------------------------
# This option allows users to have additional controls on the program run.
# Option to use this feature?  1=yes, 0=no
 0
# Check the memory requirement:
#    1 = check but do not complete the actual run
#    0 = check and then complete the run
1
# The input CAD files may be refined by SAF by consolidating nodes,
# subdividing meshes, reverse normals etc. Enter your selection for
# outputing the refined CAD files:
#    2 -- Output surface mesh (no output if there is no surface mesh)
#    3 -- Output volume mesh (no output if there is no volume mesh)
#    4 -- Output all meshes.
#    0 -- No mesh output
# (For an input tank.facet, the refined file is tank_refined.facet)
 0
#------------------------------------
#ADVANCE10: RESTART AN UNCOMPLETED JOB
#------------------------------------
# This option allows users to restart an uncompleted job for RCS
# calculations (not valid for other applications).
# Option to use this feature?  1=yes, 0=no
0
#-------------------------------------------
#ADVANCE11: RCS FROM ANTENNA MODE IRRADIATION
#-------------------------------------------
# Option to calculate Monostatic RCS from antenna irradiation: 1=yes, 0=no
# If yes, ADVANCE02 INSTALLED ANTENNA PATTERN must be also on, and the
# polarization-angle input in Sec.A become dummy.
 0
# The incident (EL,AZ) is the same as the observation (EL,AZ) in ADVANCE02.
```

```
# The frequency limits are the same as those in Sec.A, except that nstep may
# be different. Enter the new nstep, which can be the same or much bigger
# than its counterpart in Sec.A.
# SPECIAL OPTION: To add one-way antenna feed delay, enter for example
#      255 special 3.8
# meaning that nstep=255, and feed_delay=3.8 length units.
255
# Enter antenna coupling coefficient at three frequencies:
#          f(GHz)    Coupling_mag    Phase(deg)
# Example   2.4         0.0            0.0
#           3.0         1.0           45.0
#           4.7         0.6          -72.0
# Coupling coeff is assumed to vary linearly with frequency.
# Make sure that frequencies in Sec.A fall inside the above range.
2.0     0.0    0.0
2.5     1.0    180.
3.0     0.3    70.
#-----------------------------------------------
#ADVANCE12: NEAR-FIELD OUTPUT FROM HUYGEN SOURCE
#-----------------------------------------------
# This option is for CrossFlux "Level 2" application and must be used in
# conjunction with ADV07. The incident field in ADV07 is a plane wave.
# Option to replace the plane wave by a Huygen source: 1=yes, 0=no
 0
# The xyz location of the Huygen source is given previously by
#   a. the CAD file in ADV07 if Method 2 or 4 is used, or
#   b. the CAD file in Sec.A if Method 3 is used.
# Name the .nearfield file that describes the (E,H) fields of the Huygen
# source for the incident v-pol (e.g. sphere_v.nearfield).
sphere_v.nearfield
# Name the corresponding file for incident h-pol (e.g. sphere_h.nearfield).
sphere_h.nearfield
#-----------------------------------------------
#ADVANCE13: OUTPUT SURFACE CURRENT FOR DISPLAY
#-----------------------------------------------
#--Option to output surface current (J=ETA0*J'). Here ETA0=120pi is free-space
#  wave impedance and J'=true (vector) current in A/m. For targets with volume
#  material, only surface (not volume) currents are provided. The surface part
#  of the target is described in Sec.A by a facet or quad file. For a
#  multi-angle-frequency run, output is given only for the first case. Use
#  xedge for display after loading in a SAF_color preference file.
#--Enter your selection:  1=yes, 0=no
0
#--Current locations:
#     1= At centers of facets/quads. The magnitude of current is scaled to an
#        integer from 1 to n where n=28 by default. This integer is written in
#        the position of ICOAT in the output facet/quad file.
#        An option to reset n to for example 64: enter " 1 COLOR 64"
#     2= At nodes of facets/quads (as the 4th column in the coordinate part)
#        The "-color" option is ignored.
#--Enter your selection:
1
#--Definition of current magnitude
#     1 = Norm of real part of vector J = sqrt[(Re(Jx)^2+(Re(Jy)^2+(Re(Jz)^2]
#     2 = Norm of complex vector J =sqrt(|Jx|^2+|Jy|^2+|Jz|^2)
#--Enter your selection:
1
```

```
#--Current scale: 1=Linear, 2=dB
1
#---------------------------------------------
#ADVANCE90: SETTINGS FOR EM METHOD AND SOLVER
#---------------------------------------------
#---Option to adjust internal EM settings: 1=yes, 0=no
0
#---Set the upper limit of edge length in wavelength
#   (Typical values are 0.1 to 0.3, default value is 0.2)
0.2
#---For a CLOSED target (or the closed part of a mixed open/closed target),
#   CFIE is used with a parameter "alpha" defined by
#           CFIE = alpha*EFIE + (1-alpha)*MFIE
#   For open target (or the open part of a mixed open/closed target), alpha
#   is always 1 and this input has no effect. Suggested alpha for a closed
#   target is 0.4-0.6. Enter your selection (Default 0.4):
0.4
#---Three matrix solvers are available:
#     1 = Direct solver using LUD (efficient for small targets)
#     2 = Iterative solver with full matrix (not recommended for large targets)
#     3 = Iterative solver with MLFMA acceleration
#   Enter your selection (Default 3):
3
#---If MLFMA is selected, you have an option to adjust L, the number of FMM
#   levels. Higher L generally results in less CPU time and memory, and more
#   errors. Choices of L are
#     L = -1 (levels to be selected internally, default)
#       = 2.0 or greater
#   Example L=5.8, which means 6 levels of FMM and the scaling by 1.2 of
#   the bounding box of the target. Enter L:
-1
#---If the iterative solver is selected, then there are two iterative methods
#   in the program: CG and BiCG. Typically CG is more stable than BiCG,
#   but BiCG converges faster than CG in mmny cases.
#   Enter your selection: 1=CG (Default), 2=BiCG
1
#---If the iterative solver is selected, then the termination of the iteration
#   has two controls: the maximum number of iteration, and the residue error
#   Enter these two numbers (Default 300 1.e-2)
300   1.0E-02
#---For a CLOSED target, the iteration convergence may be sped up by using
#   a matrix preconditioner. Enter
#      0 = Do not use preconditioner for a closed target (Default)
#      1 = Use block diagonal preconditioner
#   This input has no effect on an open or mixed open/closed targets.
0
########################## END OF INPUT PARAMETERS ##########################
```

```
#---FISC (Fast Illinois Solver Code) v.1.7 Jan 2002
#*********************************
#A --- CAD, FREQUENCY, and ANGLES
#*********************************
#---Target is described by a triangular facet file in ACAD/Xpatch format.
#   Edges of adjacent facets must be matched.
#---Enter facet file name:
bottom_cylinder_closed.facet
#---Is the target open?  1=open,  2=closed.
2
#---Length unit:  1=inch, 2=cm, 3=meter, 4=mm, 5=mil.
4
#---Frequency(GHz): start, stop, and nstep.
#   (nstep is # of increments e.g. nstep=0 for 1 point)
0.080 0.080 0
#---Incident polarization: 1 = E-theta(Vertical pol.),
#                          2 = E-phi  (Horizontal pol.),
#                          3 = Both pols.
3
#---1=monostatic RCS,  2=bistatic RCS.
1
#---Incident EL: start, stop, and nstep (All angles in deg: EL=90-theta).
#   (nstep is # of increments e.g. nstep=0 for 1 point)
90.0000 -90.0000 181
#---Incident AZ: start, stop, and nstep (AZ=-phi).
0.0000 0.0000 0
#---Observation EL: start, stop, and nstep (dummy for mono).
0.0000 0.0000 0
#---Observation AZ: start, stop, and nstep (dummy for mono).
0.0000 0.0000 0
#*********************************
#B --- ACCURACY AND MATRIX SOLVER
#*********************************
#---Choose accuracy:  0=low,  1=medium,  2=high.
1
#---Choose matrix solver:
#    1 = LUD (good for small targets),
#    2 = Iteration using full matrix,
#    3 = Iteration using MLFMA (good for large targets).
3
#*****************
#C --- EM SETTING
#*****************
#---Choose  1=default EM setting,  2=custom setting.
2
#---If default setting, ignore the rest of the input in Sec.C.
#   Choose maximum edge length in wavelength:
#   Suggestion: 0.1 to 0.2
0.1
#---Testing function:  1=Galerkin's method,  2=line matching.
#   Suggestion: 1
1
#---Number of integration points for testing, basis functions.
#   Points for testing: Galerkin's method: 1, 4 or 7;
```

```
#                      line matching:    1, 2 or 3.
#   Points for basis: 1, 4 or 7
#   Suggestion: 1 1
1 1
#---Alpha for CFIE (between 0.0 and 1.0, EFIE: alpha=1.0; MFIE: alpha=0.0)
#   For open target, use EFIE only.
#   Suggestion: 0.5 for closed target, 1.0 for open target.
0.5
#---Choose matrix iteration methods: 1=cg, 2=bicg.
2
#---Choose maximum number of iterations and error_bound:
#   Suggestion: 200 2.e-3
800 0.002
#---Option to write a facet file showing induced current on the target
#   for display by Xedge:  0=no, 1=facet, 2=patch, 3=both.
1
#
#---Next two parameters for MLFMA only
#
#---Use block diagonal preconditioner: 0=no,  1=yes.
#   Suggestion: 0 for alpha=1.0, 1 for alpha<1.0
1
#---Choose the number of levels in MLFMA method:
#   Suggestion: -1 (it will be decided by the code)
-1
#***************
#D --- MATERIAL
#***************
#---Is the entire target PEC?   1=yes,  0=no.
1
#---If non-PEC, enter total # of materials:
#   (NOT including PEC, which is identified by ICOAT=0)
1
#---For each material, identify its ICOAT and IBOUNDARY:
#   ICOAT = any positive integer from 1 on (need not be consecutive).
#   IBOUNDARY = 1 if impedance boundary,
#               2 if resistive sheet.
#   For each material, give info by following the templates:
#^^^ a new material ^^^^^^^^^^^^^^^^^^^^^^^^^^^^^^^^^^^^^^^^^^^^^^
#---ICOAT (any positive integer from 1 up)
23
#---IBOUNDARY
1
#---Complex surface impedance in ohm e.g (35.45 -90.76)
(3000,200)
#------------------------------------------------------------------
#'OPTIONAL ADVANCED FEATURES' (Do not change letters in quotations)
#The line above must be placed at the end of the regular FISC
#input. Some features are designed using approximations.
#-------------------------------------------------------
#ADVANCED1: APPROXIMATION OF BISTATIC RCS TO MONOSTATIC RCS
#-------------------------------------------------------
# Choose bistatic to monostatic approximation, 1=yes, 0=no.
0
# Since this approximation is for one direction only,
# if both incident EL and AZ angles are changed,  input 1=EL, 2=AZ.
1
```

```
# Sweeping angle in degrees, it is about 20 to 36 divided by square root
# of the electrical size of the target in wavelength.
0.0000
#-------------------------------------------------------
#ADVANCED2: FREQUENCY INTERPOLATION OF SCATTERED FIELD
#-------------------------------------------------------
# If nstepfreq in Section 1 is greater than 2,
# choose frequency interpolation of scattered field, 1=yes, 0=no.
0
# If yes is chosen, input no. of steps of frequency used for calculation.
# It should be less than the one given in Section 1, and is about
# 10*(Lmax-Lmin), where Lmax, Lmin are the electrical sizes of the target
# in wavelength at frequencies freq_stop and freq_start, respectively.
#   (nstep is # of increments e.g. nstep=0 for 1 point)
0
#----------------------------
#ADVANCED3: MULTIPLE RHS SOLVER
#----------------------------
# If the number of incident angles in Section 1 is greater than 1,
# use Multiple Right-Hand-Side (RHS) solver, 1=yes, 0=no.
0
# If yes is chosen, choose the MRHS solver:
#    1 for seed BiCG algorithm,
#    2 for average block/seed BiCG algorithm with minimal residue smoothing,
# default is 2.
2
# If yes is chosen, input no. of RHS to be solved each time.
#  The larger this number, the more is the memory needed, but
#  more CPU time may be saved.
1
#------------------------------------------
#ADVANCED4: RANGE-DEPENDENT NEAR-FIELD RCS
#------------------------------------------
# The regular RCS calculated by FISC is based on the assumption that both
# radar transmitter TX and receiver RX are in the far field. Therefore, the
# RCS value is independent of range R. This assumption is relaxed here.
# Option to calculate range-dependent RCS, 1=yes, 0=no.
0
# Both antenna patterns of TX and RX are assumed to be isotropic.
# Three cases for possible TX and RX locations:
#    Case     TX_location     RX_location
#    -----------------------------------
#     1        R               infinite
#     2        infinite        R
#     3        R               R
# Enter case:
3
# Specify R in unit of meters by entering the start, stop, and nstep.
100.0000 1.0000 100
# In what manner is R increased?  1=linear,  2=logistic.
2
#----------------------------------------------------
#ADVANCED5: INTERPOLATION/EXTRAPOLATION OF CURRENTS
#----------------------------------------------------
# If RCS for multiple frequencies is needed, frequency interpolation
# or extrapolation of electric currents can speed up the frequency
# loop.  The electric currents at fewer frequency points or a narrower
```

```
# frequency band are calculated first, then the currents at all
# frequencies are interpolated or extrapolated.  Finally, the RCS is
# calculated. If this feature is used, AD2 (frequency interpolation
# of scattered field) is not used.  Since the same model is used for
# all frequencies, the original model is refined at the highest
# frequency for the longest edge given above.
# Option to use current interpolation/extrapolation, 1=yes, 0=no.
0
# 1: interpolation using cubic spline,
# 2: extrapolation using ESPRIT algorithm.
1
# If 1 (interpolation using the cubic spline) is chosen,
# input the number of steps of frequencies used for calculating currents.
# It should be less than the one given in Section 1, and is about
# 5*(Lmax-Lmin), where Lmax, Lmin are the electrical size of the target
# in wavelength at frequencies freq_stop and freq_start, respectively.
#   (nstep is # of increments e.g. nstep=0 for 1 point)
0
# If 2 (extrapolation using the ESPRIT algorithm) is chosen, input
# start, stop, and nstep of frequency used for calculating currents.
# In order for extrapolation to work properly, the frequency range of
# interest (f1 to f2 in Sec. 1) should be above the target resonance
# region (target size >> 3 lambda with no high-Q phenomena)
# Recommended settings:
# The start frequency should be set to f1.
# The stop frequency should be greater than f1+(f2-f1)/4.
# The frequency sampling should be set to c/(3*L) where L is size
# of the target.
# Example:  f1=1 GHz, f2=2 GHz, L=3 meters
# Choose:   start=1 GHz, stop=1.3 GHz, step=0.033 GHz, nstep=9
#   (nstep is # of increments e.g. nstep=0 for 1 point)
0.0000 0.0000 0
# If 2 (extrapolation using the ESPRIT algorithm) is chosen,
# input the number of signals to be extracted (should be 1 less than half
# of the number of frequency points used for calculating currents)
0
#----------------------
#ADVANCED6: GROUND PLANE
#----------------------
# Add a ground plane: 1=yes, 0=no.
0
# If yes, define the ground plane
#  Which plane, 1 for y-z plane, 2 for x-z, 3 for x-y.
3
#  Position of the ground plane (same unit as section A).
0.0000
#----------------------------------------------------------
#ADVANCED7: Antenna Pattern Analysis
#----------------------------------------------------------
# Antenna Pattern Generation, 1=yes, 0=no.
0
# If yes, how many source points (edges) ?
# Followed by the following information per source
# Amplitude (Amps), Phase (Degrees), ICOMP Source, ICOMP Other
0
#----------------------
#ADVANCED8: LOSSY GROUND PLANE for FOPEN Hybrid
```

```
#----------------------
# Add ground plane: 1=yes, 0=no.
0
#  Position of ground plane (same unit as section A).
-1.0
#  Relative permittivity of ground plane
(1.5,-0.33)
#  Name of FOPEN hybrid input
/full_path_or_local_path/xp4_output_surface_currents.txt
0
```

References

[1]   C. A. Balanis, *Advanced Engineering Electromagnetics*. New York: John Wiley & Sons, 1989

[2]   A.F. Peterson, S.L. Ray, R. Mittra, *Computational Methods for Electromagnetics*, New York: IEEE Press, 1998.

[3]   M. J. Havrilla, "Analytical and experimental techniques for the electromagnetic characterization of materials," Ph.D. dissertation, Michigan State University, East Lansing, Michigan, 2001.

[4]   E. F. Knott, J. F. Shaeffer, and M. T. Tuley, *Radar Cross Section*, 2nd ed. Raleigh, NC: SciTech Publishing, 2004.

[5]   B. Welsh, W. Muller, B. Kent, "Air Force Research Laboratory Advanced Compact Range RCS Uncertainty Analysis for a General Target".

[6]   P. Collins. Class handout, EENG 627, Radar Cross Section Analysis, Measurement, and Reduction, Graduate School School of Engineering and Management, Air Force Institute of Technology, Wright-Patterson Air Force Base, Ohio,Spring Quarter, 2005.

[7]   B.M. Kent, "Comparative measurements of precision radar cross section (RCS) calibration targets," Proc. IEEE, vol. 4, pp. 412-415, Jul. 2001.

[8]   J. W. Crispin, Jr. and A. L. Maffett, "Radar Cross-Section for Simple Shapes," Proceedings of the IEEE, Aug. 1965, Volume 53, Issue 8: 972-982

[9]   R. L. Eigel, Jr., "Bistatic Radar Cross (RCS) Characterization of Complex Objects", M.S. thesis, Air Force Institute of Technology, Wright-Patterson Air Force Base, Ohio, 1999

[10]   L. R. Hendrick, "Analytical Investigation of Near Zone/Far Zone Criteria", Proc. Radar Reflectivity Measurement Symp., July 1964, AD 601 365, National Technical Information Service, Springfield, VA, pp. 5-19, Aug. 1965.

[11]   D. L. Mensa, *High Resolution Radar Cross-Section Imaging*, Artech House, Boston, MA, pp 29-31, 1991.

[12]   J. Moore, R. Pizer, *Moment Methods in Electromagnetics, Techniques and Applications*, New York, 1984.

[13]   *User's Manual for FISC (Fast Illinois Solver Code)*, Center for Computational Electromagnetics, University of Illinois at Urbana-Champaign and DEMACO,   Inc., Champaign, Illinois, January 1997.

[14]   J.Song, W.C. Chew, "Fast Illinois Solver Code: Requirements and Scaling Properties", , Department of Energy, February 1998.

[15]   M.I. Skolnik, *Introduction to Radar System*, 3rd ed. New Delhi: McGraw-Hill,   Inc. 2001.

[16]   M.L. Hastriter, "A Study of MLFMA for Large-Scale Scattering Problems", Ph.D. dissertation, University of Illinois at Urbana-Champaign, 2003.

[17]   J.M. Putnam, M.B Gedera, "CARLOS-3D™: A General-Purpose Three-Dimensional Method of Moments Scattering Code", IEEE Antennas and Propagation Magazine, 35(2):69-71, April 1993.

[18]   J.M. Putnam, J.D. Kotulski. *Parall*el *CARLOS-3D Code Development.* Technical Report SAND96-0335C, Sandia National Laboratory, Department of Energy, February 1996.

[19]   S.W. Lee, H. Ling, C. Lu, J. Moore,. *CrossFlux: A Method for Hybridizing Xpatch and Other Codes.* Institute of Electrical and Electronics Engineers, 2005.

[20]   K. J. Cassell, "Investigation of time-domain and frequency-domain free-space material measurements," M.S. thesis, Air Force Institute of Technology, Wright-Patterson Air Force Base, Ohio, 2006.

REPORT DOCUMENTATION PAGE

1. REPORT DATE *(DD-MM-YYYY)*	2. REPORT TYPE	3. DATES COVERED *(From – To)*
23-03-2006	Master's Thesis	Sep 2004 – Mar 2006

4. TITLE AND SUBTITLE	5a. CONTRACT NUMBER
Comparison Of Computational Electromagnetic Codes For Prediction of Low-Frequency Radar Cross Section	5b. GRANT NUMBER
	5c. PROGRAM ELEMENT NUMBER
6. AUTHOR(S)	5d. PROJECT NUMBER #
Paul C. Lash, Capt, USAF	5e. TASK NUMBER
	5f. WORK UNIT NUMBER

7. PERFORMING ORGANIZATION NAMES(S) AND ADDRESS(S)	8. PERFORMING ORGANIZATION REPORT NUMBER
Air Force Institute of Technology Graduate School of Engineering and Management (AFIT/EN) 2950 Hobson Way WPAFB OH 45433-7765	AFIT/GE/ENG/06-32

9. SPONSORING/MONITORING AGENCY NAME(S) AND ADDRESS(ES)	10. SPONSOR/MONITOR'S ACRONYM(S)
NASIC/ADNS Attn: Mr. Robert Schalle, Robert.Schalle@wpafb.af.mil 4180 WATSON WAY WPAFB, OH 45433-7765 DSN: 672-3084	11. SPONSOR/MONITOR'S REPORT NUMBER(S)

12. DISTRIBUTION/AVAILABILITY STATEMENT
APPROVED FOR PUBLIC RELEASE; DISTRIBUTION UNLIMITED.

13. SUPPLEMENTARY NOTES
Robert.Schalle@wpafb.af.mil
Michael.Havrilla@afit.edu

14. ABSTRACT
Radar cross section (RCS) prediction of full-scale aircraft is of interest to military planners for a variety of applications. Several computational electromagnetic codes for RCS prediction are available with differing features and capabilities. The goal of this research is to compare the capabilities of three computational electromagnetic codes for use in production of RCS signature assessments at low frequencies in terms of performance, accuracy, and features: Fast Illinois Solver Code (FISC), Code for Analysis of Radiators on Lossy Surfaces (CARLOS-3D), and Science Applications International Corporation Full-wave solver (SAF). The comparison is accomplished through analysis of predicted and measured RCS of several canonical and simple objects and a complex target comprised of these constituent objects. In addition to RCS accuracy, memory requirements and computation time are key considerations for this code comparison. Verification of code performance in memory and processing time based on varying levels of unknowns is performed. A 1/36 scale body-of-revolution missile model is the complex model constructed for measurement and prediction. The model corresponds to an 18-meter full-scale target and includes a cavity allowing mode propagation at frequencies of interest. The complex model is simulated at 400 and 500 MHZ corresponding to a 24 and 30 lambda target length, respectively. RCS of each constituent part of the model is also analyzed to establish a level of confidence in solution accuracy. Solution convergence is shown using increasing discretization levels. A comparison is also conducted between measured and predicted results for two PEC objects coated with magnetic radar absorbent material (MRAM). The RCS for a 12″×12″ MRAM-coated PEC flat plate and a 9″×9″ MRAM-coated PEC right circular cone are measured in the Air Force Research Laboratory's compact RCS/antenna measurement range and then compared to results from FISC using its impedance boundary condition (IBC) feature. A physical optics method for predicting RCS of a material-coated PEC plate is also developed as a third data. The IBC formulation is generalized for polarization and angle-dependent impedances to investigate prediction improvement. Results of each part of the comparison are presented as well as the methodology used to evaluate the codes.

15. SUBJECT TERMS
radar cross section, computational electromagnetic code, method of moments, impedance boundary condition

16. SECURITY CLASSIFICATION OF:			17. LIMITATION OF ABSTRACT	18. NUMBER OF PAGES	19a. NAME OF RESPONSIBLE PERSON
REPORT U	ABSTRACT U	c. THIS PAGE U	UU	166	Michael J. Havrilla, Ph.D. (AFIT/ENG)
					19b. TELEPHONE NUMBER *(Include area code)* (937) 255-3636 ext 7252, Michael.Havrilla@afit.edu

Standard Form 298 (Rev: 8-98)
Prescribed by ANSI Std. Z39-18

[1]   C. A. Balanis, *Advanced Engineering Electromagnetics*. New York: John Wiley & Sons, 1989

[2]   A.F.Peterson, S.L. Ray, R. Mittra, *Computational Methods for Electromagnetics*, New York: IEEE Press, 1998.

[3]   M. J. Havrilla, "Analytical and experimental techniques for the electromagnetic characterization of materials," Ph.D. dissertation, Michigan State University, East Lansing, Michigan, 2001.

[4]   E. F. Knott, J. F. Shaeffer, and M. T. Tuley, *Radar Cross Section*, 2nd ed. Raleigh, NC: SciTech Publishing, 2004.

[5]   Welsh, Bryon M., Muller, William D. and Kent, Brian M. "Air Force Research Laboratory Advanced Compact Range RCS Uncertainty Analysis for a General   Target,"
J. Lee, M. J. Havrilla, J. E. Luminati, M. W. Hyde, and E. J. Rothwell, "Scattering from a cylindrical resistive sheet using a modified PO current," in press., 2005.

[6]   Collins, Peter. Class handout, EENG 627, Radar Cross Section Analysis, Measurement, and Reduction, Graduate School School of Engineering and   Management, Air Force Institute of Technology, Wright-Patterson Air Force   Base, Ohio,Spring Quarter, 2005.

[7]   B.M. Kent, "Comparative measurements of precision radar cross section (RCS) calibration targets," Proc. IEEE, vol. 4, pp. 412-415, Jul. 2001.

[8]   J. W. Crispin, Jr and A. L. Maffett. "Radar Cross-Section for Simple Shapes," Proceedings of the IEEE, Aug. 1965, Volume 53, Issue 8: 972-982

[9]   R. L. Eigel, Jr.,   "Bistatic Radar Cross (RCS) Characterization of Complex Objects", M.S. thesis, Air Force Institute of Technology, Wright-Patterson Air   Force Base, Ohio, 1999

[10]   L. R. Hendrick, "Analytical Investigation of Near Zone/Far Zone Criteria", Proc. Radar Reflectivity Measurement Symp., July 1964, AD 601 365, National   Technical Information Service, Springfield, VA, pp. 5-19

[11]   D. L. Mensa, *High Resolution Radar Cross-Section Imaging*, Artech House, Boston, MA, pp 29-31, 1991.

[12]   J.Moore, R. Pizer, *Moment Methods in Electromagnetics, Techniques and Applications*, New York, 1984

[13]   *User's Manual for FISC (Fast Illinois Solver Code)*, Center for Computational Electromagnetics, University of Illinois at Urbana-Champaign and DEMACO,   Inc., Champaign, Illinois, January 1997.

[14]   J.Song, W.C. Chew, "Fast Illinois Solver Code: Requirements and Scaling Properties", ######, Department of Energy, February 1998.

[15]   M.I. Skolnik, *Introduction to Radar Systems*. 3rd ed. New Delhi, 2001.

[16]   M.L. Hastriter, "A Study of MLFMA for Large-Scale Scattering Problems", Ph.D. dissertation, University of Illinois at Urbana-Champaign, 2003.

[17] J.M. Putnam, M.B Gedera, "CARLOS-3D™: A General-Purpose Three-Dimensional Method of Moments Scattering Code", IEEE Antennas and Propagation Magazine, 35(2):69-71, April 1993.

[18] J.M. Putnam, J.D. Kotulski. *Parallel CARLOS-3D Code Development.* Technical Report SAND96-0335C, Sandia National Laboratory, Department of Energy, February 1996.

[19] S.W. Lee, H. Ling, C. Lu, J. Moore,. *CrossFlux: A Method for Hybridizing Xpatch and Other Codes.* Institute of Electrical and Electronics Engineers, 2005.

[20] K. J. Cassell, "Investigation of time-domain and frequency-domain free-space material measurements," M.S. thesis, Air Force Institute of Technology, Wright-Patterson Air Force Base, Ohio, 2006.